The Huygens Doppler Wind Experiment: A Titan Zonal Wind Retrieval Algorithm

Dissertation
zur
Erlangung des Doktorgrades (Dr. rer. nat.)
der
Mathematisch-Naturwissenschaftlichen Fakultät
der
Rheinischen Friedrich-Wilhelms-Universität Bonn

vorgelegt von
Robindro Dutta-Roy
aus
Rourkela / Indien

Bonn, August 2002

Angefertigt mit Genehmigung der Mathematisch-Naturwissenschaftlichen
Fakultät der Rheinischen Friedrich-Wilhelms-Universität Bonn

1. Referent: Prof. Dr. Max Römer
2. Referent: Prof. Dr. Ulrich Mebold

Tag der Promotion:

Contents

List of Figures

List of Tables

Chapter 1

Introduction

The Cassini/Huygens mission to Saturn, a joint venture of NASA and ESA, was launched on 15 October 1997 from Kennedy Space Center, Cape Canevaral, Florida (USA). After a cruise phase of almost seven years, the mated Cassini and Huygens spacecraft will reach their destination in 2004. Cassini will orbit Saturn for at least four years after Saturn orbit insertion (SOI) on 1 July 2004, performing numerous flybys of Saturn's various moons. The NASA contribution Cassini carries twelve experiments which will monitor the Saturnian system in unprecedented detail along the way (Spilker, 1997). The ESA Huygens Probe, an atmospheric entry vehicle carrying another six experiments, is designed to penetrate the rather thick atmosphere (1.5 bar at the surface) of Saturn's largest moon Titan. Huygens is the first ESA mission to the outer solar system.

The Huygens Probe is scheduled to be separated from the Cassini Orbiter about six months after SOI. Three weeks later it will enter the atmosphere of Titan. Following release of its heat shield, it will descent through Titan's atmosphere under a parachute for approximately 2.25 hours and eventually impact Titan's surface. The primary goals of the Huygens mission are a detailed *in situ* study of Titan's atmosphere and a characterization of its surface along the descent ground track.

The Huygens transmission antennae have a rather small gain, thereby precluding direct transmission to Earth of the experimental data gathered during the descent. Instead, the data are first uplinked to Cassini for temporary storage via a "Probe Relay Link" (PRL). Upon conclusion of the Huygens mission, Cassini's High Gain Antenna (HGA) will be repointed away from Huygens towards Earth for the data downlink.

The Doppler Wind Experiment (DWE), one of the six experiments carried out during the Huygens descent through Titan's atmosphere and topic of this thesis, utilizes the Doppler effect on the PRL carrier frequency to measure

the radial velocity of Huygens with respect to Cassini. Its primary goal is the determination of the altitude dependence of Titan's zonal (east-west) winds along the descent track, thereby providing *in situ* verification ("ground truth") of remote Cassini observations. The most problematic DWE issue is an accurate extraction of all Doppler components other than that due to the zonal wind. The Principle Investigator (PI) of the DWE is Michael K. Bird, member of the scientific staff of the Radioastronomical Institute of the University of Bonn, Germany.

The goal of this thesis is to develop the algorithm necessary for retrieval of the zonal wind speed from the PRL carrier frequency measurement and to estimate the accuracy to which this can be performed.

Chapter 2

Titan

2.1 Facts About Titan

Discovered 1655 by the Dutch astronomer Christiaan Huygens, Titan is the only moon in the solar system with a substantial atmosphere. The atmosphere was discovered in 1907 by the Spanish astronomer José Comas Solá, who observed its limb darkening (Comas Solá, 1908). In 1944 Gerard Kuiper discovered gaseous methane in Titan's atmosphere by spectroscopic observations (Kuiper, 1944). Methane was believed to be the major constituent until the mid-1970s, when new models suggested the presence of molecular nitrogen. Measurements made during the Voyager 1 flyby in November 1980 confirmed that nitrogen is the major constituent in Titan's atmosphere.

The Voyager measurements were the basis for an atmospheric model developed by Lellouch and Hunten (Lellouch and Hunten, 1987; 1997), which is shown in Fig. 2.1. For Huygens engineering purposes, an improved model was established (Yelle *et al.*, 1997), which, however, does not deviate significantly from the Lellouch-Hunten (LH) model. The LH model is used in this thesis.

According to the LH model, methane is the most important minor constituent, contributing about 8% of the atmospheric molecules near the surface. The methane mixing ratio decreases with altitude and reaches a constant value of 1.5% for altitudes above 34 km. Argon may also be present in quantities up to 6% (Courtin *et al.*, 1995).

The photodissociation of methane and nitrogen, driven by solar UV radiation, cosmic rays and precipitating energetic magnetospheric particles, gives rise to a complex organic chemistry. As a result, Titan's atmosphere contains ethane, acetylene and more complex hydrocarbons. With a surface temperature of 94 K, it resembles a young, frozen Earth. Two optically thick haze

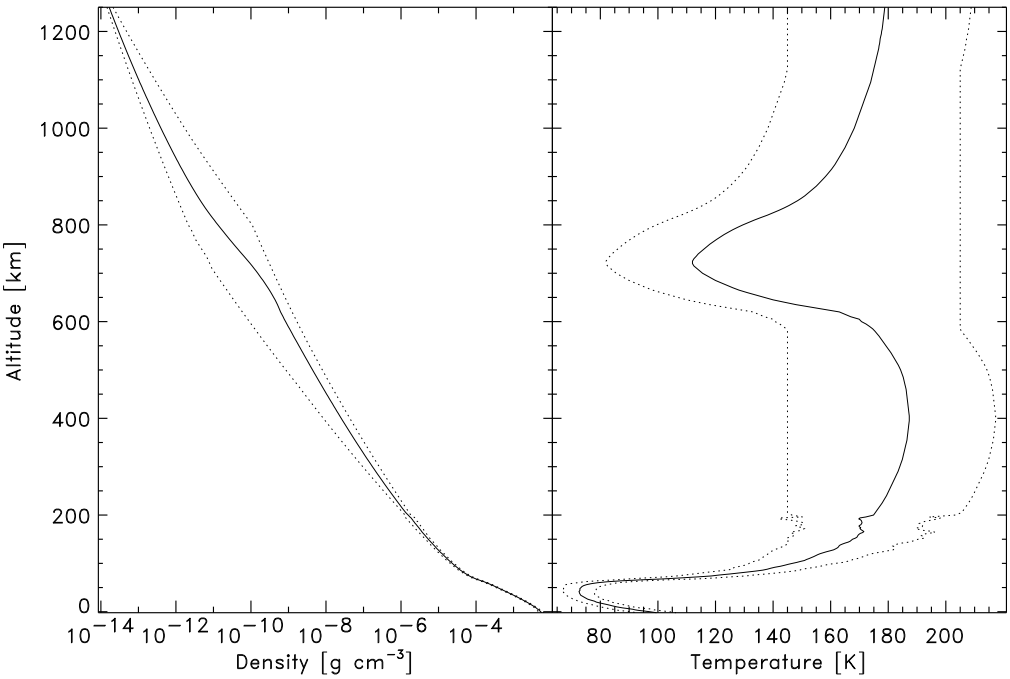

Figure 2.1: Lellouch-Hunten atmospheric model. The dotted lines give the error boundaries of the model.

layers containing aerosol particles, which prevented a view onto the surface, have been identified on images made by Voyager 1. Spectroscopic windows are found at radio and IR frequencies. These have been used for radio occultation measurements during the Voyager 1 flyby (Lindal *et al.*, 1983) and for Earth-based radar (Muhleman *et al.*, 1990) and photometric observations of surface features (Smith *et al.*, 1996). Titan's surface, however, is still a mystery. The presence of methane in Titan's atmosphere requires a continuously resupplying source, which could be lakes or even oceans of methane and ethane, or underground liquid methane reservoirs.

The orbital period of Titan is 15.95 days. Theoretical considerations and recent IR observations of surface features imply that the orbital and the rotation period are synchronous (see Sec. 5.6.5). Titan is therefore a slowly-rotating planetary body with only small Coriolis forces.

The most important physical properties are listed in Table 2.1. More information, i.e. on pressure, temperature, scale height, the properties of the two haze layers and on the observed north-south asymmetry, was gained from two stellar occultations (Hubbard *et al.*, 1993; Tracadas *et al.*, 2001). All measurements are consistent with the Voyager findings.

Table 2.1: Physical properties of Titan

Surface radius	2575 ± 0.5 km
Mass	$1.346 \cdot 10^{23}$ kg
Surface gravity	1.345 m s^{-2}
Mean density	1.881 g cm^{-3}
Distance from Saturn	$1.226 \cdot 10^{6}$ km (20.3 Saturn radii)
Orbital period	15.95 d
Rotation period	15.95 d
Surface temperature	94 ± 5 K
Surface pressure	1496 ± 20 mbar

2.2 Winds on Titan

The Voyager 1 measurements indicated that Titan's atmosphere probably superrotates cyclostrophically, i.e. well in excess of the surface rotation rate. The circulation would thus be similar to that of Venus, the only other planet where cyclostrophic superrotation has been observed. However, the evolution and maintenance of cyclostrophic atmospheres is not well understood. The investigation of Titan's atmospheric rotation by DWE and remote sensing instruments will provide new insights into these complex dynamical systems.

Based on the latitudinal temperature gradients detected by Voyager 1 at various altitudes (Lindal *et al.*, 1983), it is possible to calculate the zonal wind speed u using the "thermal wind equation"

$$\frac{\partial}{\partial \hat{z}}(u^2 \tan\lambda + 2u\Omega R_T \sin\lambda) = -R\frac{\partial}{\partial \lambda}\left[\frac{T}{\mu}\right] \tag{2.1}$$

where $\hat{z} = \ln(P_S/P)$ is the vertical log-pressure coordinate with P_S the surface pressure, T the temperature, λ the latitude, R_T the planetary radius, Ω the angular velocity of the planetary rotation, μ the mean molecular weight of the atmosphere and R the gas constant. With $u \gg \Omega R_T$ (the cyclostrophic limit), the second term on the left side of Eq. (2.1) can be neglected. Assuming that the winds near the surface are negligible, Eq. (2.1) can be integrated upwards to obtain a zonal wind profile. However, because the velocity appears as u^2 in the equation, the direction of the winds is uncertain.

Flasar *et al.* (1992; 1997) obtained a zonal wind model on this basis using the observed latitudinal temperature gradients at three different heights. The model is plotted in Fig. 2.2 as a short-dashed line. The Flasar model, used in this thesis as a reference model, was established for a latitude of 45°. In the altitude and latitude ranges of interest for the Huygens mission, it must be scaled by $\cos\lambda/\cos 45°$ to lower latitudes. This variation is based on the assumption that the zonal wind has a constant angular speed for latitudes equatorward of 45°. It must be noted that Eq. (2.1) does not allow direct retrieval of the zonal wind speed at the equator, because the temperature gradient vanishes there.

The models shown in Fig. 2.2 have been scaled to a latitude of 18°N, the originally foreseen latitude of the Huygens descent. Meanwhile the descent latitude has been changed to 10°S, so the zonal wind speed of the model is about 3% faster than displayed here.

If the observed equator-to-pole temperature gradients are stretched to the maximum, corresponding to double the best-fit values, the resulting zonal wind speed is $\sqrt{2}$ higher. With the additional assumption that the temperature gradient increases linearly with $\ln P$, Lunine *et al.* (1991) obtained the

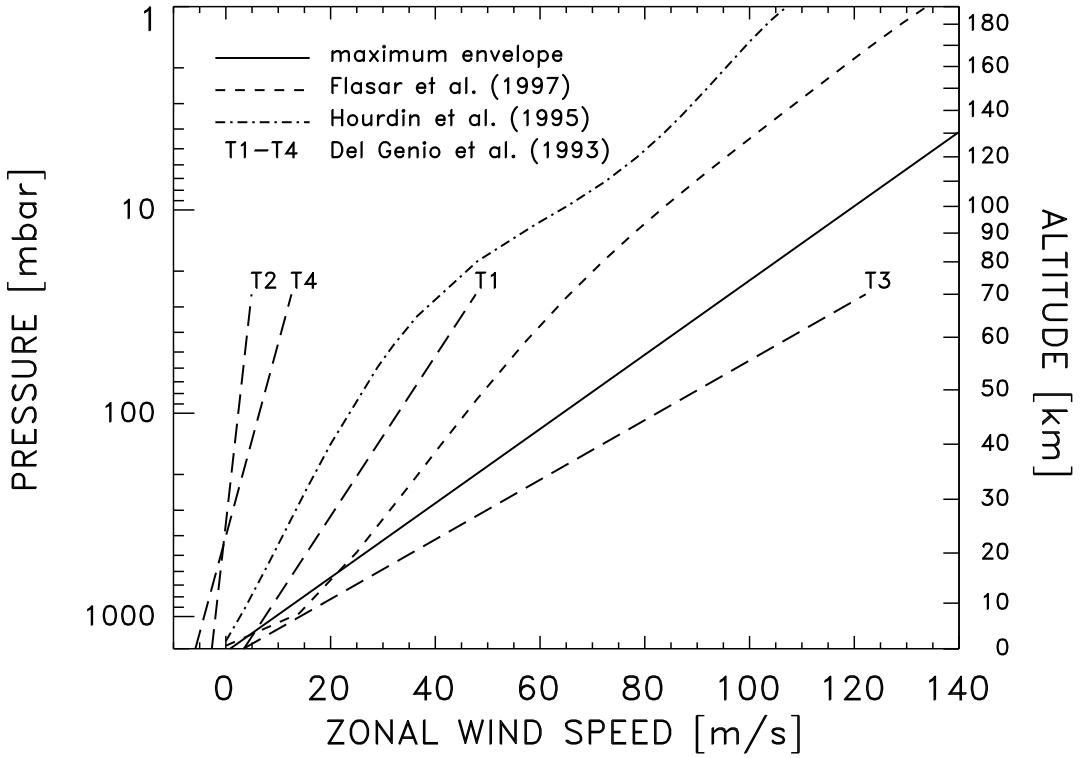

Figure 2.2: Models of the zonal wind height profiles on Titan at a latitude of 18°. The models are symmetric about the equator.

following scaled formula for a "maximum envelope"

$$\mid u(z) - u_S \mid = u_0 \left[1 + \frac{1}{8} \ln[\frac{P_0}{P(z)}]\right] \cos\lambda \tag{2.2}$$

where $u_S \simeq 0$ is the wind at the surface, $P(z)$ is the pressure and the wind and pressure at a fiducial height were taken as $u_0 = 200$ m s^{-1} at the $P_0 = 0.5$ mbar level. The maximum envelope is plotted in Fig. 2.2 as a solid line.

Several General Circulation Models (GCMs) have been adapted to the study of atmospheric superrotation on Titan (Del Genio *et al.*, 1993; Hourdin *et al.*, 1995; Tokano *et al.*, 1999). While these have plausibly simulated an upper atmospheric superrotation qualitatively consistent with the observed temperature gradient on Titan, the detailed wind structure may well depend upon the specific contributions of the planetary boundary layer and upper level wave propagation, both depending upon the surface characteristics and topography (Allison, 1992; Hinson and Tyler, 1983).

The zonal wind speed predicted by the GCM of Hourdin *et al.* (1995)

for the seasonal epoch of the Huygens descent is plotted in Fig. 2.2 as a dashed-dotted line. The long-dashed lines are linear fits to the results of a Titan dynamical process study by Del Genio *et al.* (1993). The baseline scenario (T1) features an optically thick, statically stable cloud layer in the upper troposphere. The flow regime is supported by the horizontal mixing of quasi-barotropic eddies. The other curves are obtained using the following modifications: T2 without the absorbing cloud layer, T3 without stratospheric drag and T4 with negligible surface drag. The implication is that T1 agrees best with the winds inferred from the Voyager 1 observations. Both of these models predict a prograde cyclostrophic flow.

The GCM of Tokano *et al.* (1999) predicts rather weak zonal winds of only a few meters per second at the designated Huygens target latitude. This is in conflict with the Voyager observations and the predictions of other models. A reason may be an excessive meridional flow, as stated by the authors. However, reducing the meridional flow produces superrotating jets only at high latitudes, leaving the zonal wind speed near the equator at about 10% of that predicted by the Flasar model.

A common feature of all GCMs is a prediction of fast jets at high latitudes. This is of only academic interest for the Huygens mission, however, because the currently planned descent latitude is 10°S. Furthermore, all GCMs predict meridional and vertical wind velocities much slower than the zonal. These velocity components can be attributed to Hadley cells that transport energy and angular momentum towards the poles. Due to Titan's low rotation rate, Hadley cells may extend from the equator to the poles or even across the equator. Below 200 km altitude, the meridional and vertical wind speeds are probably only of the order of several cm s^{-1}. The fastest meridional velocities (up to 1 m s^{-1} in the lower stratosphere) are obtained from the GCM of Tokano *et al.* (1999). The direction depends on altitude and the applied model, which differ in the scale and exact location of the Hadley cells.

Evidence for a a zonal superrotation is also obtained from the occultation of 28 Sgr by Titan (Hubbard *et al.*, 1993). The stratospheric mean zonal flow is inferred from the measured oblateness of Titan. The central flash of the occultation requires higher angular velocities near the poles than at equatorial latitudes. Combining the results, one derives a stratospheric zonal flow velocity on the order of 100 m s^{-1} near the equator and jets as fast as 180 m s^{-1} near $\lambda = \pm 60°$.

Although the wind direction cannot be definitely established, theoretical considerations based on Kelvin's Circulation Theorem (Flasar and Conrath, 1992) suggest that the angular momentum associated with the planetary rotation acts as a strong constraint in maintaining the sense of this rotation as

meridional circulations establish a differentially rotating atmosphere. This is supported by IR heterodyne spectroscopy measurements of an ethane emission line (Kostiuk *et al.*, 2001). A comparative analysis of the difference in Doppler shifts obtained at the eastern and western limbs implied a global zonal prograde circulation at altitudes above 100 km at the 94% confidence level.

Internal gravity waves in Titan's atmosphere, excited by tropospheric processes, transport momentum vertically and may be important in maintaining the cyclostrophic zonal winds (Hinson and Tyler, 1983). The scale of such waves is a crucial parameter for GCMs. Apart from measuring the mean zonal wind speed profile, the DWE will also monitor systematic Doppler fluctuations to determine possible gravity wave activity in Titan's atmosphere.

Chapter 3

The Huygens Mission

3.1 Experiments

Apart from DWE, described in detail in the following chapters, the Huygens Probe payload consists of five experiments that are briefly described in the following.

3.1.1 Gas Chromatograph and Mass Spectrometer (GCMS)

GCMS is designed to identify and quantify the abundance of the various atmospheric components. It works either in the direct mass spectrometer mode or in the more powerful mode where the gas samples are passed through the gas chromatograph columns to separate components of similar mass before analysis with the mass spectrometer. Furthermore, it is equipped with a separate ionization chamber for analysis of the aerosol pyrolyzer products fed by the ACP (described in the next subsection). If Huygens survives the impact at touchdown, GCMS can also measure the composition of vaporized surface samples (Niemann *et al.*, 1997).

3.1.2 Aerosol Collector and Pyrolyzer (ACP)

ACP collects aerosols for GCMS to analyze their chemical composition. It is equipped with a deployable sampling device that operates twice during descent in order to collect aerosols from two atmospheric layers in the 135-32 km and 22-17 km altitude regions. After extension of the sampling device, a pump draws the atmosphere and its aerosols through filters to capture the aerosols. At the end of each sampling, the filter is retracted into an oven

where the aerosols are heated to three temperatures, in order to conduct a step pyrolysis. The volatiles are vaporized first at lowest temperature. Then the more complex less volatile organic material is heated further, and finally the core of the particles. The pyrolyzer products are flushed to GCMS for analysis, thereby providing spectra for each analysis step (Israel *et al.*, 1997).

3.1.3 Descent Imager/Spectral Radiometer (DISR)

DISR is a multi-sensor optical instrument capable of imaging and spectroscopy over a wide range of wavelengths from the ultraviolet to the infrared (UV-IR, 0.3-1.64 μm). It also measures the upward and downward heat fluxes to determine the radiative and convective heat transport processes in Titan's thick atmosphere. An aureole sensor measures the intensity of the sun's halo, which, among other things, allows one to infer the aerosols' physical properties. A side-looking horizon instrument images the clouds. One of the prime objectives is investigating the nature and composition of the surface of Titan. Therefore, two cameras (one visible, one IR) looking downwards and sideways image the surface. The slow Huygens spin is exploited to construct mosaic panoramas.

During the low altitude part of the descent, it may be possible to infer the Probe drift from such panoramas and thus contribute to the wind measurements. Due to its large distance from the sun and the thick atmosphere, Titan's surface is probably not brighter than 350 times the brightness of nighttime on Earth with a Full Moon. While this would be adequate for imaging, a surface lamp must be activated at an altitude of a few hundred meters to provide enough light in the methane absorption bands for spectral reflectance measurements of the surface (Tomasko *et al.*, 1997).

3.1.4 Huygens Atmospheric Structure Instrument (HASI)

Like DISR, HASI is a multi-sensor instrument designed to measure physical properties of the atmosphere. It comprises a 3-axis accelerometer, various temperature sensors, a multi-range pressure sensor and an electric field sensor array. The accelerometers are optimized to measure entry deceleration for inferring the atmospheric density and thermal profile during the entry phase (see Section 3.2). The electric field sensor features a relaxation probe to measure ion conductivity and a quadrupolar array of electrodes to measure atmospheric and surface material permittivity. The temperature and pressure sensors are mounted on a fixed stub long enough to protude into

the free flow. The electrical sensors are mounted on a pair of deployable booms to minimize the shielding effects of the Probe body. Furthermore, HASI has a capability for processing the surface-reflected signal of the radar altimeter, originally provided as part of the Probe System (Jones and Giovagnoli, 1997), which allows it to return important information about the surface topography and radar properties below the Probe along the descent track (Fulchignoni *et al.*, 1997).

3.1.5 Surface Science Package (SSP)

SSP is designed to measure the physical properties of the surface at the impact site. It includes a force transducer for measuring the impact deceleration and several other sensors to measure the refraction index, temperature, thermal conductivity, heat capacity, speed of sound and dielectric constant of the (liquid) material at the impact site. An acoustic sounder is activated at a height of a few hundred meters for sounding the atmosphere's bottom layer and the surface's physical characteristics before impact. Should Huygens land in a liquid, the acoustic sounder is used in a sonar mode to probe the liquid depth. A tilt sensor is included to indicate Huygens' attitude after impact. SSP also conducts measurements in Titan's atmosphere during the descent. The thermal properties, acoustic velocity and electrical permittivity subsystems may provide useful science measurements of various atmospheric properties (Zarnecki *et al.*, 1997).

3.2 Timeline and Geometry

After an interplanetary cruise phase of seven years, the combined Cassini/ Huygens spacecraft is inserted into a highly eccentric orbit around Saturn on 1 July 2004. During the third orbit, on 18 December 2004, the spacecraft is targeted on an impact trajectory towards Titan. According to the current schedule, Huygens is released a few days later on 24 December 2004. In order to avoid its own impact on Titan, Cassini performs an Orbiter Deflection Maneuver (ODM) on 28 December 2004. The ODM puts Cassini on a trajectory parallel to Huygens that passes Titan on the western side at a distance of 65,000 km.

This schedule, which is still preliminary (as of spring 2002), is the result of a redesign of the Huygens mission. In the old mission scenario, Cassini would have been placed on a trajectory that follows Huygens at a distance of four hours and passes Titan on the eastern side at a distance of only 1,228 km. The range rate (radial velocity) between Cassini and Huygens in this scenario was essentially given by the Cassini velocity, about 5.7 km s^{-1}, leading to a large PRL blueshift. The carrier tracking loop is equipped with a Doppler compensation to account for such a high frequency shift. The decoding section, however, was not. This design flaw, which was discovered after launch in spring 2000, does not allow acceptable telemetry demodulation at a large Doppler shift (Clausen and Deutsch, 2001). The problem is aggravated by a CDMU clock driving the sampling and data transmission rate aboard Huygens. This clock runs slightly fast, thus mimicking an additional blueshift. With the increase of the distance between Titan and Cassini's Titan periapsis to 65,000 km in the new mission scenario, the large Cassini velocity has only a small projection onto the line of sight (LOS) to Huygens.

The old and new targeting strategies are displayed in Fig. 3.1, showing the Titan B-plane as seen from Huygens. The B-plane is a plane passing through Titan's center and perpendicular to the asymptote of the incoming trajectory (Sollazzo *et al.*, 1997). As the Cassini and Huygens trajectories are nearly parallel in both the old and the new cases, the figure is qualitatively valid for Cassini. The "Orbiter Delay Time" (ODT), the time delay between Cassini and Huygens with respect to the B-plane, is 2.1 hours (4 hours in the old mission scenario). The delivery error ellipses shown in Fig. 3.1 represent the 3-σ-uncertainty of the aim points. However, any uncertainty stated in the following is a 1-σ-error.

Three weeks after separation, Huygens enters Titan's atmosphere on 14 January 2005, around 09:00 UTC. The responsibility of the NASA Navigation Team at JPL ends at the so-called "interface altitude" at 1270 km above the surface of Titan. Crossing this altitude marks the beginning of the

"entry phase". This is the altitude at which the delivery errors of Fig. 3.1 are defined. The aim point for the interface altitude is 167.4°E and 10.7°S in the IAU-Titan system (Davies *et al.*, 1996). The zero meridian is defined as the sub-Saturn meridian in this coordinate system. Thus, Saturn will be located "behind" Titan during the Huygens mission.

The Huygens dedicated receivers aboard Cassini will be switched on 45 minutes before while Huygens is switched on by timers about 30 minutes before reaching the interface altitude. Huygens may be switched on up to four hours earlier, pending a currently ongoing discussion. It has been shown in several tests that a warm-up period would reduce the frequency of the CDMU clock and thus reduce the impact of the receiver design flaw.

Upon entering Titan's atmosphere, Huygens is decelerated by atmospheric friction with a maximum of 10-14 g occurring at an altitude of approximately 250 km. HASI is the only instrument operating during this phase. In case of a failure of the wake-up timers, Huygens will be switched on by g-switches at the end of the deceleration phase.

At 160±25 km altitude, about 4.5 minutes after the beginning of the entry phase, a small pilot chute removes Huygens' back cover. The relatively large altitude error is a result of the inaccuracy of the incorporated atmospheric models. About two seconds later, a larger parachute ("main chute") and the front cover are released. The moment of the pilot chute deployment, called t_0, marks the beginning of the "descent phase" and occurs at about 09:11 UTC. All instruments and the transmitter High Power Amplifier (HPA) are now sequentially switched on. The data transmission to Cassini starts about 2.5 min later.

Fifteen minutes after t_0, the large parachute is replaced by a smaller drogue chute, in order to decrease the duration of the descent to 135±13 min. The uncertainty can be attributed to the inaccuracy of the atmospheric models and to topographic uncertainties. The link between Huygens and Cassini can be maintained for at least three, possibly four hours, which allows surface investigations for at least 30 minutes, if Huygens survives the impact at touchdown.

The duration of the Huygens mission is limited basically by the fact that Cassini drifts out of the Huygens antenna beam. This can be seen in Fig. 3.2, which shows the Cassini trajectory during the Huygens descent. The Probe Aspect Angle (PAA) is the angle between Huygens' local vertical and the LOS. The gain of the Probe Transmitter Antennae (PTA) falls off rapidly for PAA$>$ 60°. The angle γ_{DWC} (Doppler Wind Component Angle) describes the projection of the zonal (East-West) velocity component of Huygens onto the LOS and is therefore a crucial parameter for DWE.

Another view of the geometry during the Huygens mission is displayed

in Fig. 3.3, which gives a 3D-impression and shows that the ground tracks of Cassini and Huygens lie approximately in the same plane. Furthermore, as inferred from the shaded areas, the Huygens mission is performed around local noon.

The High Gain Antenna (HGA) of Cassini has a very narrow beam (FWHM: 2.4°). However, due to the rather large range foreseen in the new mission scenario, the pointing error can be neglected. With the large gain and small pointing error of the HGA, it may be possible to maintain the link at PAAs greater than 60°. At the latest, the mission will be terminated when Cassini reaches the horizon as seen from Huygens at around $t_0 + 4$ h.

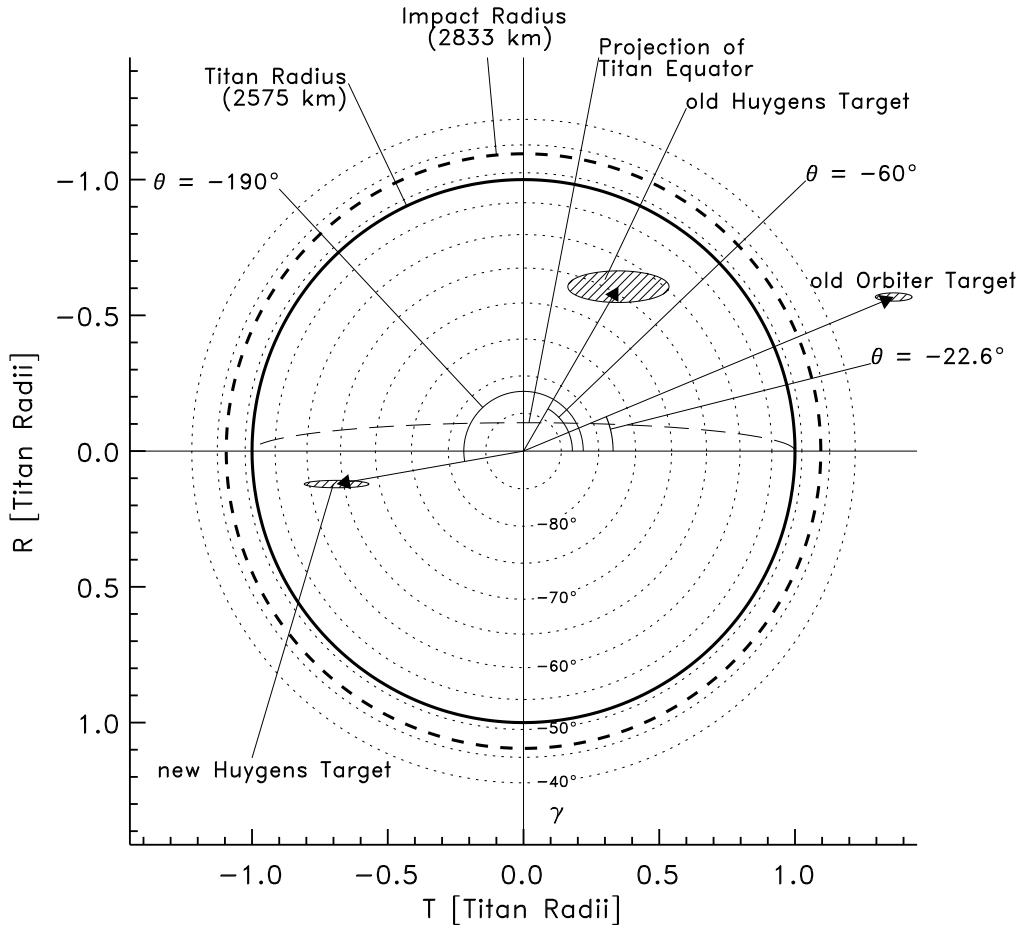

Figure 3.1: Titan B-plane. Old and new delivery error ellipses are shown. The new Cassini delivery error ellipse has a B-plane angle $\theta = -180°$ and is far outside on the left side of this figure.

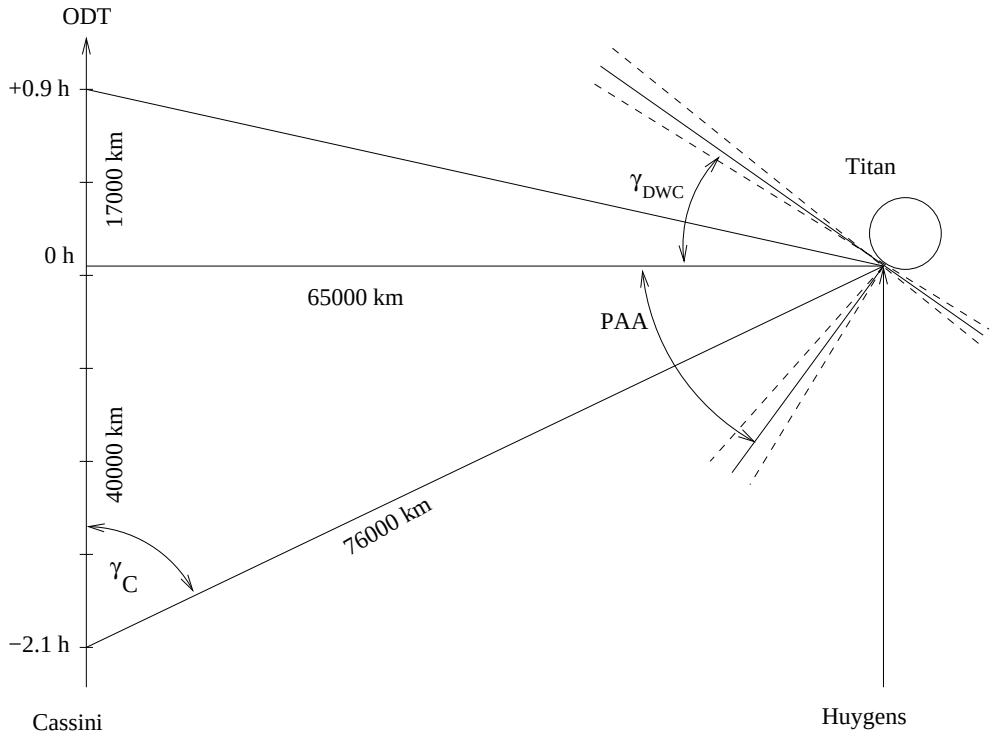

Figure 3.2: Geometry during Huygens mission as seen from Titan's north pole. The angles PAA and γ_{DWC} are affected not only by the Cassini motion but also by the zonal drift of Huygens, as indicated by the dashed lines.

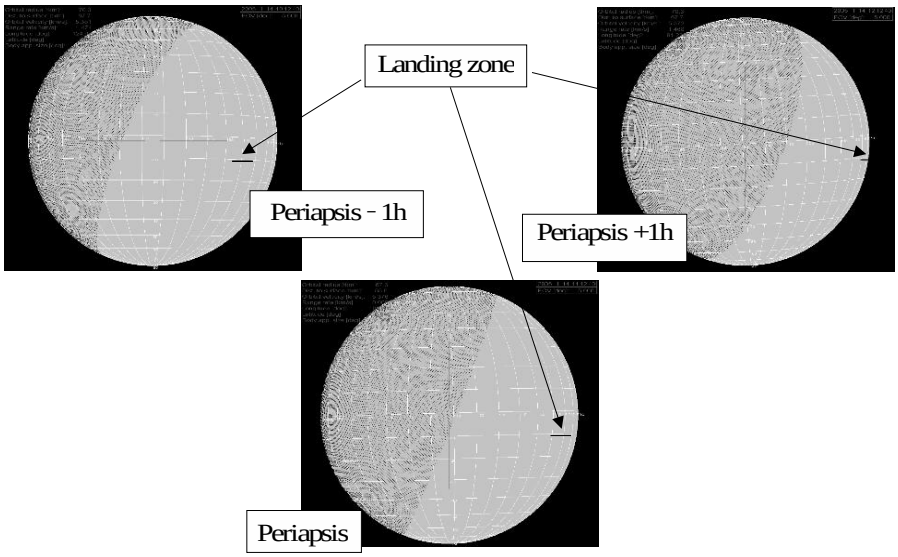

Figure 3.3: Geometry during Huygens mission as seen from Cassini. Orbiter periapsis corresponds to $t_0 + 2.1$ hours (figure displayed with kind permission by Michael Khan, ESOC).

Chapter 4

The DWE Hardware

4.1 Basic Facts and Requirements

While Huygens descends through Titan's atmosphere, the telemetry, comprising experiment science and Probe housekeeping (HK) data, is sent to Cassini for on-board storage via an S-band radio link ("Probe Relay Link", PRL). The signal is received through Cassini's High Gain Antenna (HGA), which must therefore be pointed towards Huygens throughout the descent.

In the original mission scenario, HGA pointing updates were unnecessary, because the geometry hardly changed during the mission. The geometry changes rather rapidly with the new mission scenario. So the HGA pointing must be updated at regular intervals. The entire spacecraft must be aligned with the LOS, because the HGA is fixed to the Cassini body. The HGA will be pointed towards Earth for downlinking the Probe data only after the end of the mission.

During the mission, the telemetry is transmitted redundantly on two channels operating at 2040 and 2098 MHz, respectively. These carrier signals contain the data on a phase-modulated sub-carrier. More detailed information can be found in the Huygens User Manual (HUM; Alcatel, 1997a).

The carrier frequency and the signal-to-noise ratio of the received signal are measured in the Huygens dedicated receiver section ("Probe Support Avionics", PSA) aboard Cassini. The carrier frequency measurement is performed in a Phase Locked Loop (PLL) using an identical oscillator as in the transmitter section and subtracting its frequency from the frequency of the incoming signal. These data are stored in the PSA-HK data along with other receiver parameters, e.g. link status bits, and transmitted to Earth after the end of the Huygens mission as part of the Huygens data stream.

DWE uses the carrier frequency Doppler excess f_D, the difference between

the transmitted and the received frequency, to measure the altitude profile of the zonal wind speed. The magnitude of the expected zonal wind speed could extend up to several hundred meters per second. As $f_D/f_0 = -v/c$ (f_0: transmitted frequency; see Sec. 5.1), the accuracy $\delta f/f_0$ of both the transmitted signal's frequency and the frequency measurement must be significantly better than 10^{-8} in order to measure velocities below 3 m s^{-1}, even if the zonal direction was aligned with the LOS.

The accuracy of oscillators is generally limited by an unpredictable frequency offset from the nominal output frequency and by frequency drift. On Cassini/Huygens, a slow "long-term" drift over several years may alter the frequency offset and induce a systematic error in the zonal wind speed recovery. A relatively fast "short-term" drift over the duration of the Huygens mission, approximately 2 to 3 hours, would be indistinguishable from a Doppler excess caused e.g. by zonal wind. Furthermore, an oscillator output frequency is usually affected by environmental impacts like mechanical stress or changes in temperature and pressure, which are expected to occur during the entry phase. Random measurement noise, on the other hand, can be reduced, at the expense of time (altitude) resolution, by integrating over as many frequency samples as necessary.

Learning that the short-term drift stability of standard quartz oscillators normally used in space missions is typically only 10^{-6}, it was deemed necessary to implement special ultra-stable oscillators (USO) in the Huygens radio system, which meet the stringent stability requirement over the entire range of expected temperatures and pressures. The DWE USOs were built by MBB (later taken over by DASA, since 1999 Astrium) in Ottobrunn, Germany. On the transmitter side, the Transmitter USO (TUSO) serves as the carrier frequency generator. On the receiver side, the Receiver USO (RUSO) is used to measure the received carrier frequency.

Only channel A operating at 2040 MHz is equipped with USOs, because a principle of the mission was that no experiment was allowed to have redundant equipment. The carrier frequency of channel B is generated and measured by standard temperature controlled crystal oscillators (TCXO) with a drift accuracy of 10^{-6}. TCXOs also serve as backup oscillators on channel A in case of a USO failure prior to the mission.

4.2 The USO Design and Performance

Detailed information about the USO specification, design and unit level performance is available from the DWE User Manual and from the Acceptance Data Packages (DASA, 1996) and test reports for the various units. This chapter summarizes the most important features, which are essential for understanding the following chapters.

A DWE USO produces an output frequency of 10 MHz, as required by the Huygens radio system. Its output signal is internally locked to the ground state hyperfine transition of Rubidium (Rb). Rb is easy to heat and thus able to accommodate the originally required fast warm-up time of 30 min. Another major driver for the use of Rb was its insensitivity to mechanical loads expected during the Huygens entry phase. Huygens is the first deep space mission operating Rb oscillators (Bird *et al.*, 1997a; 1997b; Kohl *et al.*, 1997; 1998a; 1998b).

Internal lock is achieved by converting the USO output frequency to the frequency of the Rb ground state hyperfine transition and looping this reference signal back to the USO internal Rb cell. The Rb gas in the cell is heated and excited by a Rb lamp. After crossing the Rb cell, its light is detected by a photo cell. When the USO output frequency is in lock with the Rb ground state hyperfine transition, the Rb gas becomes optically thick, because the Rb atoms resonate in the field of the reference signal. The intensity decrease at the photo cell, however, is less than 1%. For this reason, a DC detection is not suitable. Instead, the output frequency is modulated with a servo frequency of $f_{servo} = 135.63$ Hz, which is derived from the USO output frequency by dividing the USO output frequency (10 MHz) by 73728. This modulation produces a modulation of the photo detector output current. If the USO is internally locked and the photo current is thus minimum, both increasing and decreasing the output frequency cause the photo current to increase. The modulation frequency of the photo cell output current is then twice the original modulation frequency. This doubling of the photo current modulation is used as lock indicator (DASA, 1996). Fig. 4.1 shows the DWE-USO block diagram.

Using this technique, it was possible to achieve a high frequency stability over the entire range of expected temperatures and pressures. The power of spurious modulations, among these being the modulation at f_{servo}, could be kept below -65 dBc (65 dB below carrier level at 10 MHz) as specified.

However, during acceptance testing of the USOs, not all of the required specifications could be met. The warm-up time until lock slightly exceeded the specification of 30 minutes at initial USO temperatures below -20 C°. Thermal models developed by DASA, however, suggest that such low tem-

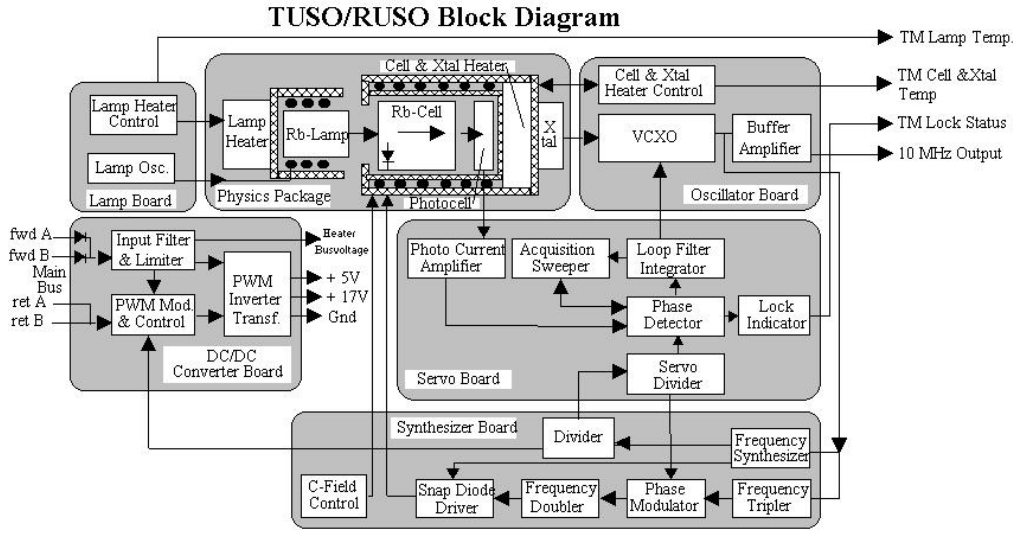

Figure 4.1: DWE-USO functional block diagram.

peratures were highly unlikely during the Huygens mission, either inside the PSA (RUSO) or inside the Probe (TUSO).

The short-term frequency drift behavior, specified not to exceed $2 \cdot 10^{-10}$ after 30 minutes, meets this requirement only after two hours of operation. For operation times shorter than two hours, the specification was exceeded by a factor of up to 4 in the temperature range expected during the Huygens mission. The noise specification was also slightly exceeded.

The frequency measurement noise, defined as the Allan deviation (Allan *et al.*, 1997), was specified not to exceed 10^{-11} with a 1-sec integration time. The unit now used as TUSO exceeded this limit by a factor of 5; the RUSO exceeded it by a factor of 2. All these nonconformances were acceptable for DWE. Fortunately, the crucial frequency parameters: offset, drift and noise, were virtually independent of environmental conditions (DASA, 1996).

Various USO models have been built in the course of the program. Fully functioning models are the two Engineering Models (EM), the Qualification and Flight Spare model (QFS) and the two Flight models (FM). As the QFS exhibited a slightly higher drift stability than the unit originally intended for use as the TUSO-FM, it was decided before integration to exchange the units and to use the QFS as TUSO-FM. The original TUSO-FM is now used as RUSO in the Huygens-EM, which is located at ESOC for ground tests and in-flight test preparation. The TUSO-EM serves as TUSO on the Huygens-EM and the original RUSO-EM is located at the University of Bochum in Germany (CoI-Institute) for unit level tests.

4.3 The USO Integration

After integrating the USOs into the Cassini/Huygens radio system (Fig. 4.2), it was found that a number of USO performance parameters actually depend

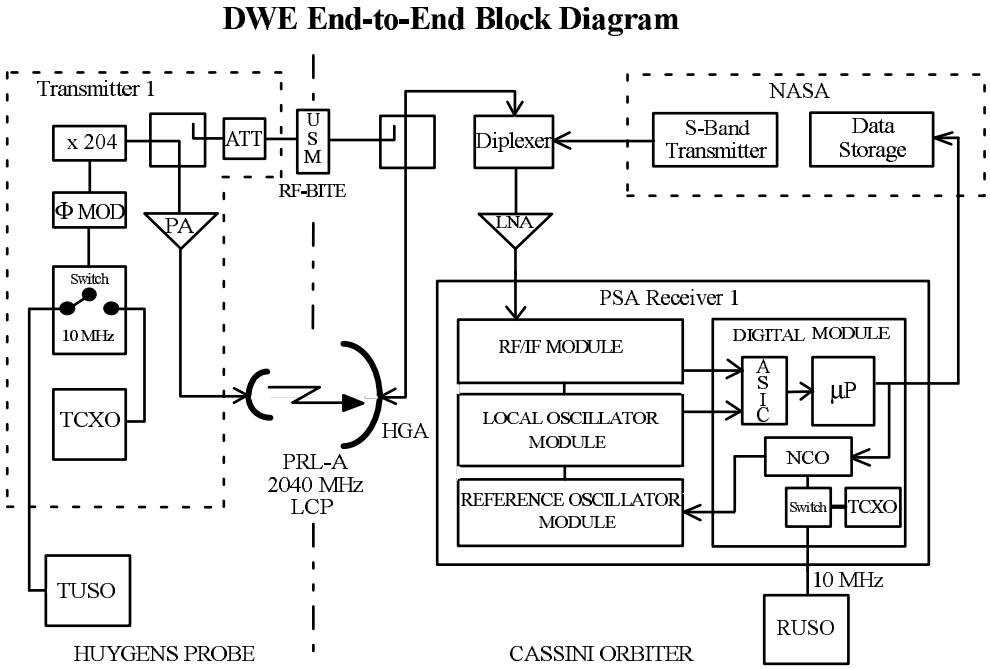

Figure 4.2: The Huygens radio system.

on the manner of the USO implementation. The noise of the frequency measurement, for instance, is not only a hardware feature, but depends on the way it is measured. During unit level tests, the signal was integrated over a certain amount of time (1 sec and 10 sec) by basically counting cycles. In the Huygens radio system, however, the frequency is measured in a PLL, which is updated internally at a rate of approximately 1 kHz. Unfortunately, only eight of these updates are written to the DWE dedicated PSA-HK data each second. This led to significant degradation of the noise performance.

System level tests using USOs and standard TCXOs show virtually identical noise behavior. The noise of the carrier frequency measurement is dominated by the PLL and virtually independent of the oscillator characteristics. The frequency noise at system level had been specified not to exceed $5 \cdot 10^{-10}$ at a 1-sec integration time, 50 times higher than the corresponding specification for the USOs. As shown below, this is about the measured noise level of the carrier frequency data, regardless of which oscillator (USO or TCXO) is used.

In principle, the USO output frequency ($f_{USO} = 10$ MHz) is upconverted to $f_0 = 2040$ MHz, the operating frequency on channel A, by a simple multiplication ($f_0 = f_{USO} \cdot 204$). However, as outlined above, f_{USO} is modulated by a servo signal at a frequency $f_{servo} = 135.63368$ Hz. f_{USO} may be written as

$$f_{USO} = f_{USO,0} + A_{osc} \cdot \cos(2\pi \cdot f_{servo} \cdot t) \tag{4.1}$$

where $f_{USO,0}$ is the nominal USO output frequency (10 MHz), A_{osc} is the amplitude and t is the time. At unit level, the power of the servo signal, which determines the amplitude A_{osc}, is less than -65 dBc.

It is clear from Eq. (4.1) that a multiplication of f_{USO} by 204 also increases the amplitude of the servo signal by the same amount. At S-band, the modulation amplitude is thus 204 times stronger than at 10 MHz. This corresponds to an increase in power (amplitude^2) by 46.2 dB. The effective spurious servo line power after integration into the Huygens radio system is -19.2 dBc for the receiver and -28.7 dBc for the transmitter.

The effect of these rather high spurious emissions is an oscillation of the measured carrier frequency. As the sampling rate for the carrier frequency is $f_{sample} = 8$ Hz (Nyquist frequency = 4 Hz), an oscillation at a frequency of 135.63368 Hz cannot be resolved. It is instead aliased to f_{osc}= 0.36632 Hz ($f_{osc} = 17 \cdot f_{sample} - f_{servo}$).

During AIV testing of the Huygens-FM at DASA in 1996, this specification flaw led to a constant oscillation of the frequency measurement with an oscillation frequency $f_{osc} = (0.3663 \pm 0.0001)$ Hz and an amplitude $A_{osc} = (7 \pm 1)$ Hz peak-to-peak (p-p). The effect had no impact on the link performance and was barely visible above the noise level of the raw data.

4.4 The Link Performance in Flight

All experiments and the Huygens radio system have been regularly tested in flight since launch. The Probe checkouts (PCOs) take place approximately every six months. Eight checkouts have been performed so far (F1–F8; state: spring 2002). The DWE-USOs are tested during three out of four checkouts. Every fourth test (so far F2 and F6) is performed using the backup TCXOs as signal generators.

During a checkout, the data are routed through an umbilical connecting the transmitter aboard Huygens to the receiver aboard Cassini. It is thus clear that the signal is not Doppler shifted. The umbilical is disconnected at Probe separation by an Umbilical Separation Mechanism (USM; see Fig. 4.2).

In addition to the regular checkouts, several Probe Relay Tests (PRTs) have been performed to test the Huygens dedicated receiver aboard Cassini and to calibrate the received signal level. For these tests, a signal simulating Huygens is uplinked to Cassini from an Earth-based DSN antenna. Huygens itself is dormant. It was the first PRT which revealed a design flaw in the decoding section and led to the redesign of the Huygens mission.

DWE receives no dedicated science data from Huygens, but rather evaluates the PSA-HK data, which contain the received carrier frequency, the signal level and several RUSO parameters like internal lock status, temperatures and power consumption. In addition, link performance parameters are evaluated to check the quality of the link. The corresponding TUSO parameters are read from the Probe-HK data.

The carrier frequency is returned as the residual between the received frequency and a reference frequency f_{ref}, which is nominally equal to the transmitted frequency $f_0 = 2040$ MHz. Furthermore, the reference frequency may be shifted by approximately 38.5 kHz to account for the expected high Doppler shift in the original mission scenario. The key measurement for DWE is thus a frequency f_R with

$$f_R = f_0 + f_D - (f_{ref} + f_{comp}) \tag{4.2}$$

where f_0 is the transmitted frequency, f_D accounts for all possible Doppler shifts imposed on the link, f_{ref} is the reference frequency, f_{comp} is the built-in Doppler compensation, which is either ~ 38.5 kHz (original mission scenario) or 0 Hz (PCO mode). It is likely that f_{ref} and f_0 differ slightly by a frequency f_{off}. To account for this possible offset, f_{ref} may be written as

$$f_{ref} = f_0 - f_{off} \tag{4.3}$$

Eq. (4.2) can thus be rearranged to

$$f_R = f_D - f_{comp} + f_{off} \tag{4.4}$$

The following subsections give an overview of the most important results from the in-flight tests regarding the DWE performance. Detailed information on telemetry and test performance may be found in the TM/TC Data Tables (Alcatel, 1997c) and in the DWE Test Reports (Dutta-Roy, 1996-2002).

4.4.1 Spurious Emissions

After the mating of Cassini and Huygens, the behavior of the frequency oscillation phenomenon changed dramatically. In all PCOs and PRTs performed so far and in the only system test in mated configuration prior to launch using the USOs, the amplitude of the frequency oscillation varied between 6 and a maximum of 30 Hz p-p. Fig. 4.3 shows the appearance of this phenomenon for all PCOs performed with USOs to date. The thickness of the lines is a measure for the oscillation amplitude. The sinusoidal shape of the oscillation itself is not resolved at this time scale. The checkouts are performed approximately every six months. The backup TCXOs were used as carrier frequency generators in F2 and F6.

The effect could be driven by another spurious signal coupling with the carrier signal or with the servo signal directly. A possible origin could be the Bus Interface Unit (BIU) which connects the PSA to the Cassini CDS bus. The BIU is driven at 8 Hz and has thus a harmonic at 136 Hz. Furthermore, it was not installed before the mating of Cassini and Huygens. Due to the lack of testing capabilities, it is, however, impossible to arrive at a definite conclusion regarding the source of this phenomenon.

Fortunately, the effect does not seriously degrade the link performance. At maximum observed oscillation amplitudes, the effect decreases the signal level by 0.5 dB (Dutta-Roy, 1997 and 1998). Special tests on the Huygens-EM have shown that an impact on the link performance (sideband lock on $f_0 + f_{servo}$, but frame decoding still possible) occurs at an oscillation amplitude above 50 Hz p-p. Ironically, the phenomenon decreases slightly at lower signal-to-noise levels.

Fig. 4.4 shows the one-sided normalized power spectrum of f_R measured during F8 (Fig. 4.3, last panel) between t_0 and $t_0 + 150$ min. The time averaged spectra of all in-flight PCOs look virtually identical. The most prominent line, which is responsible for the large frequency oscillation amplitude, is located at 0.3672 ± 0.0001 Hz. The slight offset with respect to the theoretical value of 0.3663 Hz for f_{osc} can be explained by the behavior of the CDMU clock, which governs the sampling rate of the Huygens data and has a positive relative offset of $\sim 10^{-5}$ with respect to its nominal value. Numerous other lines f_{ijk} are visible in Fig. 4.4 which can be described by

$$f_{ijk} = \pm i \cdot 1\text{Hz} \pm (j \cdot f_{osc} \pm k \cdot f_{osc_2}) \tag{4.5}$$

where i, j and k are integers, $f_{osc} = 0.3672$ Hz and $f_{osc_2} = 0.5 \cdot (1+1/100) \cdot f_{osc}$. The frequency f_{osc_2} is most probably a modulation of f_{osc}, because it is not present when $j = 0$ (it does not couple to the spurious emissions at $i \cdot 1$ Hz directly).

The term in parentheses in Eq. (4.5) can already be seen in the spectra of pre-mating system tests. The amplification of the oscillation amplitude after the mating is associated with the appearance of spurious lines at $i \cdot 1$ Hz. This is further evidence that the BIU is the source of the spurious amplification, because the PSA data have a frame rate of 1 Hz.

Fig. 4.5 shows the F8 frequency measurement and its dynamical spectrum as a contour plot with a time resolution of 1 min. The variation of spurious lines with the oscillation amplitude can be seen in this graph. Moreover, an unexplained pattern appears between $t_0 + 135$ and $t_0 + 165$ min, which occurred in several other in-flight PCOs, however not at the same time. Certain spurious lines were strongly amplified during this period. This feature cannot be seen in the time domain, because it is dominated by the oscillation at f_{osc}.

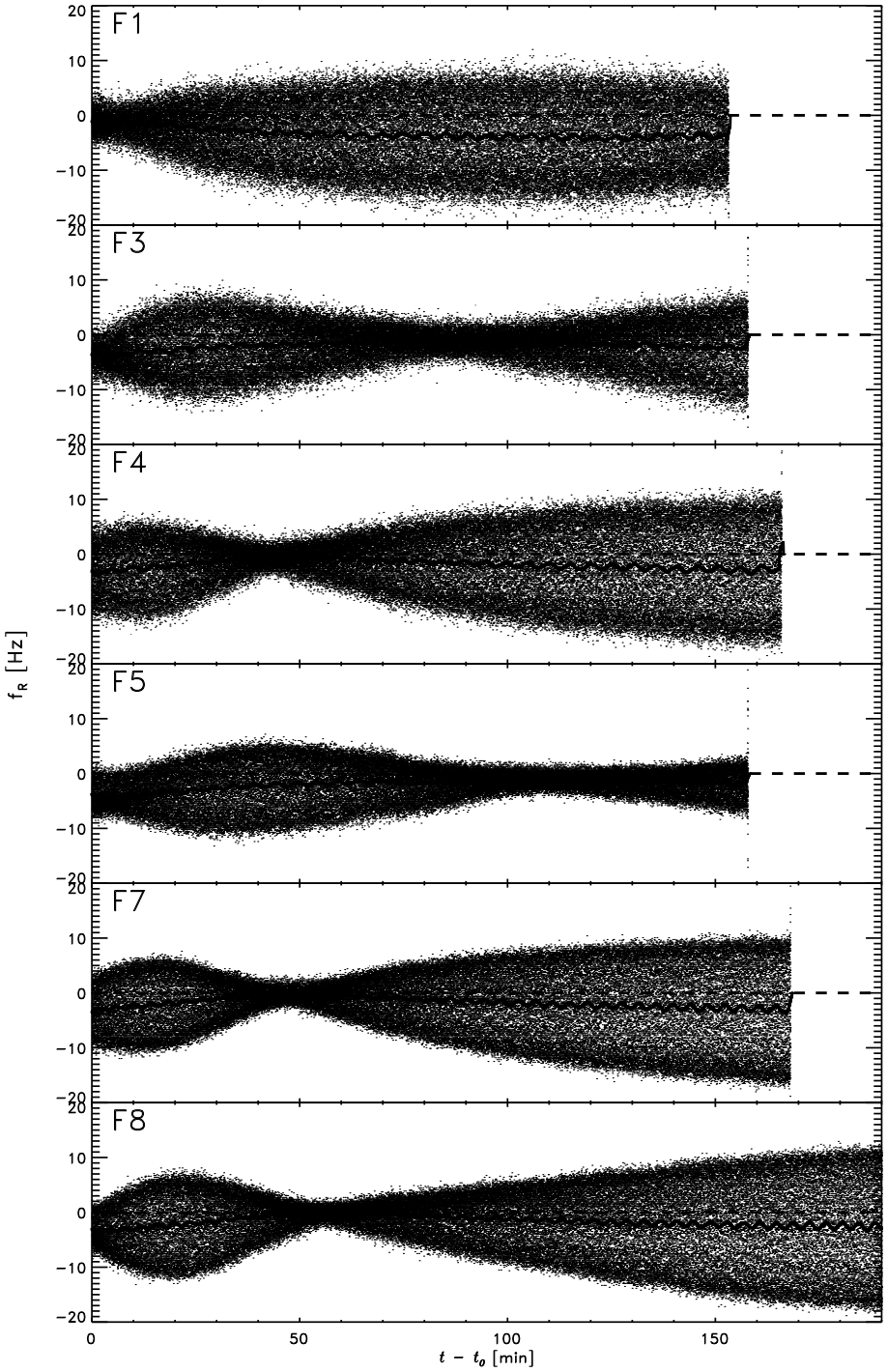

Figure 4.3: Frequency measurements (f_R) during Probe checkouts. The raw samples are displayed as dots. The solid thick line is a 1-minute running mean of the samples.

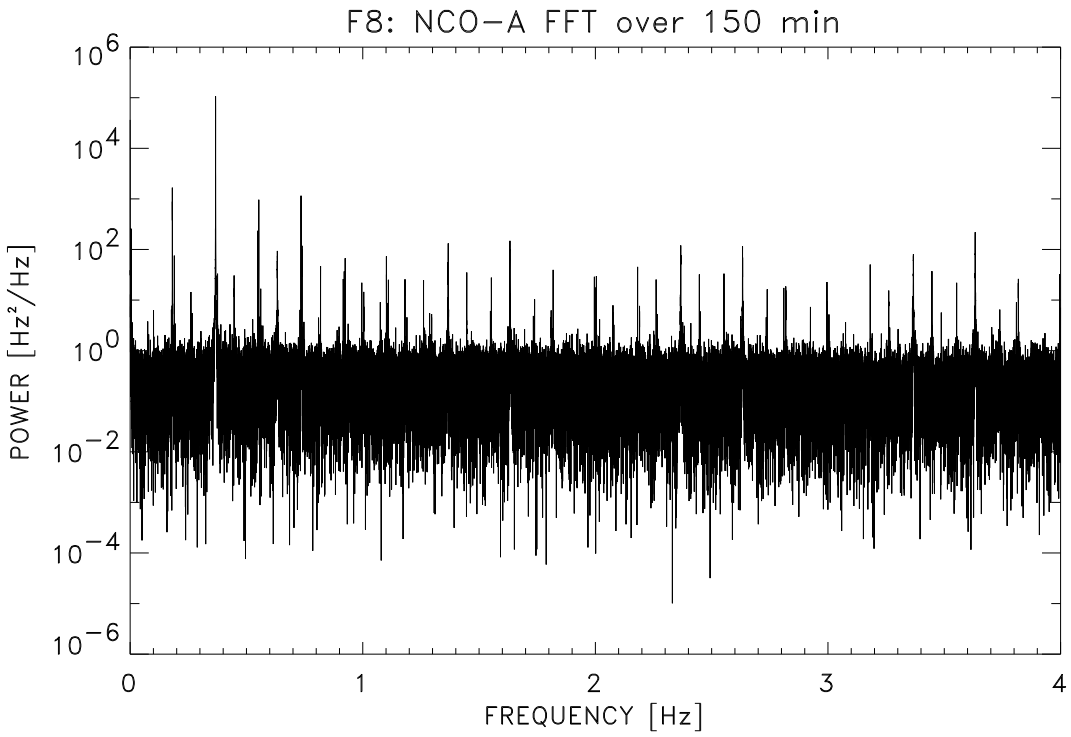

Figure 4.4: One-sided normalized power spectrum of frequency measurement during F8. The time window extends from t_0 until $t_0 + 150$ min.

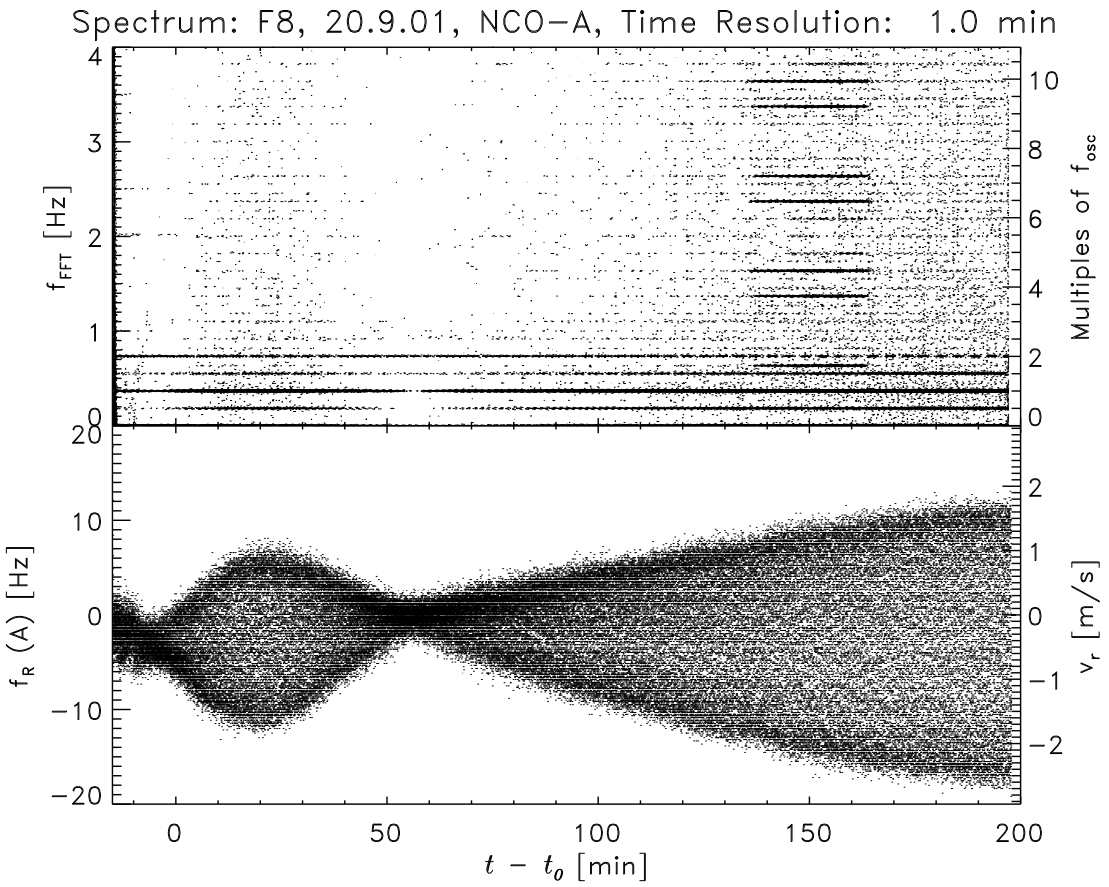

Figure 4.5: Frequency measurement (f_R) during F8. The lower panel shows the frequency measurement in the time domain and the upper panel shows a dynamic power spectrum of this measurement as a contour plot with a time window of 1 minute. The ordinate on the right side shows f_R converted to LOS velocity and f_{osc} converted to multiples of f_{osc}, respectively.

4.4.2 Noise Performance and Calibration

In the original Huygens mission scenario, the PRL would have been blue-shifted by more than 38 kHz for almost the entire mission duration. As the bandwidth of the carrier tracking loop is only ±30 kHz, this fact made a Doppler compensation necessary for the Huygens mission ("Mission Mode"). The built-in Doppler compensation was designed to compensate for 38.5 kHz. The accuracy of this value (f_{comp}) was, however, unclear.

The third PRT, performed in June 2001, provided an opportunity to calibrate f_{comp} using two switches from "Mission mode" to "Checkout mode" (Doppler compensation switched off), which is not possible in a regular checkout. Fig. 4.6 shows one of those switches. Before the switch, the receiver

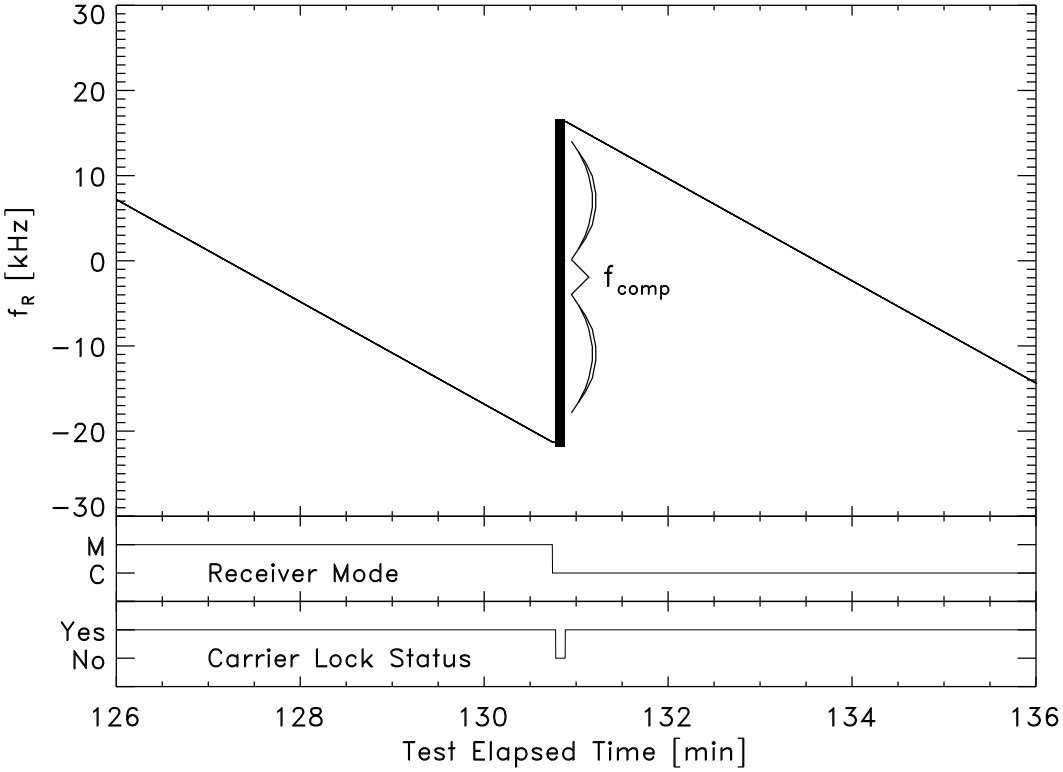

Figure 4.6: Calibration of f_{comp}.

was set to Mission mode and the received frequency was observed to decrease roughly linearly with time. Before reaching the lower edge of the bandwidth (−30 kHz), the receiver was commanded to Checkout mode. The switch caused a link interruption of 10 sec. A linear regression was applied to the frequency measured five minutes before and after the switch. The two resulting lines had virtually identical slopes and f_{comp} was calculated by the

difference between the two lines at the time of the switchover. Using two independent switching events on the same day, f_{comp} could be calibrated to $38,504.1 \pm 0.2$ Hz (Dutta-Roy, 1996-2002).

However, due to the design flaw in the PSA that led to the redesign of the Huygens mission, it has now been excluded that the "Mission mode" will be used during the Huygens mission. Although the Cassini trajectory is not yet finalized, all viable alternatives differ only marginally and do not foresee Doppler shifts of more than 17 kHz.

A possible offset f_{off} between the transmitted frequency f_0, generated by the TUSO, and the reference frequency f_{ref}, generated by the RUSO, is of more concern for the DWE. It can be seen in Fig. 4.3 that the offset is apparently correlated to the frequency oscillation amplitude. Fig. 4.7 provides a more detailed analysis of the F8 frequency measurement. The second panel shows the p-p oscillation amplitude A_{osc} averaged over one minute. The third panel shows the offset of the frequency measurement f_R (panel 1), calculated as a 5-min running mean and plotted inversely to make the correlation more obvious. This parameter is equal to the f_{off} in Eq. (4.4), because f_D and f_{comp} have a value of 0 Hz during a PCO. The fourth panel shows the Allan deviation, which is also correlated to the oscillation amplitude. The Allan deviation has been calculated by integrating f_R over 1 second and using 100 integrated samples. It can be seen that the Allan deviation is $\sim 2 \cdot 10^{-10}$ when the oscillation is at a minimum. This is slightly better than the specification at system level, but far from the specification at USO level.

The correlation between the frequency offset f_{off} and the oscillation amplitude A_{osc} apparently does not exist during the first 30 minutes. The reason for this behavior may be the fact that the TUSO is not yet fully warmed up. Skipping those first 30 minutes, the correlation analysis gives a linear relation between A_{osc} and f_{off} ($f_{off} = -0.104 \cdot A_{osc} + (0.353 \pm 0.100)$ Hz). Combining the analysis results of all in-flight PCOs with DWE participation except F1, the correlation may be written as

$$< f_{off} >= -0.09 \cdot A_{osc} - 0.14 \text{ Hz} \pm 0.65 \text{ Hz} \qquad (4.6)$$

This result is displayed in Fig. 4.8. Eq. (4.6) will, of course, be updated after each future PCO.

The error of ± 0.65 Hz includes the calibration error as well as random noise. The least significant bit of the frequency telemetry word corresponds to a frequency of 0.0484 Hz. The digitization error may therefore be neglected, as this value is much smaller than the actual noise. The frequency noise increases also with decreasing signal-to-noise level. The correlation is weak, however, in the signal-to-noise range expected during the Huygens mission.

The TUSO spurious at 135.6 Hz signal might not fall significantly into the narrow tracking bandwidth of the receiver carrier-recovery-loop (25 Hz), which represents a low-pass filter for the input phase jitter. However, the same receiver carrier-recovery-loop represents a high-pass filter for the RUSO spurious. Furthermore, the phenomenon of the oscillating carrier frequency in PCOs showed virtually identical behavior during the PRTs, where Huygens is dormant. These facts indicates that the effect is generated inside the receiver and justifies the use of Eq. (4.6), which is derived from PRT frequency measurements, to correct the frequency measurement obtained during the Huygens mission. The PRTs, where the receiver including the RUSO were used over a period of eight hours, also showed that the oscillation amplitude stabilizes and assumes a constant value after about 3-4 hours of operation.

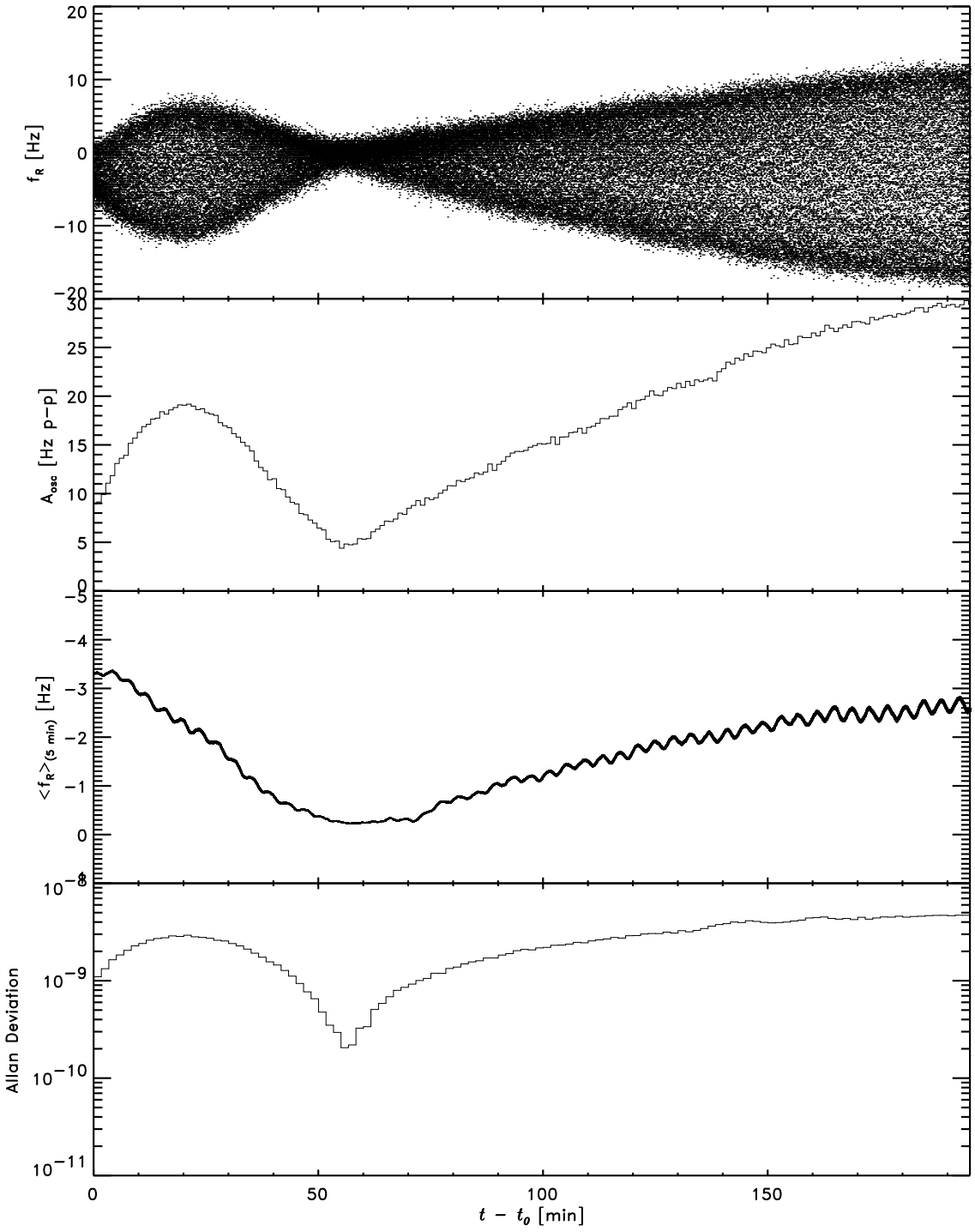

Figure 4.7: Analysis of F8 frequency measurement.

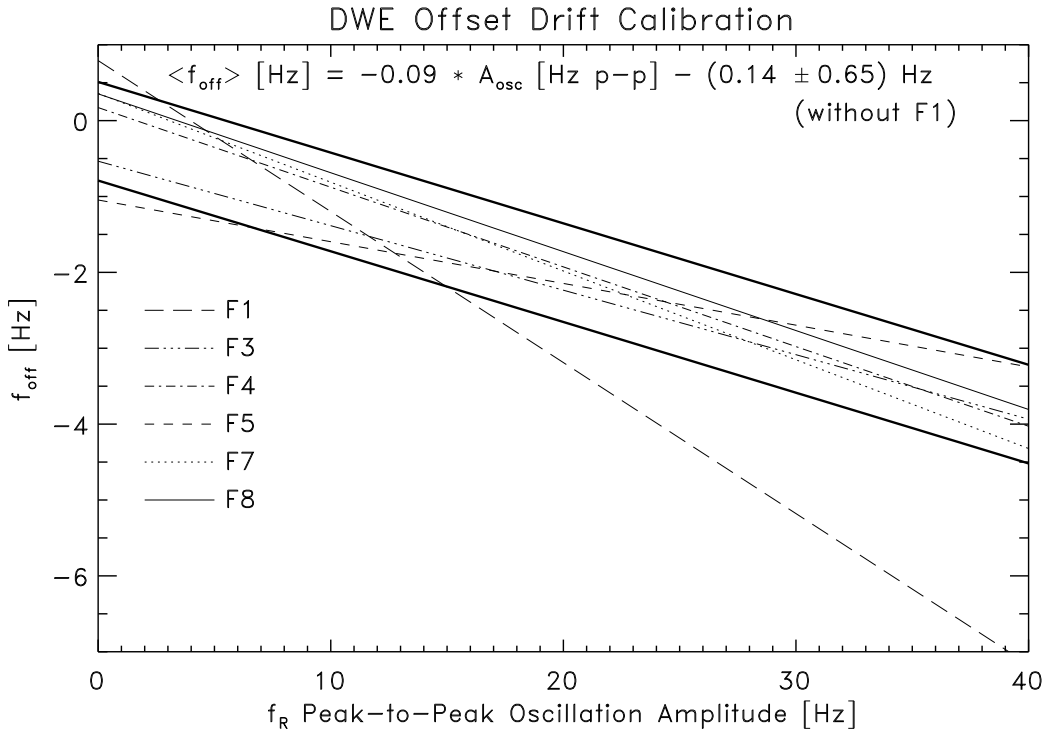

Figure 4.8: f_R offset calibration. The thick lines mark the correlation line ± 0.65 Hz.

Chapter 5

The Wind Retrieval Algorithm

5.1 Introduction and Basics

DWE works on a simple principle: It utilizes the PRL carrier signal to derive a velocity measurement from its Doppler shift. Relative motion between transmitter and receiver affects the frequency measurement according to the following relativistic Doppler formula:

$$f_R = f_T \cdot \frac{\sqrt{1 - \frac{v^2}{c^2}}}{1 + \frac{v}{c} \cdot \cos\alpha} \tag{5.1}$$

Here, f_R and f_T are the received and transmitted frequencies, respectively, $v = \mid \vec{v} \mid$ is the relative speed between transmitter and receiver, α is the angle between the LOS and the relative velocity vector $\vec{v}$ and c is the speed of light.

Considering the velocities of Cassini and Huygens, the factor v/c is smaller than 10^{-5} throughout the descent. This means that the second order relativistic effects can be neglected. At $f_T = 2040$ MHz, they contribute to a frequency shift of less than 0.2 Hz (or 3 cm s^{-1}), less than the achievable accuracy, as will be shown later.

Eq. (5.1) may thus be simplified to

$$f_R = f_T \cdot (1 - \frac{v_{LS}}{c}) \tag{5.2}$$

where v_{LS} represents the LOS component of the relative velocity between transmitter and receiver ($v_{LS} = v \cdot \cos\alpha$). The Doppler excess frequency f_D is then given by

$$f_D = f_R - f_T = -f_T \cdot \frac{v_{LS}}{c} \tag{5.3}$$

The parameters f_R and f_T of Eq. (5.3) are time dependent, and f_R is retarded with respect to f_T due to the one-way light time between Cassini and

Huygens. However, considering the distance between Huygens and Cassini, which varies between 76,000 and 65,000 km during the Huygens mission, the retardation time is less than 250 msec and may therefore be neglected.

With the results of Section 4.4, the DWE frequency data are evaluated in a straightforward way by (1) hardware drift compensation by applying the calibration, (2) filtering spurious modulations by integration and, of course, (3) extracting all Doppler contributions other than zonal speed. The other Doppler contributions, which are the Cassini velocity and the meridional and descent velocities of Huygens, have to be determined by other means for an unambiguous zonal wind recovery. The crucial point for DWE is the accuracy to which these steps can be performed. In this chapter, all known sources of inaccuracy and their impact on the DWE determination of Titan's zonal wind speed are investigated.

5.2 Earlier Efforts

The idea of measuring atmospheric motion by utilizing the Doppler shift of the relay link between an atmospheric entry vehicle and a receiving station is not new. There have been previous DWEs on Venus (Counselman *et al.*, 1979) and Jupiter (Atkinson, 1989). Each of these experiments had unique environmental and geometric conditions as well as unique oscillator and radio system characteristics. The atmosphere of Mars is too thin for this kind of experiment, but wind velocities have been determined by other means (Seiff, 1993).

The experiment most similar to the Huygens-DWE was performed in 1995, when the spacecraft Galileo dropped a probe into Jupiter's atmosphere. Like Huygens, the Galileo Probe sent the data measured during its descent via a PRL to the Galileo Orbiter, thereby enabling wind measurements. Atkinson (1989) developed an algorithm for the Galileo-DWE zonal wind recovery on Jupiter. As a side product, he also introduced a method to recover the zonal winds on Titan. However, the Galileo-USOs were ordinary quartz oscillators. The stability of quartz USOs is adequate, but their absolute output frequency is subject to environmental conditions. Thus, the zero frequency offset between transmitter and receiver was unknown at the time of the Galileo Probe mission. Due to this restriction, the algorithm developed for Jupiter requires a rapidly changing observation geometry. Furthermore, *a priori* assumptions must be made about the zonal wind behavior. On the other hand, the Atkinson algorithm developed for Titan, the so called Direct Method, assumes an essentially constant observation geometry as foreseen in the old mission scenario. In both cases, the errors resulting from inaccurate knowledge of the geometry were assumed to be noncritical.

It will be shown that the geometric inaccuracies are, in fact, dominant for the Huygens-DWE and cannot be neglected. However, the USOs of the Huygens-DWE are regularly tested during the cruise to Saturn and the frequency offset between transmitter and receiver is a well-known value. The invariance of the Rb absorption resonance guarantees that the frequency offset is not affected by the environmental conditions expected during the entry phase, as has been shown in various tests prior to launch (Dutta-Roy, 1996-2002). The subsequent sections demonstrate how this critical advantage can be exploited to retrieve the zonal wind velocity in an even more "direct" way.

5.3 Correspondence between Probe and Wind Velocity

5.3.1 Probe Response Time

The algorithm outlined hereafter recovers the Huygens zonal velocity, but not necessarily the zonal wind speed. Huygens has mass and therefore inertia, consequently it will react with a certain delay to changes in the wind speed.

Atkinson (1989) showed that the probe response to horizontal wind gusts of relative velocity w_H is given by

$$\vec{v}_{pr,H}(t) = \vec{w}_H[1 - \exp(-\frac{g}{v_T}t)] \tag{5.4}$$

Here, $\vec{w}_H$ is the relative velocity of a step like wind gust occurring at $t = 0$ and $\vec{v}_{pr,H}$ is the probe relative velocity at time t after the wind gust. g represents the local gravitational acceleration and v_T, the terminal descent velocity, is given by

$$v_T = \sqrt{\frac{2mg}{C_D A \rho}} \tag{5.5}$$

(m: probe mass, C_D: probe/parachute drag coefficient, A: probe/parachute effective cross sectional area, ρ: atmospheric density). It is thus possible to define a horizontal wind gust characteristic time $\tau_H = v_T/g$ ("Probe Response Time") and a characteristic length $l_H = v_T\tau_H = v_T^2/g$. A wind gust that appears and disappears in a spatial layer smaller than l_H will have only little effect on the overall probe velocity. It may, however, induce a pendulum motion, because the individual drag coefficients for the probe and the parachute are very different.

Effectively, the probe is continuously accelerated in response to the constantly varying horizontal winds. To represent the probe horizontal velocity as a function of the horizontal wind velocity correctly, the Atkinson formalism can be extended in the following way:

$$\vec{v}_{pr,H}(t) = \vec{w}_H(t_0) + \int_{t_0}^{t} \frac{d\vec{w}_H(t')}{dt'}[1 - \exp(-\frac{g(t')}{v_T(t')}(t - t')]\, dt' \tag{5.6}$$

This formula assumes that the horizontal probe velocity $\vec{v}_{pr,H}$ equals the horizontal wind velocity $\vec{w}_H$ at the time $t = t_0$. The term in brackets under the integral is the probe response function, which acts like a weighting function for different times t'.

In general, a true signal $u(t)$ is smeared out or distorted by the imperfect instrument response. The resulting signal $s(t)$ is the result of a convolution

with the instrument response function $r(t)$.

$$s(t) = \int_{-\infty}^{\infty} u(t')r(t-t')\,dt' \tag{5.7}$$

Usually, the measurements $s(t)$ may be easily deconvoluted by using Fourier transforms (Press *et al.*, 1992). However, the response function in Eq. (5.6) depends not only on $(t-t')$ but also on t' alone. The characteristic time $\tau_H = v_T/g$ is a function of the time or altitude, respectively. This fact prevents a straightforward deconvolution of the DWE signal.

If, however, the response function is close to unity, then the horizontal probe velocity may directly be translated to horizontal wind velocity. In fact, the response function in Eq. (5.6) is close to unity for times $t-t' \gg \tau_H$. Thus, if the step size for the integration is chosen large enough, the response function may be approximated by unity.

During the descent, the Huygens descent module (probe + parachute) drag coefficient C_D will vary between 0.78 and 0.86, according to the local Reynolds number. Its mass is 207.6 kg before main chute separation and 202.4 kg thereafter. The effective area is 55.44 m^2 and 8.57 m^2 before and after main chute separation, respectively (Alcatel, 1997b). Given these values, it is possible to calculate the Huygens Probe response time for the descent. Table 5.1 shows the evolution of the terminal velocity, the Probe response

Table 5.1: Huygens Probe response time during descent

$t-t_0$ [min]	Altitude [km]	ρ [kg m^{-3}]	v_T [m s^{-1}]	τ_H [sec]	l_H [m]
1	152	$5.0 \cdot 10^{-3}$	47.7	39.5	1883.6
14	115	$1.45 \cdot 10^{-2}$	28.4	22.9	650.6
15	112	$1.59 \cdot 10^{-2}$	Main chute separation		
16	109	$1.73 \cdot 10^{-2}$	65.2	52.3	3408.8
30	64	$1.38 \cdot 10^{-1}$	23.5	18.2	427.0
60	32	1.15	8.2	6.2	50.8
90	16	2.75	5.3	4.0	21.4
120	5	4.45	4.2	3.1	13.0
135	0	5.52	3.8	2.8	10.9

time and the characteristic length during the Huygens mission. It should be noted that the atmospheric density ρ is taken from the LH model, which has an uncertainty of about 10% in the relevant altitude range. Furthermore, the mass estimates may be altered by ablation and icing. The Probe response

time should thus not be considered as exact. The basic result from this calculation is that the Probe response time is longer than 3 seconds for virtually the entire descent.

5.3.2 Wind Gusts and Parachute Swing

Sudden changes of the wind velocity may set Huygens swinging under the parachute. If this motion has a contribution along the LOS, it will induce a Doppler shift on the received signal. The effect is limited by the Probe response time, which acts as a low-pass filter on the gust function. The Probe-parachute system is designed to limit any pendular motion to an amplitude of 10° and to quickly damp such motions (Alcatel, 1997a; Lorenz 1994). If the possible wind gusts are not significantly stronger than expected, it is therefore justified to assume that pendular motion may be neglected.

The HUM (Alcatel, 1997a) provides a rough model for wind gusts (amplitude and gradient vs altitude). From this model, we can estimate the scale of possible wind gusts (spatial scale = 2·amplitude / gradient). Table 5.2 is a

Table 5.2: Wind gust scales during descent

$t - t_0$ [min]	Altitude [km]	τ_H [sec]	Gust amplitude [m s^{-1}]	Spatial scale [km]	Temporal scale [sec]
1	152	39.5	21.0	9.0	120
14	115	22.9	10.5	4.0	107
15	112	Main chute separation			
16	109	52.3	9.9	3.8	52
30	64	18.2	15.0	3.3	103
60	32	6.2	10.0	3.5	315
90	16	4.0	10.0	5.3	736
120	5	3.1	10.0	6.5	1140
135	0.001	2.8	10.0	6.5	1226

supplement to Table 5.1 showing the Probe response time τ_H and the spatial scale of wind gusts in Titan's atmosphere with respect to mission time and altitude. The temporal scale is given by the spatial scale divided by the descent velocity. The main result of this rough estimate is that wind gusts can be fully resolved. Only right after main chute separation, the Probe response time may be too long for a full wind gust resolution. DWE can resolve only the LOS component of the wind gusts, because their horizontal direction is generally arbitrary. They are of considerable scientific interest, however, as they may indicate the presence of gravity waves (Hinson *et al.*, 1983), convective activity (Awal *et al.*, 1994) or the transition through a planetary boundary layer (Allison, 1992).

5.4 Integration

In Section 4.4, it was shown that spurious emissions on the carrier signal lead to an oscillation of variable amplitude with a period of 2.7 seconds. This fact and the effect of the Probe response time make it appropriate to integrate the measurement over several samples. The best strategy to filter out the spurious modulation effectively is to use a moving average filter with a width close to a multiple of the period of the most prominent spurious oscillation. Additionally, such a filter will reduce random noise on the signal. In fact, it can be shown that the moving average filter is the *optimal* filter for reducing noise while keeping the sharpest step response (Smith, 1997).

The moving average filter is implemented by modifying the frequency measurement $f(t)$ according to

$$\bar{f}(t_i) = \frac{1}{2k+1} \cdot \sum_{j=-k}^{+k} f(t_{i+j}) \tag{5.8}$$

The effect of a moving average filter can best be seen in its frequency response. Fig. 5.1 shows a typical filter function in the time domain. It represents an integration of 21 samples equal to 2.625 sec. This value was chosen, because 21 is the odd number closest to $2.7 \cdot 8$, the period of the frequency oscillation times the number of samples per second. Fig. 5.2 displays the one-sided, normalized power spectrum of the filter function. The rectangular pulse in the time domain corresponds to a *sinc*-function in the frequency domain with minima at frequencies close to multiples of the oscillation frequency $f_{osc} = 0.367$ Hz. These frequencies are effectively suppressed in this manner.

The Probe response time, however, is longer than 2.7 sec for the entire descent. Additionally, as shown in Subsection 4.4.1, a rather strong spurious emission is present on the signal at $f_{osc} \approx 0.367/2$. Thus, an alternative solution is to integrate the signal over approximately 5.4 sec (≈ 43 samples). At altitudes above 50 km the integration time may be even larger.

The moving average filter also reduces the noise of the frequency measurement by a factor $\sqrt{N}$, where N is the number of summed samples. The altitude resolution is hardly affected by this technique as long as the integration time is not longer than the Probe response time.

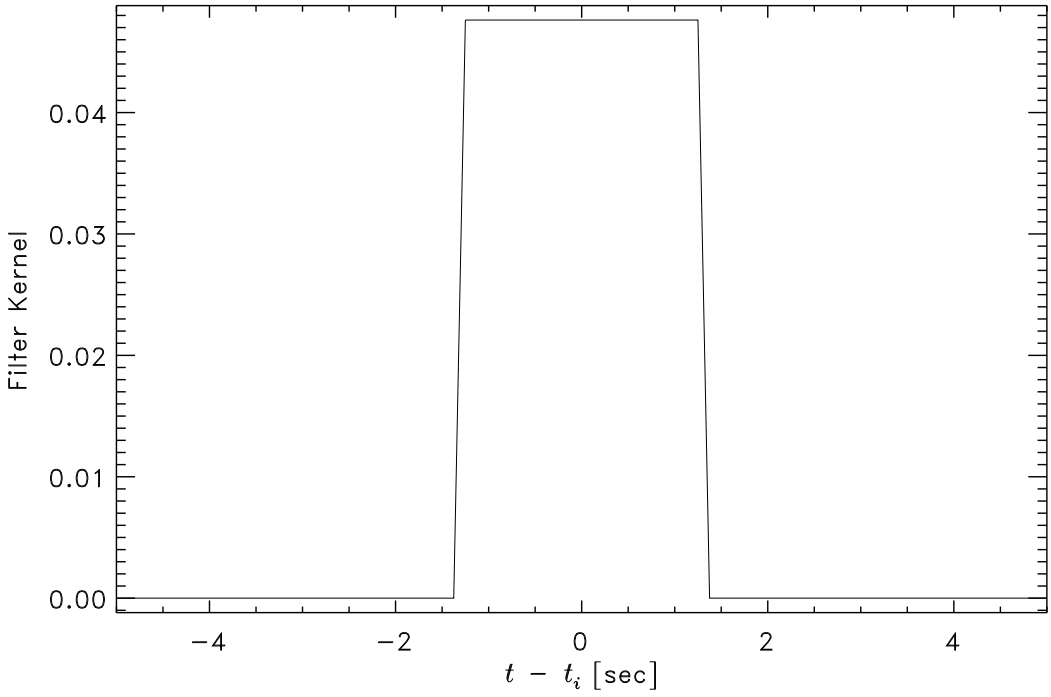

Figure 5.1: Moving Average Filter Function. The integration is performed over 21 samples equivalent to 2.625 sec. t_i is the time tag of the ith frequency sample.

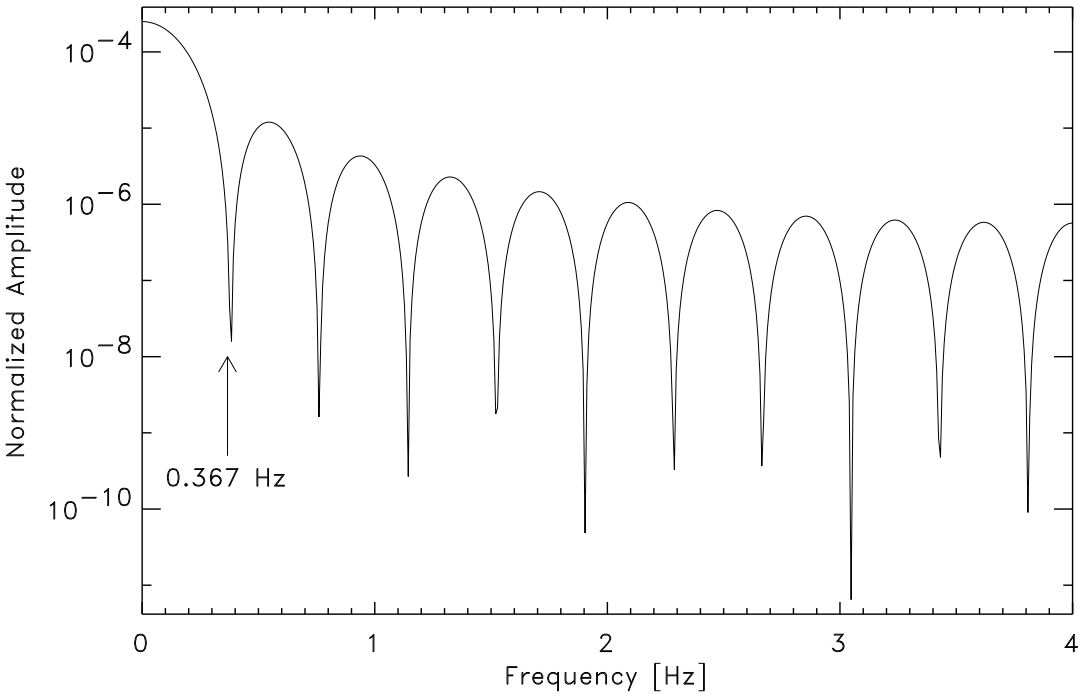

Figure 5.2: Frequency Response (FFT) of Moving Average Filter Function displayed in Fig. 5.1.

5.5 Propagation Effects

5.5.1 Refraction

As Huygens descends through Titan's atmosphere, the uplinked PRL signal is subject to refraction. The result is a weak attenuation of the signal level due to differential refraction (Bird, 1997) and a shift in frequency due to alteration of the phase path. Assuming straight line propagation, refraction alters the phase path according to

$$\phi = \frac{f_0}{c} \int_{x_H}^{x_C} (n-1)\, dx \tag{5.9}$$

where ϕ is the phase path increase, f_0/c is the inverse transmitted wavelength, x_H and x_C the locations of Huygens and Cassini, respectively, and n is the refractive index along the ray path (Fjeldbo *et al.*. 1965a and 1965b). The parameter $(n-1)$ is also known as refractivity R.

Refraction has an impact on the received frequency if ϕ varies with time. The frequency shift is simply the time derivative of the phase path ($f_{D,refract} = \partial\phi/\partial t$). For a rough assessment of the refraction effect during the Huygens mission, we set in Eq. (5.9) $dx = dz/\cos\gamma_{des}$, where dz indicates integration in the vertical direction. Additionally, setting γ_{des} constant to 80° allows us to pull it out of the integral. The refractive index n at the position of Cassini x_C is 0. $f_{D,refract}$ is then given by

$$f_{D,refract} = \frac{\partial\phi}{\partial t} = \frac{\partial\phi}{\partial z} v_{des} = \frac{f_0}{c \cdot \cos\gamma_{des}} R \cdot v_{des} \tag{5.10}$$

The refractivity of a neutral molecular gas R_m is given by

$$R_m = \frac{N_m \cdot R_{standard}}{L} \tag{5.11}$$

where N_m is the molecular density, L is the Loschmidt number and $R_{standard}$ is the refractivity at standard conditions (1 bar, 0°). For a gas consisting of several components, the refractivities are added according to their weight.

We calculated the refractivity of Titan's neutral atmosphere by assuming that it consists of 90% Nitrogen and 10% Argon.

$$R_{standard} = 0.9 \cdot R_{N_2} + 0.1 \cdot R_{Ar} \tag{5.12}$$

with $R_{N_2} = 2.933 \cdot 10^{-4}$ and $R_{Ar} = 2.775 \cdot 10^{-4}$ (Newell *et al.*, 1965). The molecular refractivity R_m follows from Eq. (5.11). For the calculation, we used molecular densities taken from the LH model of Titan's atmosphere.

The density and the resulting refractivity are displayed in Figs. 5.3 and 5.4 as a solid line.

The refractivity of Titan's ionosphere must also be considered. A reanalysis of Doppler data obtained from the Voyager I occultation in 1980 provided evidence that an ionospheric layer exists on Titan at about 1200 km altitude (Bird *et al.*, 1997). This finding confirmed models of Keller *et al.* (1992) and Ip (1990), which virtually do not differ quantitatively. Other models predict additional layers at about 100 km altitude (Borucki *et al.*, 1987) and at 550 km altitude (Grard, 1992).

The ionospheric refractivity is given by

$$R_e = \frac{-N_e \cdot r_e \cdot c^2}{2\pi \cdot f_0^2} \tag{5.13}$$

where N_e is the electron density, r_e is the classical electron radius and f_0 is the transmitted frequency. The electron density is displayed in Fig. 5.3 as a dashed line. The resulting refractivity is generally negative. Its absolute value is plotted in Fig. 5.4 as a dashed line. The total refractivity is the sum both the molecular and the electron refractivities.

With $\gamma_{des} = 80°$, the first factor on the right side of Eq. (5.10) $f_0/(c \cdot cos\gamma_{des})$ has a value of about 40 m^{-1}. The maximum refractivities near ground are around 10^{-3} and the descent velocity is of the order of 10 m s^{-1}. The frequency shift due to refraction is thus $\simeq$0.4 Hz, equivalent to a velocity of 6 cm s^{-1} along the LOS. As it is expected that this frequency shift varies rather slowly with time, it will contribute to a systematic error.

This rough estimate indicates that the impact of refraction is small. Nevertheless, if positional errors, the largest systematic DWE error source (see Sec. 5.6), can be reduced, it is worth quantifying this effect in more detail, especially near the ground. Near the surface, the refraction effect is maximum, because of the large molecular refractivity and the large PAA (γ_{des}).

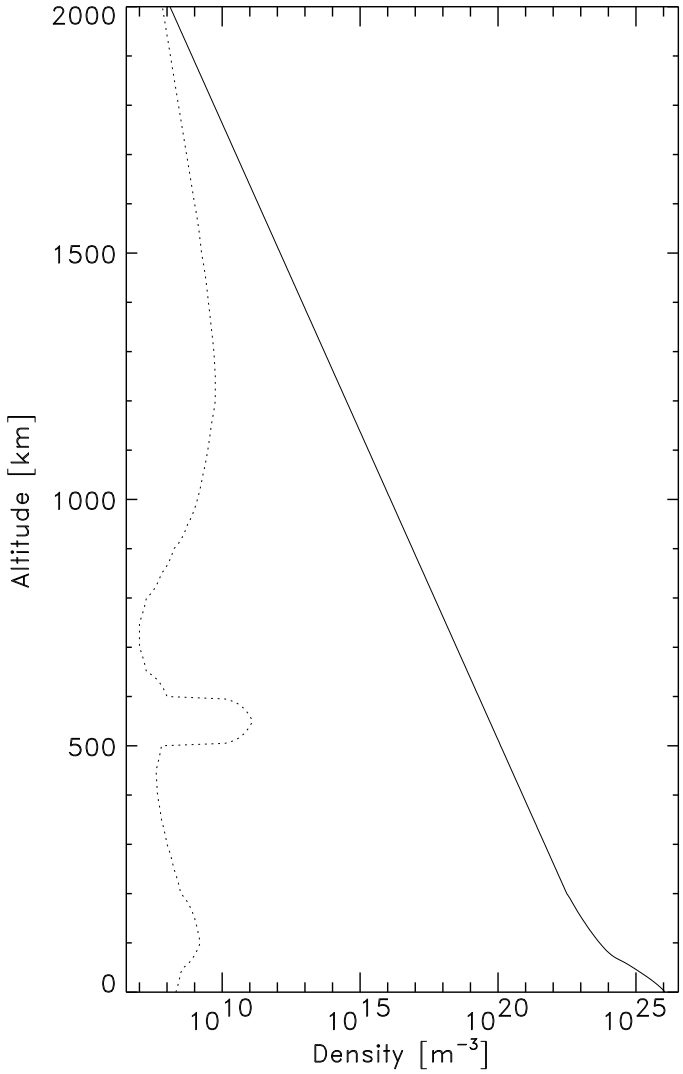

Figure 5.3: Molecular (solid line) and electron (dashed line) density in Titan's atmosphere. The molecular density is taken from the LH atmospheric model. The displayed electron density combines three models (see text).

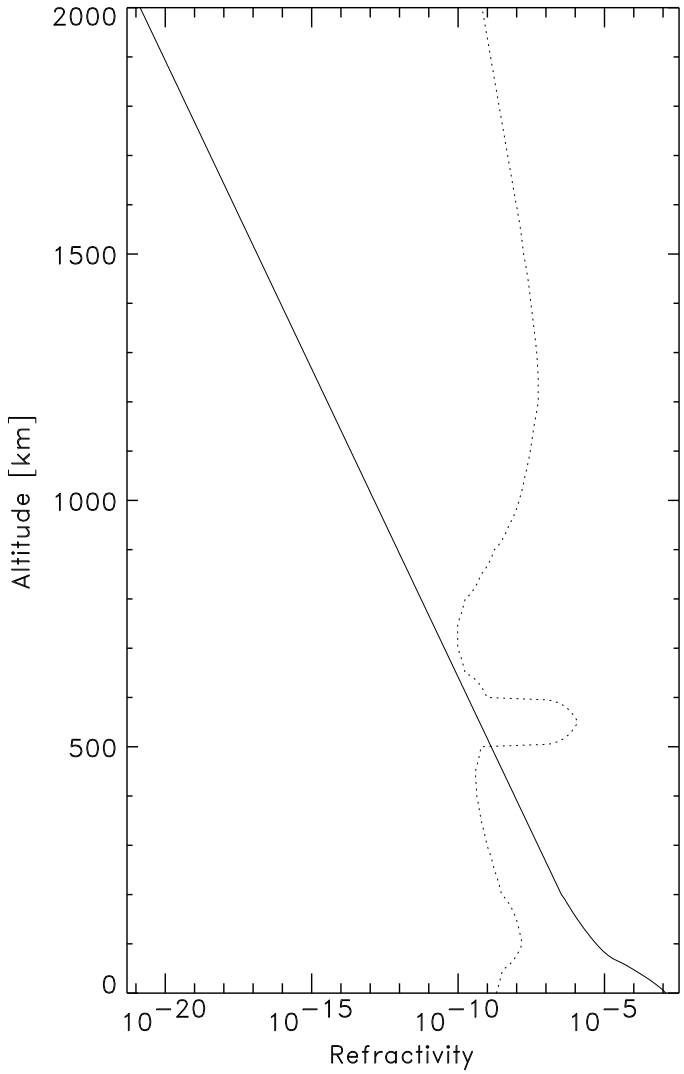

Figure 5.4: Molecular (solid line) and electron (dashed line) refractivity in Titan's atmosphere. The electron refractivity is generally negative. Thus, the dashed line shows the absolute value of the electron refractivity.

5.5.2 Gravitational Red-shift

It was shown in Section 5.1 that the transverse Doppler effect ($\alpha = 90°$) can be neglected. Another relativistic effect is the time dilatation in a gravitational field. According to general relativity, the frequency of a signal traveling from a distance r_1 from a gravitational center to a distance r_2 is shifted by

$$f_{D,grav} = f_0 \cdot \frac{GM}{c^2} \cdot (\frac{1}{r_1} - \frac{1}{r_2}) \tag{5.14}$$

where G is the Newton's gravitational constant and M is the mass of the gravitational center. In order to estimate the impact of this effect on the DWE, we have to consider the gravitational fields of both Saturn and Titan.

Cassini travels roughly 80,000 km during the Huygens descent. For the purpose of this estimate, we may assume that this motion is entirely radial with respect to Saturn. The mean orbital distance of Titan is r_T = 1,221,830 km. r_1 and r_2 can thus be set to r_T+40, 000 km and r_T−40, 000 km, respectively. With $M_{Saturn} = 5.68 \cdot 10^{26}$ kg, it follows from Eq. (5.14) that the gravitational field of Saturn shifts the frequency by less than 0.04 Hz during the Huygens mission, equivalent to 6 mm s^{-1} along the LOS.

The maximum range between Huygens and Cassini is 75,500 km at the beginning of the mission. At that time, the PAA (γ_{des}) is near 20°, so the radial difference between Cassini and Huygens with respect to Titan is about 70,000 km. We can thus set r_1 and r_2 to 2700 km and 72,700 km, respectively. With $M_{Titan} = 1.35 \cdot 10^{23}$ kg, the resulting frequency shift is less than 0.08 Hz, equivalent to 12 mm s^{-1} along the LOS.

In conclusion, the gravitational red-shift has a negligible impact on the DWE frequency measurement.

5.6 Geometrical Effects on the Doppler Shift

The speed along the line of sight between Cassini and Huygens v_{LS}, the parameter measured by DWE via Eq. (5.3), is given by

$$v_{LS} = (\vec{v}_{des} + \vec{v}_{NS} + \vec{v}_{EW} + \vec{v}_{rot} - \vec{v}_C) \cdot \vec{n}_{LS} \tag{5.15}$$

where $\vec{v}_{des}$ is the Huygens descent velocity, $\vec{v}_{NS}$ is its meridional velocity, $\vec{v}_{EW}$ is its zonal velocity, $\vec{v}_{rot}$ accounts for its velocity due to Titan's rotation, $\vec{v}_C$ represents the velocity of Cassini and $\vec{n}_{LS}$ is a unit vector pointing along the LOS from Cassini toward Huygens. Possible periodic velocity variations, e.g. due to spin or parachute swing, as well as refractive or other effects on the received frequency, are discussed separately.

In anticipation of the result of this chapter, Fig. 5.5 shows the typical contribution of all five velocities projected onto the LOS and converted to

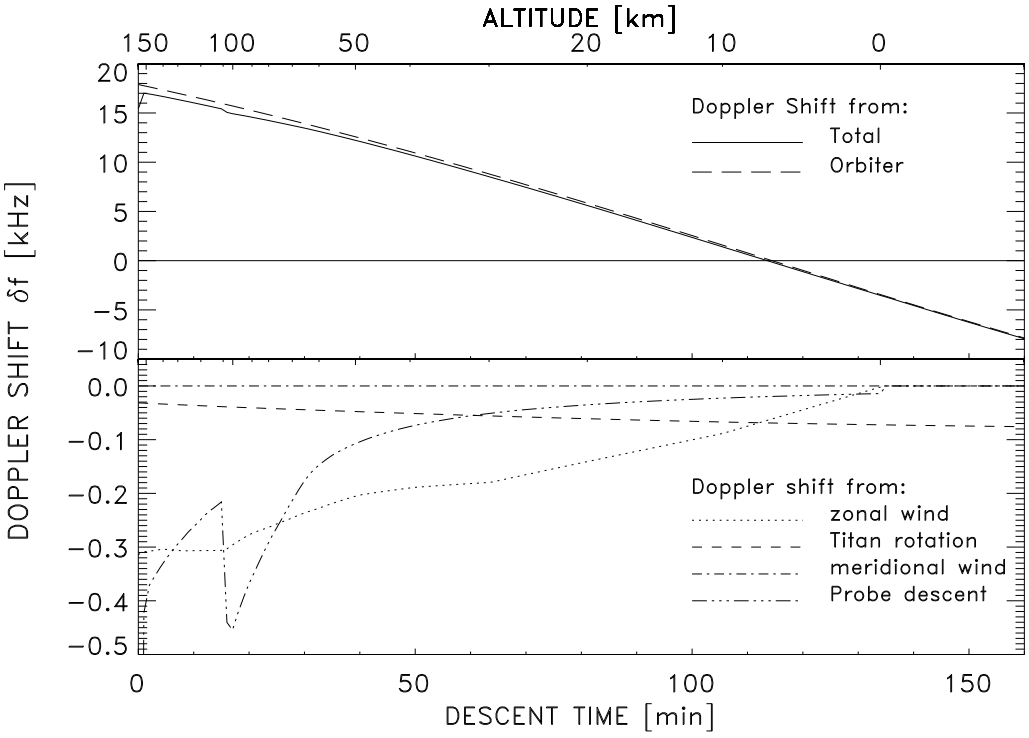

Figure 5.5: Contributions to PRL Doppler shift.

Doppler excess frequency f_D by Eq. (5.3). The exchange of parachutes at $t_0 + 15$ min is reflected in the shape of the contribution of the Huygens

descent velocity $\vec{v}_{des}$. The remaining Doppler contributions after touchdown at t_0+135 min are the Cassini velocity $\vec{v}_C$ and the Titan rotation velocity $\vec{v}_{rot}$. The value of $\vec{v}_{EW}$ is the desired quantity to be retrieved from this analysis. Neglecting the Probe response effect, this value represents the zonal wind speed. Rearranging Eq. (5.15) yields

$$v_{EW} = \frac{1}{\cos\gamma_{DWC}} \cdot (v_{LS} + v_C \cdot \cos\gamma_C - v_{des} \cdot \cos\gamma_{des} - v_{NS} \cdot \cos\gamma_{NS}) - v_{rot} \quad (5.16)$$

where $v = \mid \vec{v} \mid$ and the various angles are defined as:
γ_{DWC}: angle between the line of sight and the local east-west direction ("Doppler Wind Component Angle")
γ_C: angle between the line of sight and the Cassini velocity
γ_{des}: angle between the line of sight and the local vertical ("Probe Aspect Angle")
γ_{NS}: angle between the line of sight and the local north-south direction

Eq. (5.16) is used to retrieve the zonal wind speed. It contains nine parameters, only one of which is measured by DWE: the LOS velocity v_{LS}. The remaining parameters are other velocity contributions and geometry factors (angles), which depend on the relative positions of Cassini and Huygens. In the rotating IAU-Titan system, the Huygens velocity due to Titan's rotation v_{rot} is 0 and its impact is included in the Cassini velocity.

All parameters and possible other contributions are discussed in detail in the following subsections. JPL navigation predictions will be used for the construction for the trajectory of Cassini (see Appendix for details). The Huygens Probe vertical position and velocity are derived from altitude (Fig. 5.6) and descent velocity predictions (Fig. 5.7) provided by ESA. The horizontal components of the Huygens velocity are given by applying prograde and retrograde Flasar winds (Fig. 2.2) and a constant meridional wind (0 or $\pm$1 m s^{-1}). The position at the start of the descent phase, at t_0, is assumed to be 161.4°E and 9.0°S (all latitudes and longitudes are given in the IAU-Titan system). This differs slightly from the aim point in the B-plane (Section 3.2) to account for the Huygens motion during the entry phase. It must be noted, however, that accurate modeling of this motion is not yet accomplished. During the Huygens entry phase, this motion will be measured by HASI accelerometers. The state vectors of Cassini and Huygens are synchronized assuming that t_0 occurs at 09:11:10.8 UTC on 14 January 2005.

It becomes obvious from Eq. (5.16), that γ_{DWC}, the DWC angle, is a crucial parameter. In order to reduce the impact of inaccurate values for the

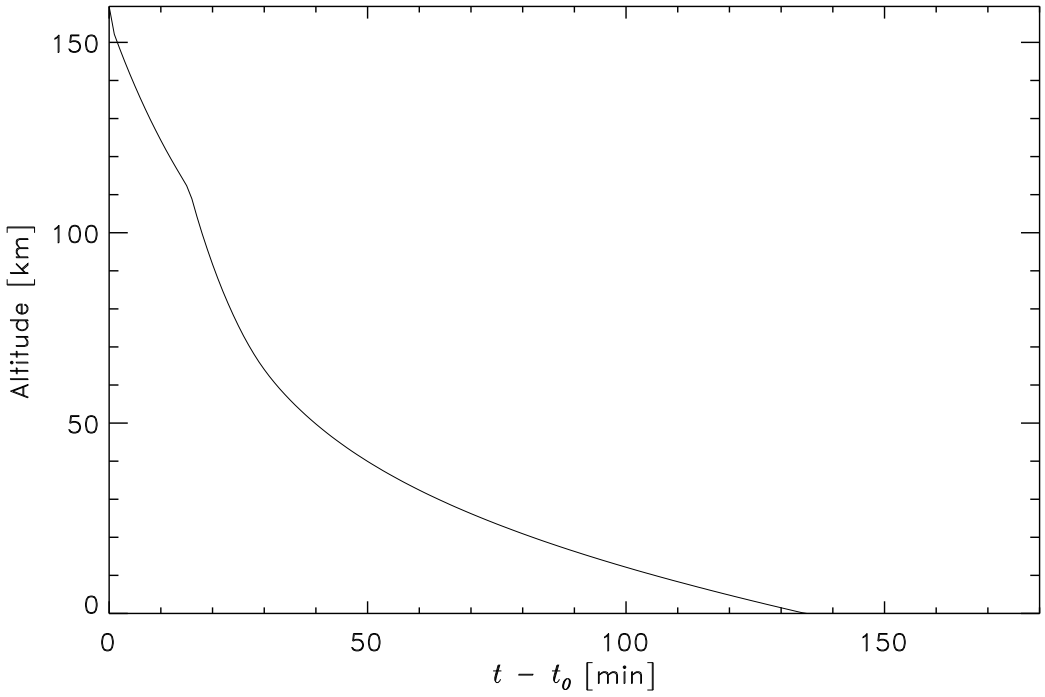

Figure 5.6: Huygens altitude during descent.

other velocity contributions, γ_{DWC} should avoid values near 90°. In fact, at $\gamma_{DWC} = 90°$, the zonal wind velocity becomes indeterminate.

The accuracy of the zonal wind speed δv_{EW} can be calculated by considering the accuracy of each of the nine parameters:

$$\begin{aligned} \delta v_{EW}^2 &= (\frac{\partial v_{EW}}{\partial v_{LS}}\delta v_{LS})^2 + (\frac{\partial v_{EW}}{\partial v_C}\delta v_C)^2 + (\frac{\partial v_{EW}}{\partial v_{des}}\delta v_{des})^2 \\ &+ (\frac{\partial v_{EW}}{\partial v_{NS}}\delta v_{NS})^2 + (\frac{\partial v_{EW}}{\partial v_{rot}}\delta v_{rot})^2 + (\frac{\partial v_{EW}}{\partial \gamma_{DWC}}\delta \gamma_{DWC})^2 \\ &+ (\frac{\partial v_{EW}}{\partial \gamma_C}\delta \gamma_C)^2 + (\frac{\partial v_{EW}}{\partial \gamma_{des}}\delta \gamma_{des})^2 + (\frac{\partial v_{EW}}{\partial \gamma_{NS}}\delta \gamma_{NS})^2 \end{aligned} \quad (5.17)$$

Here and in the following, the prefix δ denotes the accuracy of the corresponding variable. The (positive) square root of the summands will be called the "error contribution" and described as err(). For example, the error contribution due to the Huygens descent velocity is

$$\mathrm{err}(v_{des}) = \mid \frac{\partial v_{EW}}{\partial v_{des}}\delta v_{des} \mid$$

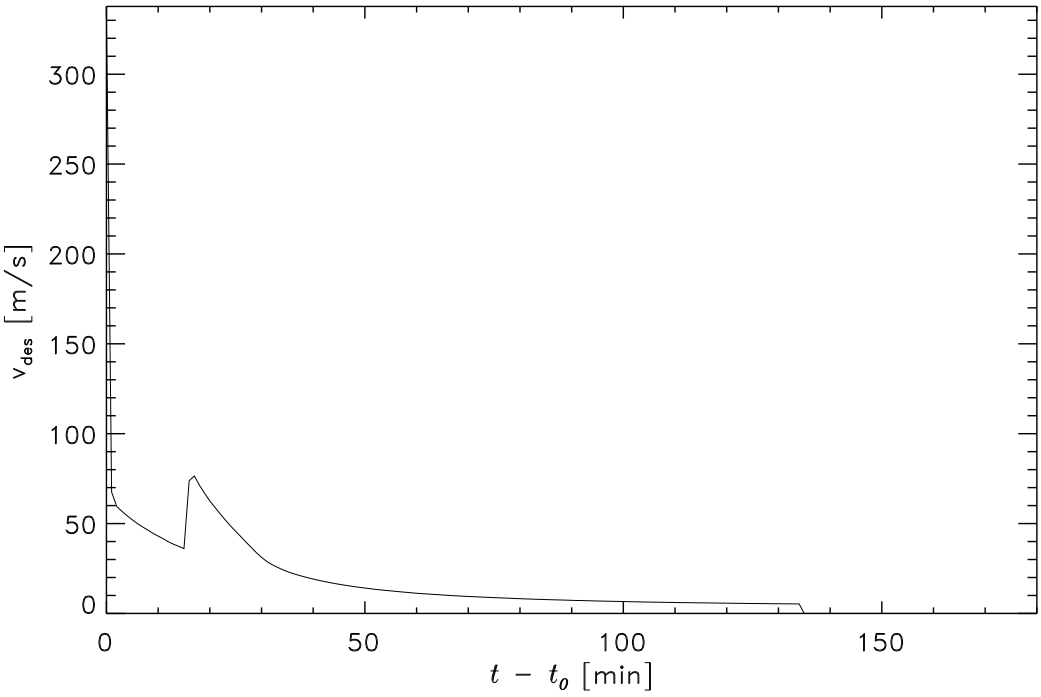

Figure 5.7: Huygens descent velocity.

The impact of the individual error contributions is discussed in the following subsections.

5.6.1 DWE Measurement: Range Rate

The LOS velocity between Huygens and Cassini v_{LS} calculated from Eq. (5.15), also called range rate, is shown in Fig. 5.8. The small crease at $t_0 + 15$ min

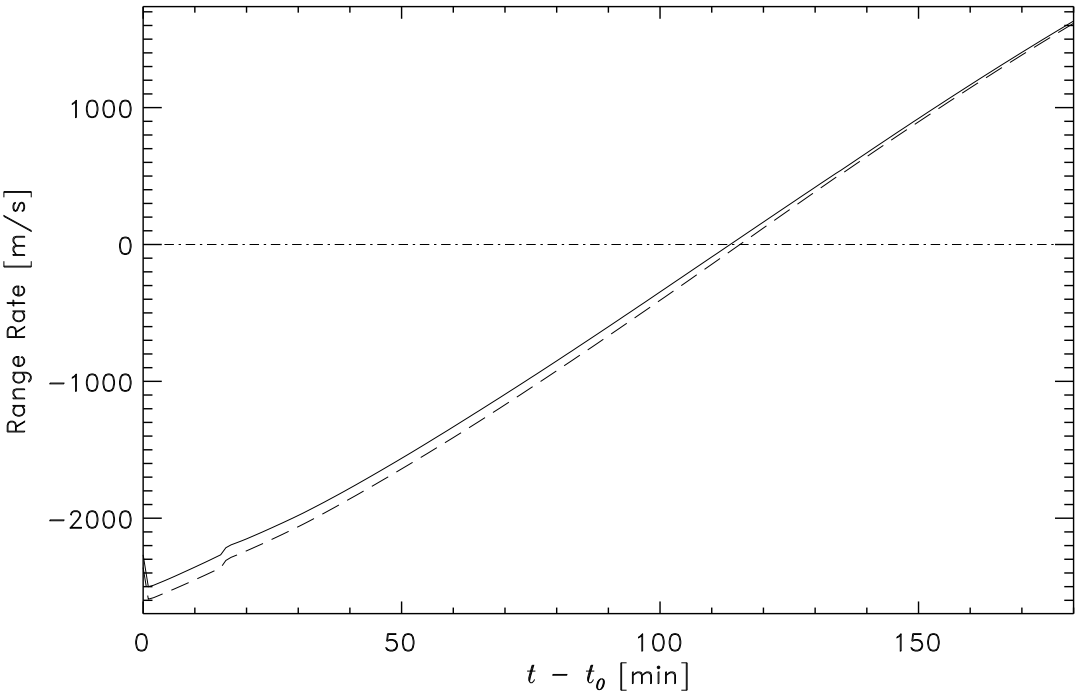

Figure 5.8: Range rate between Cassini and Huygens. The solid (long-dashed) line shows the range rate for prograde (retrograde) winds.

marks the exchange of parachutes. The zero-line crossing occurs near Cassini's Titan periapsis.

The range rate is the only parameter DWE is able to measure directly. The data for this analysis were simulated. JPL navigation predictions were used to model the Cassini velocity $\vec{v}_C$ with respect to the IAU-Titan system. The Huygens velocity $\vec{v}_H$ ($\vec{v}_H = \vec{v}_{des} + \vec{v}_{NS} + \vec{v}_{EW}$) was modeled using descent velocity (v_{des}) predictions provided by ESA (Figs. 5.7 and 5.9) and a vanishing meridional motion ($v_{NS} = 0$). The impact of nonvanishing meridional motions is investigated in Subsection 5.6.4. v_{EW} was modeled assuming that Huygens is carried by nominal prograde or retrograde Flasar winds. Fig. 5.10 shows this speed and its projection onto the LOS. With this speed, the ground track during the Huygens descent is about 7.5° or 340 km long (Fig. 5.11). The corresponding ranges, the distance between Cassini and Huygens, are

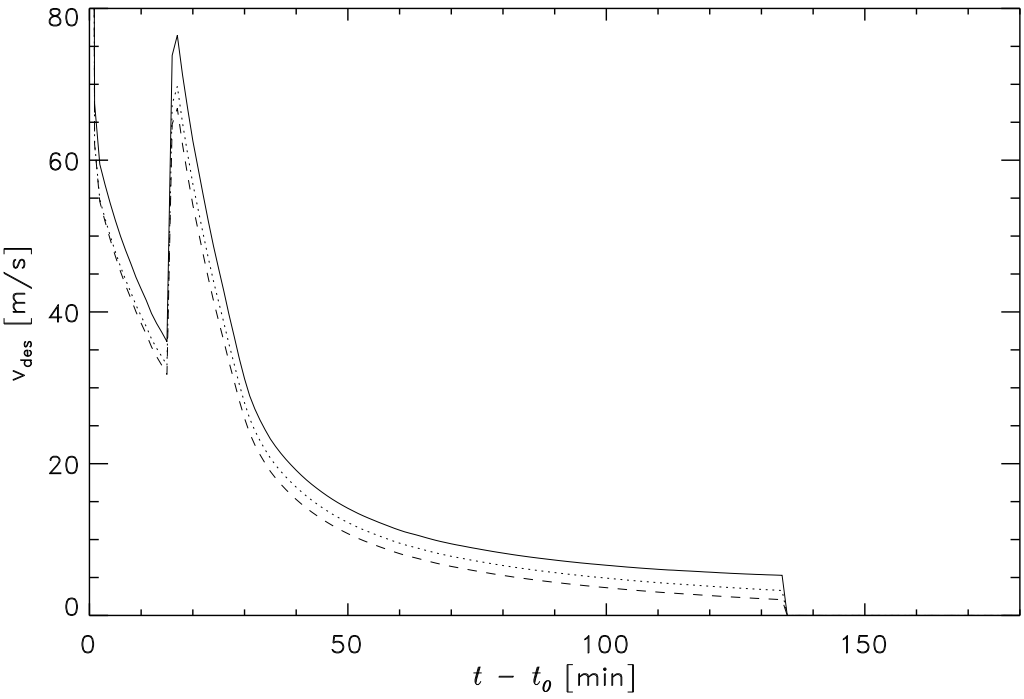

Figure 5.9: Huygens descent velocity v_{des}. The short-dashed line shows the projection onto the LOS ($v_{des} \cdot \cos\gamma_{des}$) for prograde winds, the dotted line for retrograde winds. v_{des} exceeds the maximum plot range during the first minute (see Fig. 5.7).

plotted in Fig. 5.12.

The first term in Eq. (5.17) represents the DWE measurement accuracy. With $v_{LS} = -f_D \cdot c/f_0$ (f_D: carrier Doppler excess, f_0: carrier frequency), it follows that

$$\delta v_{LS} = c \cdot \sqrt{(\frac{\delta f_D}{f_0})^2 + (\delta f_0 \frac{f_D}{f_0^2})^2} \tag{5.18}$$

The accuracy of the frequency measurement f_D is given by the DWE calibration. The result, as shown in Subsection 4.4.2, was $\delta f_D = 0.7$ Hz. The accuracy of the transmitter frequency $\delta f_0/f_0$ depends on the TUSO output accuracy, which was measured to be smaller than 10^{-8} (DASA, 1996). Using those numbers and inserting $f_0 = 2040$ MHz and $f_D \approx 10$ kHz as a typical value, one can easily calculate that the second term in Eq. (5.18), which is approximately eight orders of magnitude smaller than the first, can be

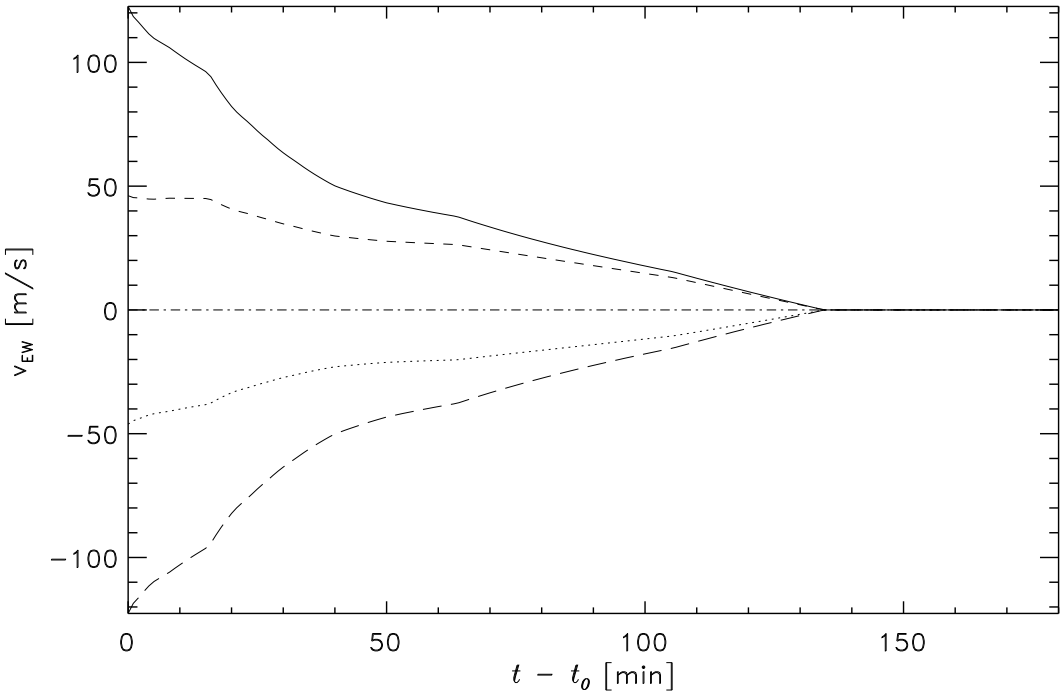

Figure 5.10: Huygens zonal velocity v_{EW}. The solid (long-dashed) line shows the prograde (retrograde) case. The short-dashed (dotted) line shows the projection onto the LOS ($v_{EW} \cdot \cos\gamma_{DWC}$) for prograde (retrograde) winds.

neglected. Thus, the DWE measurement accuracy is given by

$$\delta v_{LS} = c \cdot \frac{\delta f_D}{f_0} \tag{5.19}$$

This means that a possible offset δf_0 from 2040 MHz of the TUSO output frequency has virtually no impact on the accuracy of the zonal wind measurement. The relative offset *between* TUSO and RUSO remains as the only relevant parameter. Finally, with

$$\frac{\partial v_{EW}}{\partial v_{LS}} = \frac{1}{\cos\gamma_{DWC}} \tag{5.20}$$

it follows that the contribution of the DWE measurement error $\mathrm{err}(v_{LS})$ to the overall accuracy is

$$\mathrm{err}(v_{LS}) \;=\; \left| \frac{\partial v_{EW}}{\partial v_{LS}} \delta v_{LS} \right| \;=\; \left| \frac{c}{\cos\gamma_{DWC}} \cdot \frac{\delta f_D}{f_0} \right| \tag{5.21}$$

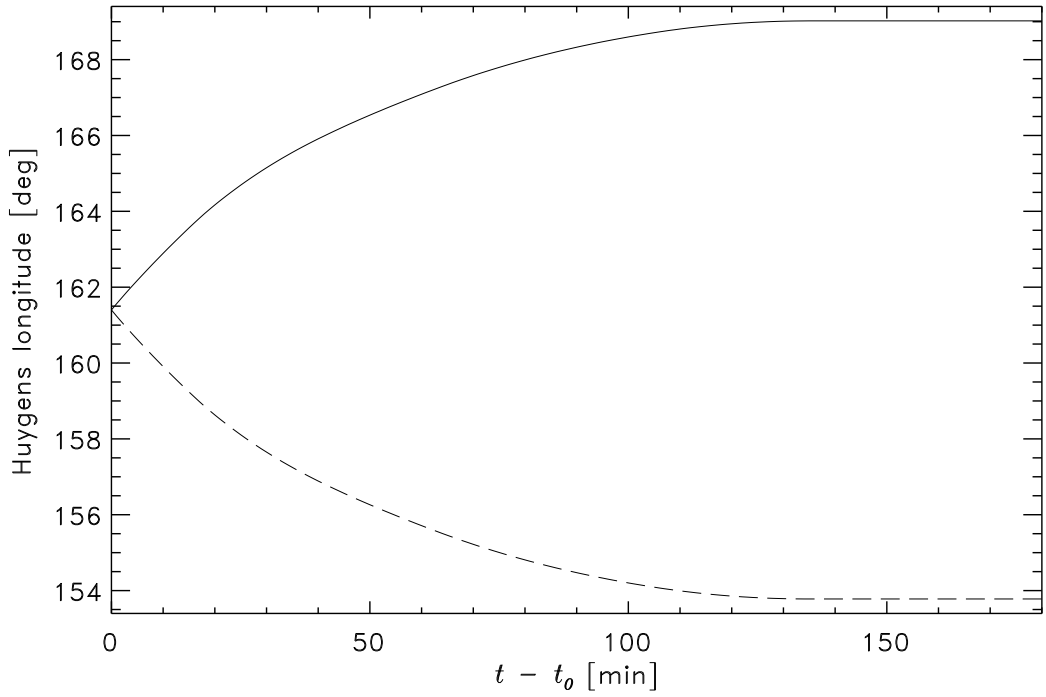

Figure 5.11: Huygens longitude. The solid line shows the prograde case; the long-dashed line the retrograde case.

Fig. 5.13 shows the evolution of this term during the Huygens mission for a prograde Flasar (solid line) and a retrograde (long-dashed line) wind profile. For this calculation, a conservative upper limit of $\delta f_D = 1$ Hz was used. The difference between the prograde and the retrograde case originates from the different evolution of the observation geometry (γ_{DWC}). In both cases, err(v_{LS}) decreases as the observation geometry improves ($\gamma_{DWC} \to 0$).

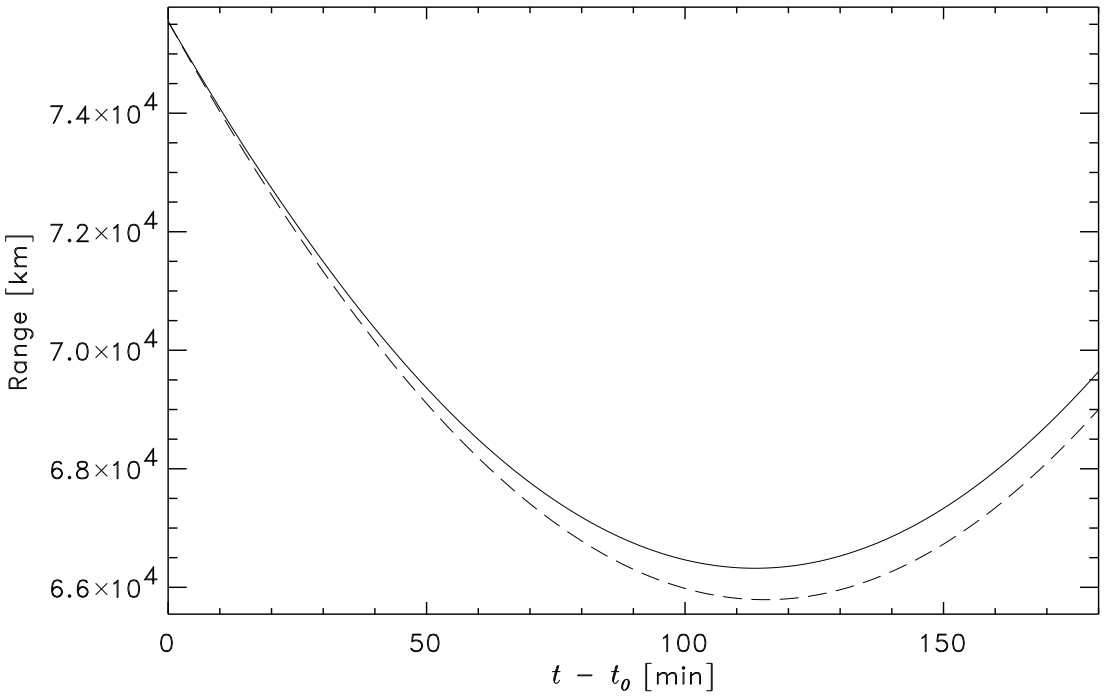

Figure 5.12: Range between Cassini and Huygens. The solid line shows the prograde case; the long-dashed line the retrograde case.

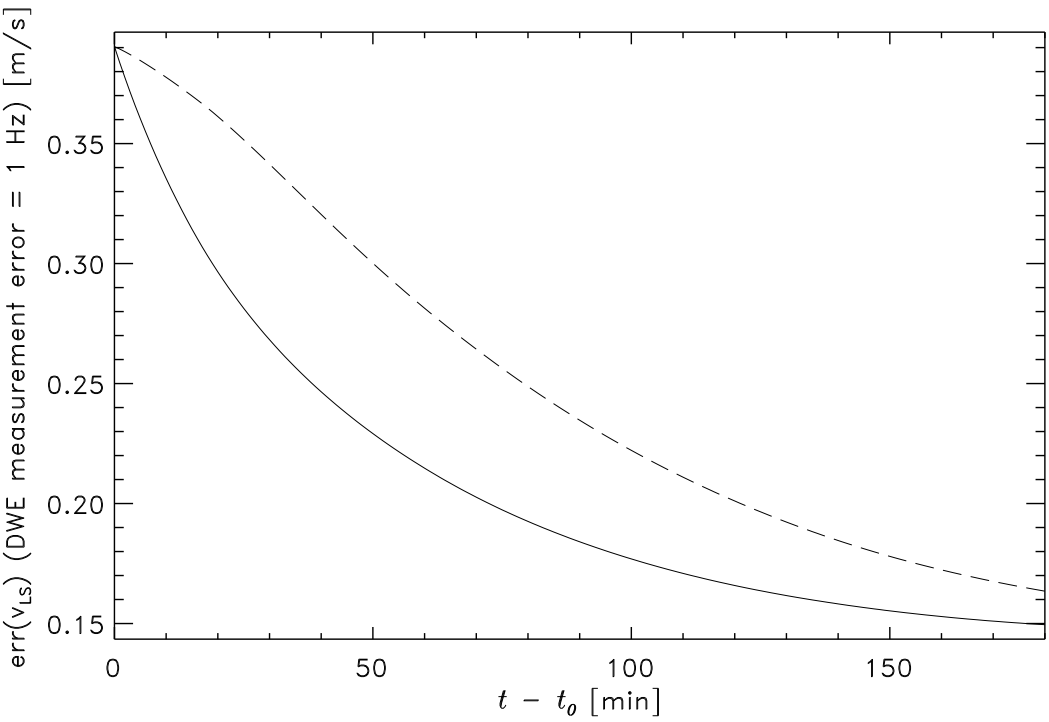

Figure 5.13: DWE measurement error for prograde winds. The solid line shows the prograde case; the long-dashed line the retrograde case.

5.6.2 Cassini Velocity

During most of the Huygens mission, the largest contribution to the Doppler excess stems from the Cassini velocity $\vec{v}_C$, which has an approximately constant absolute value of 5.7 km s^{-1} in a Titan centered frame throughout the Huygens descent. Fig. 5.14 shows the LOS projection of the Cassini velocity $v_{C,LOS} = v_C \cdot \cos\gamma_C$ for both prograde and retrograde zonal motion. Only

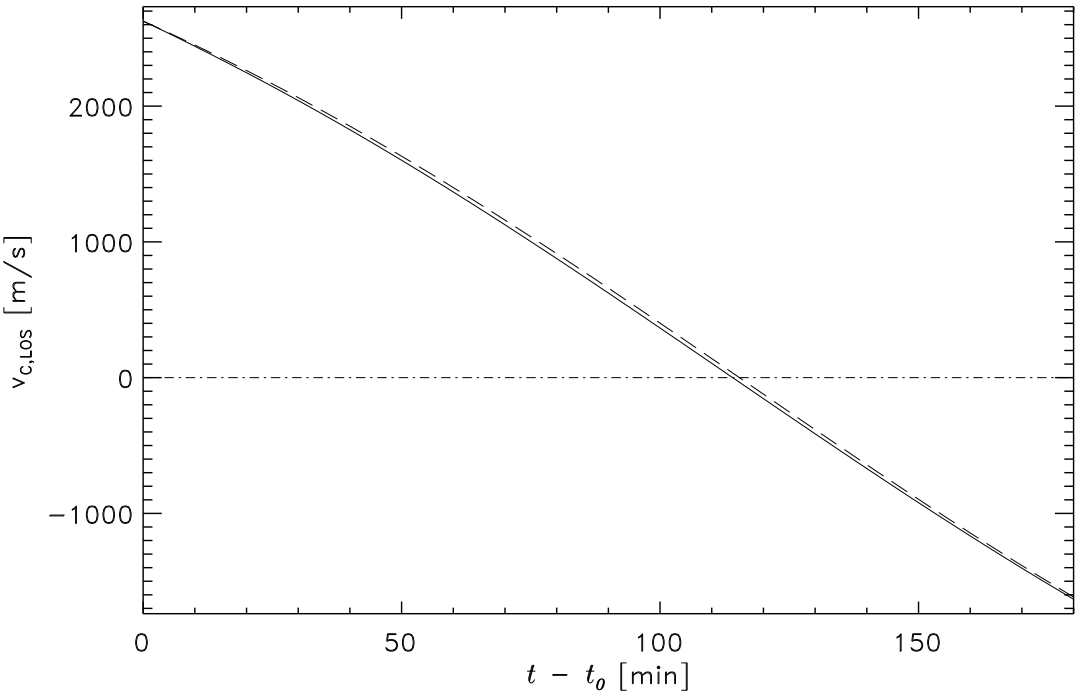

Figure 5.14: Cassini velocity projected onto the LOS. The solid line shows the prograde case; the dashed long-line the retrograde case.

near periapsis, about 115 minutes after the start of the descent phase, the radial component of this velocity vanishes and its contribution assumes 0.

As in the previous subsection, v_C was calculated using Cassini velocity predictions provided by JPL. The direction of the Cassini velocity and the locations of Cassini and Huygens are needed to model γ_C. The Huygens location was calculated iteratively by integrating the various Huygens velocity contributions. The evolution of γ_C and its accuracy is discussed in a separate chapter. For Fig. 5.14, we used the same Huygens velocity contributions as above while modeling the range rate v_{LS}.

The second term of Eq. (5.17), err(v_C), gives the impact on the accuracy of

the zonal wind retrieval resulting from inaccurate knowledge of v_C. Carrying out the differentiation gives

$$\mathrm{err}(v_C) \;=\; \left| \frac{\partial v_{EW}}{\partial v_C} \delta v_C \right| \;=\; \left| \frac{\cos\gamma_C}{\cos\gamma_{DWC}} \cdot \delta v_C \right| \qquad (5.22)$$

It is presently not clear, what accuracy can be achieved for the Cassini state vector (position and velocity) during the Huygens mission. A value $\delta v_C / v_C = 10^{-5}$ was used for this analysis, which is about two orders of magnitude greater than the accuracy achievable during the cruise to Saturn. The accuracy of the state vector is basically given by the integration time since the last trajectory alteration maneuver. It is currently planned to perform a last maneuver before the Huygens mission at about two weeks before. This is the Orbiter Deflection Maneuver (ODM) which prevents Cassini from following the Huygens trajectory and impacting on Titan. During cruise, the time between two maneuvers is generally longer. The variation of Eq. (5.22) during the mission is shown in Fig. 5.15.

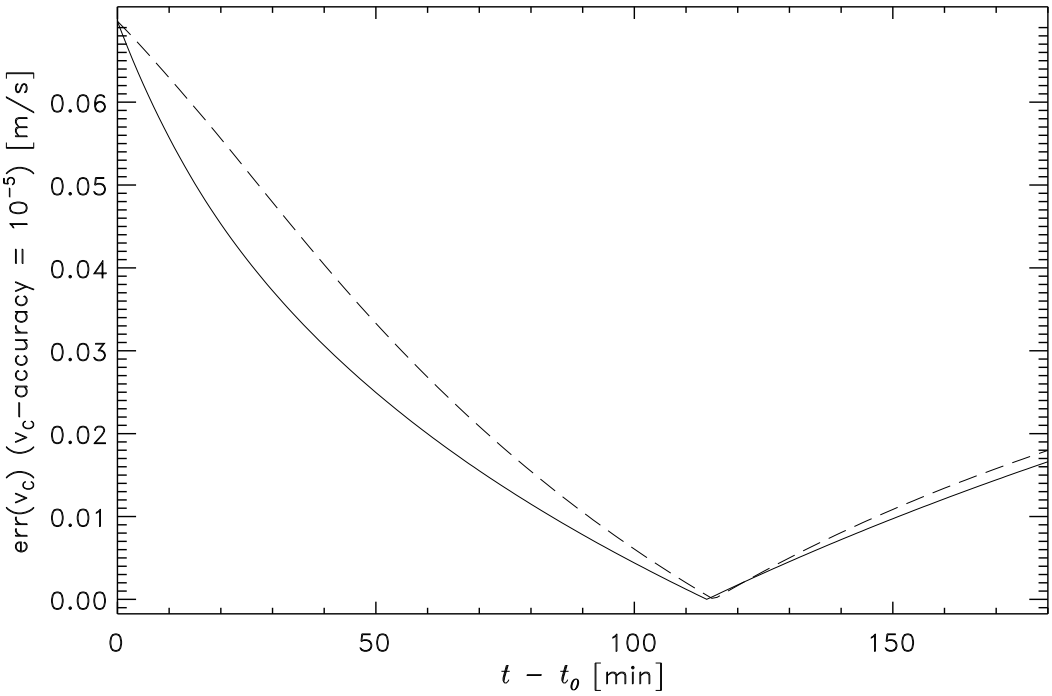

Figure 5.15: Error contribution from inaccurate Cassini velocity. The solid line shows the prograde case; the long-dashed line the retrograde case.

This analysis does not include effects from the HGA pointing update. In

contrast to the old mission scenario, where the observation geometry stayed approximately constant, the new mission geometry foresees a rather rapidly changing observation geometry. This requires updates of the HGA pointing direction. The pointing strategy and update rate, however, are not yet finalized. As will be shown later in the appropriate subsection, γ_C changes at a rate of about 0.004°/sec during the Huygens mission. Thus, within 10 minutes it changes by 2.4°, which equals the HGA-FWHM. Obviously, this is the maximum time which may pass between two successive pointing updates. The final update rate will probably be significantly greater.

After the Galileo experience, where the HGA refused to unfold after launch, it was decided to install a fixed-body HGA on Cassini. Thus, a pointing update requires reorientation of the entire spacecraft. It is clear that such attitude maneuvers could induce a small Doppler component in the received frequency. Their magnitude depends on the amplitude and slew rate of the pointing update maneuvers. If it is large enough to be visible in the frequency data, these events must be earmarked and the Doppler effects compensated.

5.6.3 Descent Velocity

The Huygens descent velocity v_{des} is an externally determined Huygens velocity component which DWE needs as input for the zonal wind retrieval. During the Huygens descent, this parameter will be measured by various sensors. For instance, DISR imaging will be used. More appropriate, however, are HASI measurements. The HASI accelerometer data can be integrated to retrieve the Huygens velocity. HASI will also perform pressure gradient measurements. Assuming hydrostatic equilibrium, this parameter is proportional to the descent velocity (Fulchignoni *et al.*, 1997). The accuracy of this measurement ($\sim$1%) can be increased by combining it with SSP speed of sound measurements (Atkinson, 1998). In the lower atmosphere, below 25 km, the altitude will also be determined by the radar altimeter unit (RAU). Although the RAU accuracy can be reduced to only 3% *a posteriori*, the resulting error is predominantly systematic and thus has no impact on the gradient, the descent velocity (Svedham, 2000). DISR imaging stops below 200 m altitude and the RAU saturates below 150 m. In this regime, the descent velocity may be determined from SSP sounder measurements (Atkinson, 1998). In summary, an accuracy for altitude and descent velocity of better than 1% seems to be achievable (Fulchignoni *et al.*, 1997).

Predictions for the Huygens altitude and descent velocity v_{des} have been provided by ESA and are shown in Fig. 5.6 and Fig. 5.7. The LOS projections of v_{des} for the prograde and retrograde cases ($v_{des} \cdot \cos\gamma_{des}$) are shown in Fig. 5.9. In case of retrograde winds, the LOS component is higher at the end of the mission, because γ_{des}, the Probe Aspect Angle (PAA), does not increase as much (see Subsection 5.6.7).

The error contribution from inaccurate descent velocity $\mathrm{err}(v_{des})$, given by

$$\mathrm{err}(v_{des}) \;=\; \left| \frac{\partial v_{EW}}{\partial v_{des}} \delta v_{des} \right| \;=\; \left| \frac{\cos\gamma_{des}}{\cos\gamma_{DWC}} \cdot \delta v_{des} \right| \qquad (5.23)$$

is displayed in Fig. 5.16. $\delta v_{des}/v_{des}$ was set to 1% for this calculation. Due to the slightly different evolution of γ_{DWC} and γ_{des} for the case of retrograde winds, a small difference is visible with respect to the prograde case.

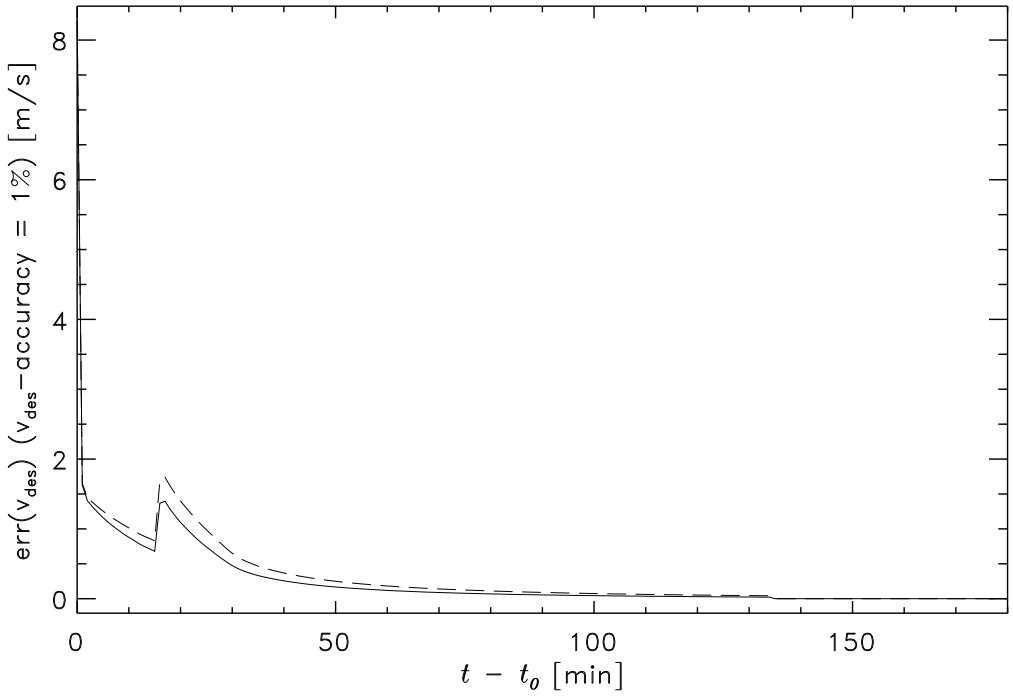

Figure 5.16: Error contribution from inaccurate Huygens descent velocity. The solid (long-dashed) line shows the prograde (retrograde) case.

5.6.4 Meridional Velocity

Most current wind models suggest that the Huygens meridional motion can be neglected in the region of interest below 200 km altitude. The model giving the highest meridional wind velocities (Tokano, 2000) predicts a maximum of 1 m s^{-1} in the upper stratosphere with no preferred direction. Other models yield significantly lower meridional wind speeds (see Section 2.2). It is clear that, if meridional motion is found during the Huygens descent by other means (e.g. DISR imaging), these findings will be incorporated into the zonal wind recovery algorithm.

In order to estimate the impact of an unknown meridional motion v_{NS} onto the zonal wind recovery, we calculated the contribution of a constant meridional wind of $v_{NS} = \pm 1$ m s^{-1}. Fig. 5.17 shows a southward wind of 1 m s^{-1} and its projection on the LOS ($v_{NS} \cdot \cos\gamma_{NS}$; dashed and dotted

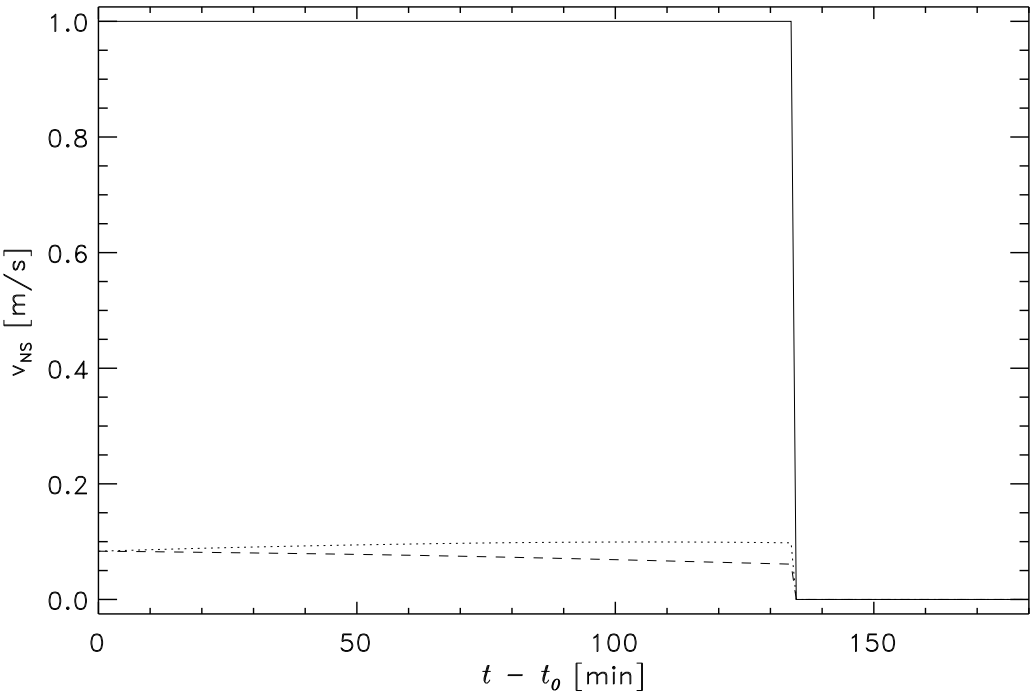

Figure 5.17: Huygens meridional velocity for a southward (positive) wind of 1 m s^{-1}. The short-dashed (dotted) line shows the meridional velocity projected on the LOS for prograde (retrograde) winds.

lines). In both the prograde and retrograde cases γ_{NS} is near 90° throughout the descent, as will be shown below. If such a wind were present during the

descent, Huygens would drift south a total of 0.18° or 8.1 km (Fig. 5.18).

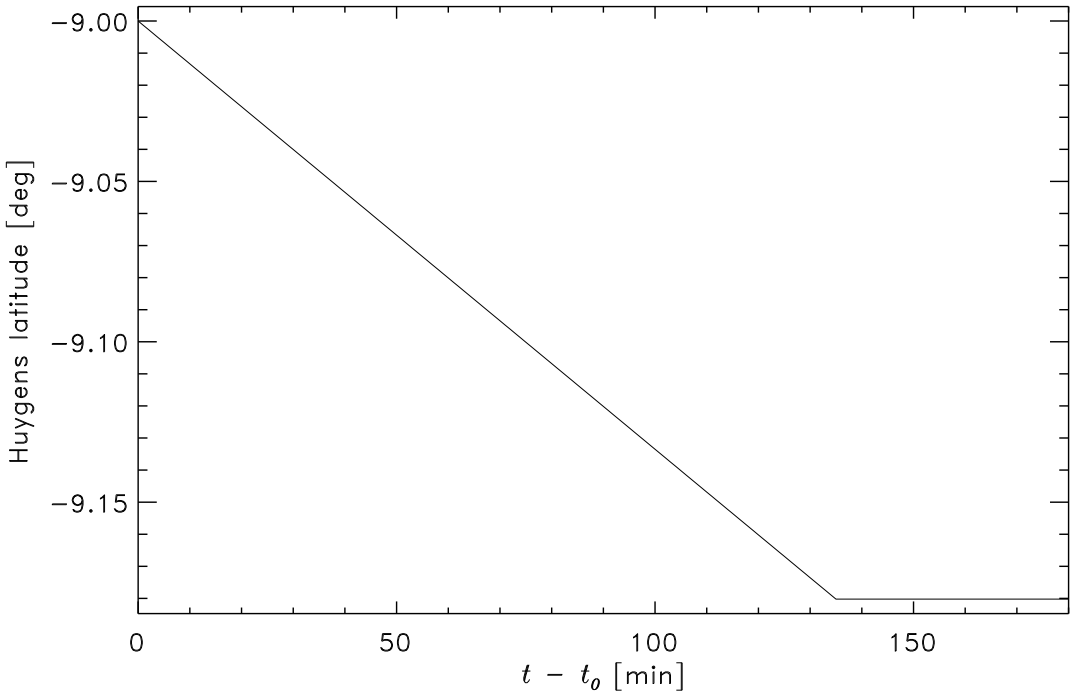

Figure 5.18: Huygens latitude for a southward (positive) wind of 1 m s^{-1}.

A similar result is obtained for a northward wind (v_{NS} = –1 m s^{-1}; Fig. 5.19). The corresponding Huygens latitude is plotted in Fig. 5.20.

The error contribution of this parameter err(v_{NS}) can be calculated from Eq. (5.17):

$$\mathrm{err}(v_{NS}) \;=\; \left| \frac{\partial v_{EW}}{\partial v_{NS}} \delta v_{NS} \right| \;=\; \left| \frac{\cos\gamma_{NS}}{\cos\gamma_{DWC}} \cdot \delta v_{NS} \right| \qquad (5.24)$$

Even assuming an error as large as δv_{NS} = 1 m s^{-1} keeps the contribution relatively small, as can be seen in Fig. 5.21. Again, this is because of the angle γ_{NS} being close to 90°.

Fig. 5.21 was produced assuming a vanishing meridional velocity (v_{NS} = 0 ± 1 m s^{-1}). Virtually identical plots are produced when v_{NS} is set to 1 ± 1 m s^{-1} and −1 ± 1 m s^{-1}.

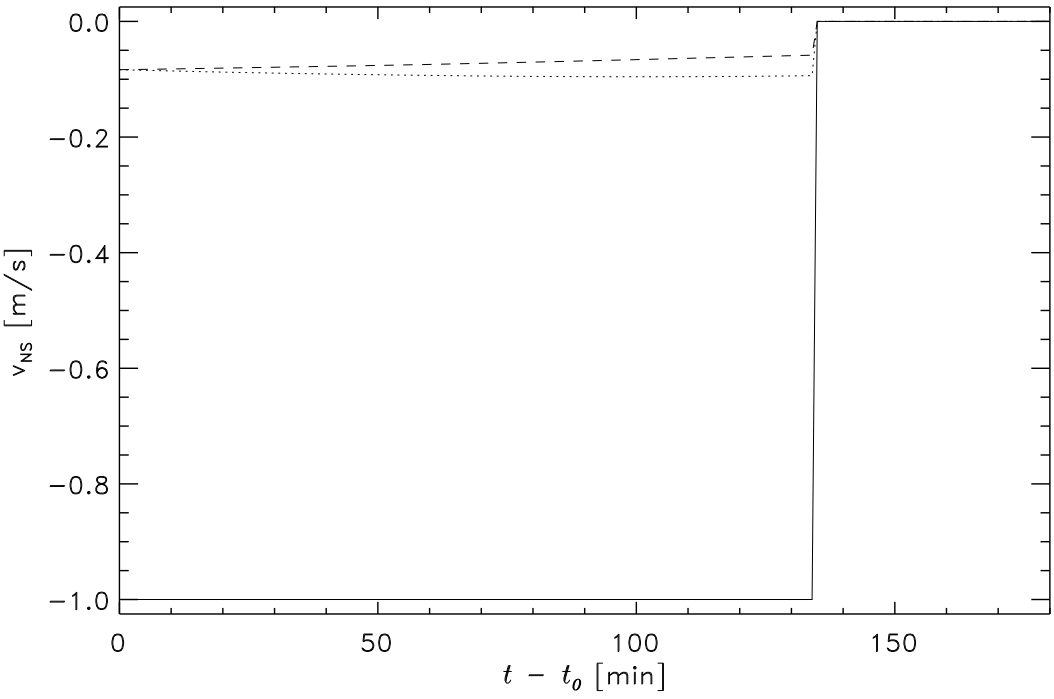

Figure 5.19: Huygens meridional velocity for a northward (negative) wind of –1 m s^{-1}. The short-dashed (dotted) line shows the meridional velocity projected on the LOS for prograde (retrograde) winds.

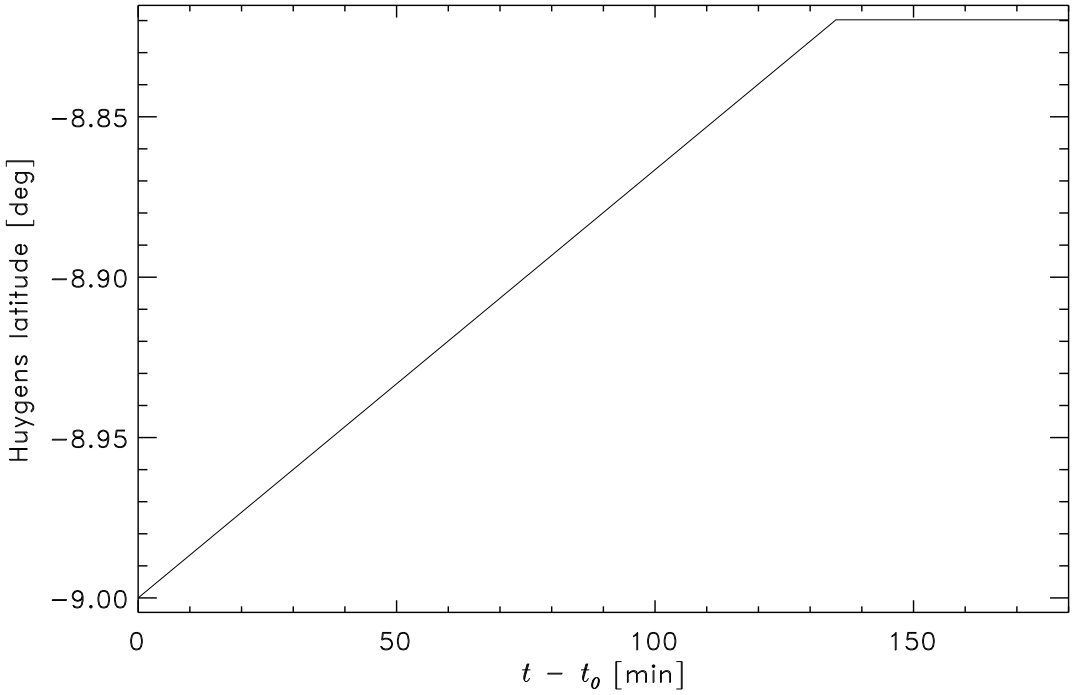

Figure 5.20: Huygens latitude for a northward (negative) wind of –1 m s^{-1}.

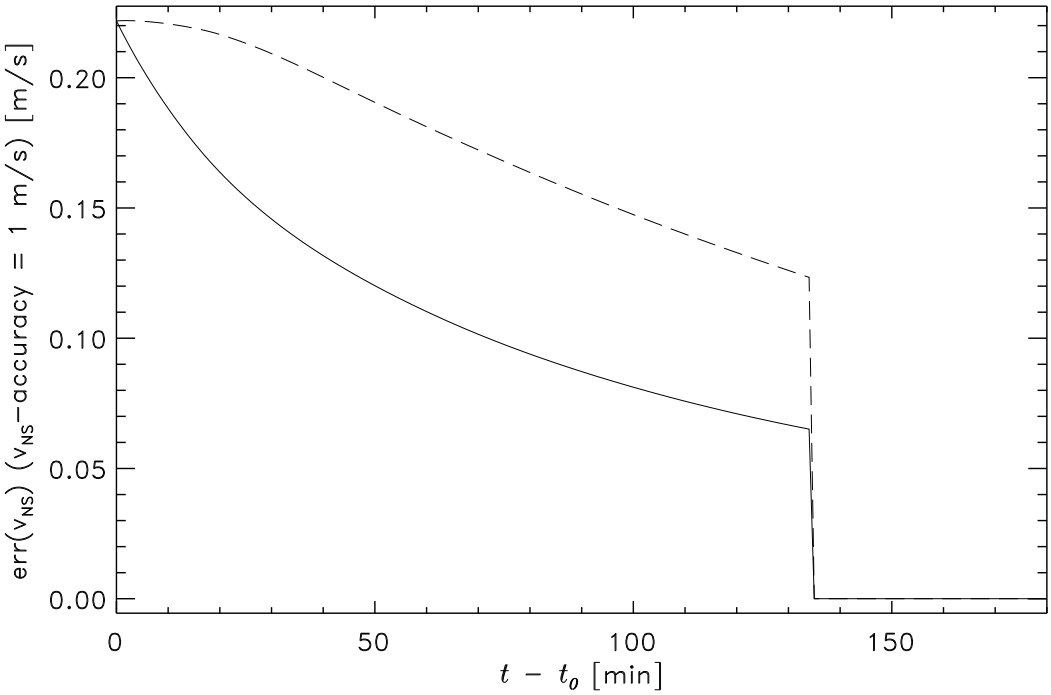

Figure 5.21: Error contribution from inaccurate Huygens meridional velocity. The solid (long-dashed) line shows the prograde (retrograde) case.

5.6.5 Titan Rotation

The rotation period of Titan could not be observed at the time of the Voyager 1 flyby because the surface was obscured by a featureless haze. However, the most probable rotation period from theoretical considerations would be synchronous to Titan's orbital period of 15.945452 days, as for most Saturn satellites. This assumption could be confirmed only recently.

Measurements of Titan's rotational light curve at IR wavelengths revealed a rotation period of 15.950 ± 0.025 days (Lemmon *et al.*, 1995). Combining this result with earlier measurements gave 15.949 ± 0.006 days. A recent reanalysis of Voyager 1 data stated a value of 15.946 ± 0.002 days as Titan's rotational period (Richardson *et al.*, 2001).

The local velocity of Huygens due to Titan's rotation is calculated from

$$v_{rot} = \frac{2\pi(R_T + z)}{T_{rot}} \cdot \cos(lat_H) \tag{5.25}$$

where R_T is Titan's radius, z is the Huygens altitude, T_{rot} is the rotation period and lat_H is the Huygens latitude. The surface velocity at the equator for synchronous rotation is 11.74 m s^{-1}. Fig. 5.22 shows the Huygens velocity resulting from Titan rotation and its projection onto the LOS ($v_{rot} \cdot \cos\gamma_{DWC}$). It must be noted that v_{rot} is 0 in the IAU-Titan coordinate system. The impact of Titan's rotation is included in the Cassini velocity v_C in this frame.

The error contribution of this parameter err(v_{rot}) is simply δv_{rot}, because $\vec{v}_{rot}$ and $\vec{v}_{EW}$ point in the same direction. The error of 0.002 days cited above contributes maximally only 1.5 mm s^{-1} and is thus clearly negligible.

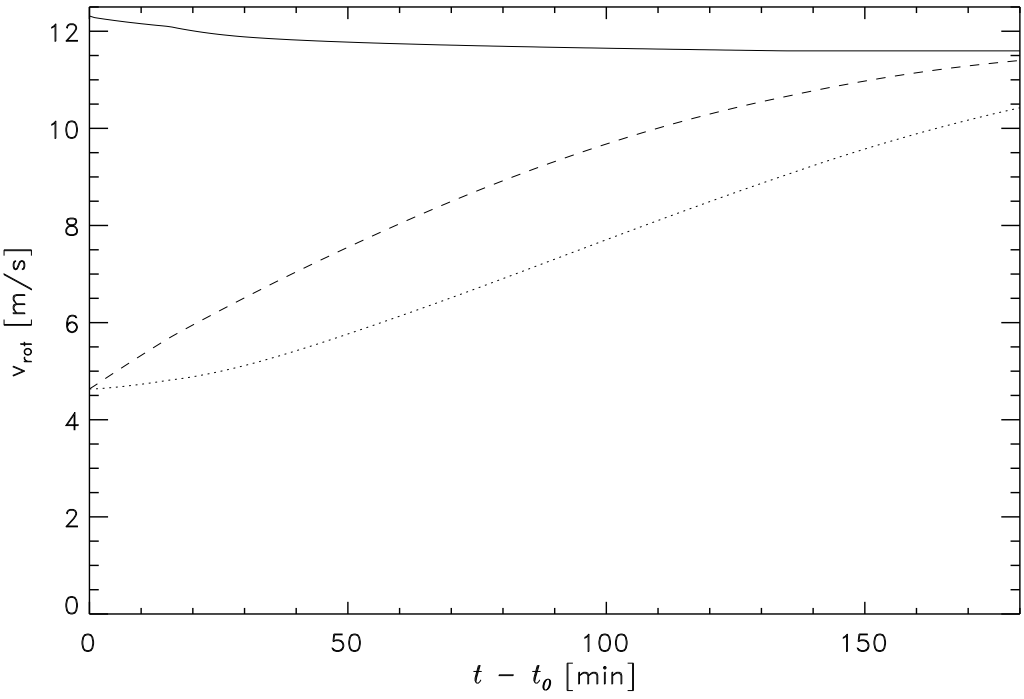

Figure 5.22: Huygens velocity due to Titan rotation. The short-dashed (dotted) line shows this velocity projected onto the LOS for the case of prograde (retrograde) winds.

5.6.6 Zonal Doppler Wind Component

The zonal Doppler wind component is defined as the cosine of the angle between the local east-west direction and the LOS ($\cos\gamma_{DWC}$). We define γ_{DWC}, the zonal Doppler wind component angle, as the angle between the vector pointing from Cassini to Huygens (the LOS vector) and a vector pointing towards east at the Huygens position. The evolution of this angle is displayed in Fig. 5.23 for prograde and retrograde winds, respectively.

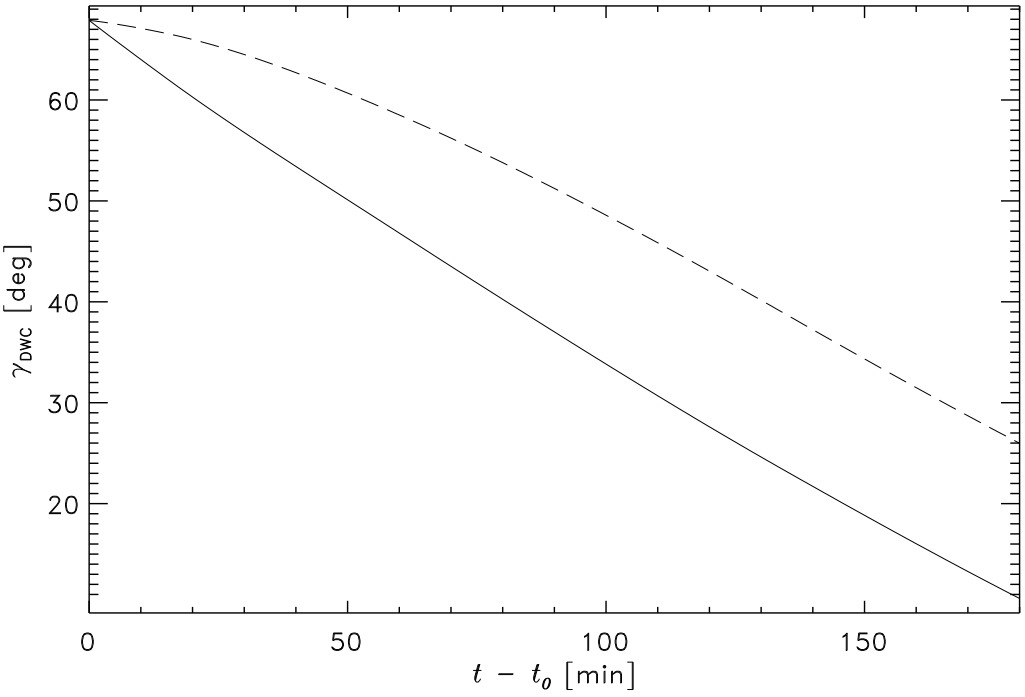

Figure 5.23: Evolution of Doppler wind component angle. The solid (long-dashed) line shows the prograde (retrograde) case.

The error contribution due to inaccurate knowledge of this parameter $\mathrm{err}(\gamma_{DWC})$ is given by

$$\mathrm{err}(\gamma_{DWC}) \;=\; \mid \frac{\partial v_{EW}}{\partial \gamma_{DWC}} \delta\gamma_{DWC} \mid \;=\; \mid \frac{\partial v_{EW}}{\partial(\cos\gamma_{DWC})} \delta(\cos\gamma_{DWC}) \mid \quad (5.26)$$

With $\delta(\cos\gamma_{DWC}) = -\sin\gamma_{DWC} \cdot \delta\gamma_{DWC}$, it follows that

$$\mathrm{err}(\gamma_{DWC}) \;=\; \mid (v_{EW} + v_{rot}) \cdot \tan\gamma_{DWC} \cdot \delta\gamma_{DWC} \mid \quad (5.27)$$

$\delta\gamma_{DWC}$ is constructed from the position errors of Cassini and Huygens. As all navigation errors are provided with respect to Titan, possible errors of the Titan ephemerides are already included in these errors. The Cassini trajectory can be reconstructed *a posteriori* to an accuracy of less than 10 km (Jones, 2000). For this analysis, we therefore assume a spherically symmetric error distribution around the nominal position of Cassini with a radius of $\delta x_C = 10$ km. At Cassini periapsis, this error contributes to a maximum of $\delta x_C / x_{LS} = 0.01°$ (x_{LS}: range between Cassini and Huygens; see Fig. 5.12).

The larger contribution to err(γ_{DWC}) stems from the position errors of Huygens. The Cassini latitude during the Huygens mission (Fig. 5.24) is ap-

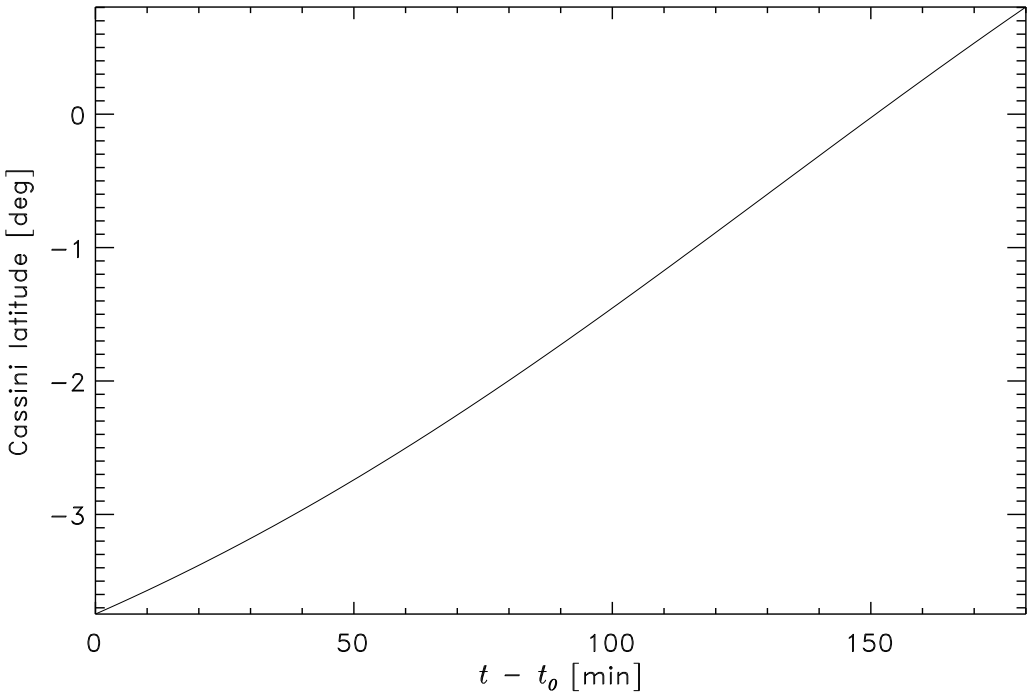

Figure 5.24: Cassini latitude during Huygens mission.

proximately equal to the Huygens latitude, which equals about −9°. As the LOS vector lies approximately in the plane which is spanned by the vectors v_{des} and v_{EW} (see also Fig. 3.3), this contribution may be approximated by the Huygens longitudinal position error δlon_H. Initially, this error is given by the longitudinal component of the Huygens delivery error ellipse, which has a 1-σ-width of 102 km corresponding to $\delta lon_{H,0} = 2.3°$ (see Fig. 3.1). However, like a sextant, DISR sun sensor measurements will effectively act

to circularize the error ellipse, thereby reducing it *a posteriori* to the more accurate latitudinal value of 12 km corresponding to $\delta lon_{H,0} = 0.26°$ (Atkinson, 1998).

An erroneous value for the initial longitude will induce a systematic error into the zonal wind recovery. It will be shown in this chapter that an erroneous initial longitude is in fact one of the most dominant error sources. At this point, we have to anticipate the results of the simulation presented in Chapter 6. The simulation shows that the error on the recovered zonal wind speed induced by the erroneous initial longitude decreases the longitudinal offset. This can be explained as follows: If the true Huygens longitude is east of the longitude assumed by the zonal wind retrieval program, the Cassini observation angle γ_C used by the retrieval program is generally smaller than the true γ_C (see Fig. 3.2). The term $v_C \cdot \cos\gamma_C$ in Eq. (5.16) is therefore underestimated. Furthermore, in this case the DWC angle γ_{DWC} used by the retrieval program is generally larger than the true DWC angle. In the case of prograde winds, both effects act to overestimate the zonal wind speed. If the winds are retrograde, the effects have opposite directions, but due to the large value of $v_C \cdot \cos\gamma_C$, the effect of the underestimation of γ_C dominates. The opposite is true if the true initial Huygens longitude is west of the longitude used by the retrieval program. In summary, the retrieved zonal wind velocity always acts to decrease a possible initial longitudinal position error. Just like in a feedback loop, any initial longitudinal position error converges towards 0 in the course of the zonal wind retrieval. After each step of this recovery algorithm, the new Huygens longitude is determined from the recovered zonal wind speed, and the new Huygens longitude is always slightly closer to the true Huygens longitude than the longitude recovered in the previous step. This is an important result, because it makes the zonal wind retrieval algorithm very robust.

$\delta\gamma_{DWC}$ may thus be written as the RSS of the angular uncertainty in the positions of Cassini and Huygens, respectively:

$$\delta\gamma_{DWC} = \sqrt{(\frac{\delta x_C}{x_{LOS}})^2 + \delta lon_H^2} \approx \delta lon_H \tag{5.28}$$

Following the argumentation above, δlon_H decreases during the mission. However, for the purpose of this error estimation, we keep it constant at its initial value.

Fig. 5.11 shows the Huygens longitude lon_H for prograde and retrograde winds. The contribution of the error $\delta\gamma_{DWC} \approx \delta lon_H$ to the zonal wind recovery error $\mathrm{err}(\gamma_{DWC})$ is displayed in Fig. 5.25. Even though δlon_H is kept constant, the contribution of this error decreases due to the improving observation geometry. It should be kept in mind that δlon_H actually decreases

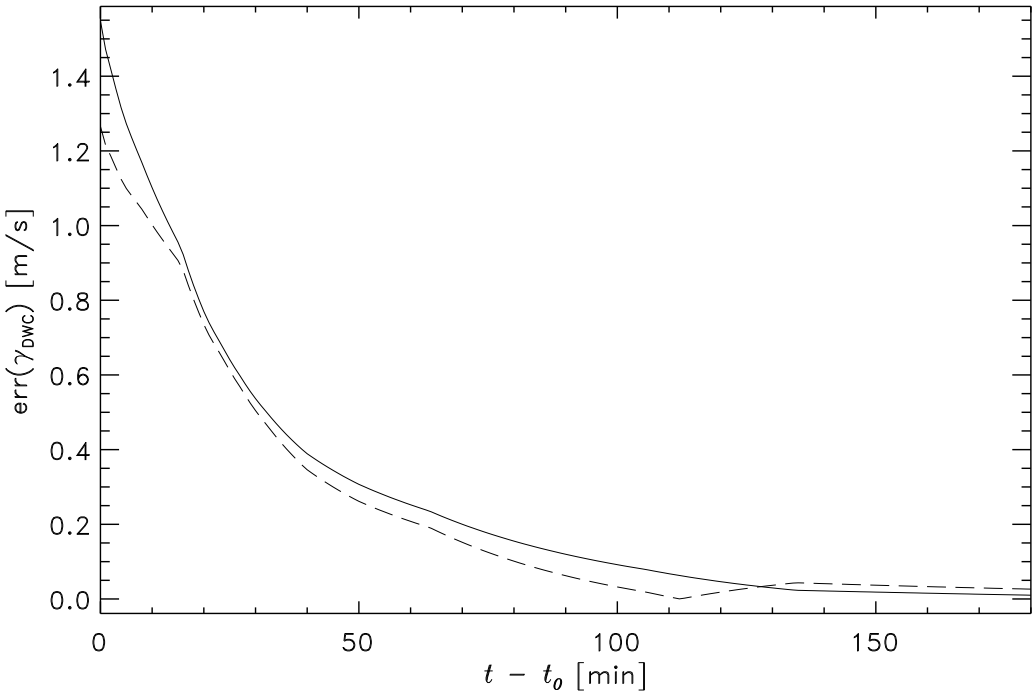

Figure 5.25: Error contribution from inaccurate Doppler wind component angle. The solid (long-dashed) line shows the prograde (retrograde) case.

during the mission, so the error contribution plotted in Fig. 5.25 is slightly overestimated for $t \to t_0 + 180$ min.

5.6.7 Probe Aspect Angle

This angle (γ_{des}) is defined as the angle between the local vertical and the LOS. γ_{des} is often called the "Probe Aspect Angle" (PAA). Strictly speaking, the PAA is the angle between the Huygens vertical axis and the LOS. If Huygens is tilted away from the local vertical, the PAA and γ_{des} differ by the tilt angle. However, in this analysis, we use γ_{des} and PAA synonymously. Fig. 5.26 shows the behavior of this angle during the Huygens mission for

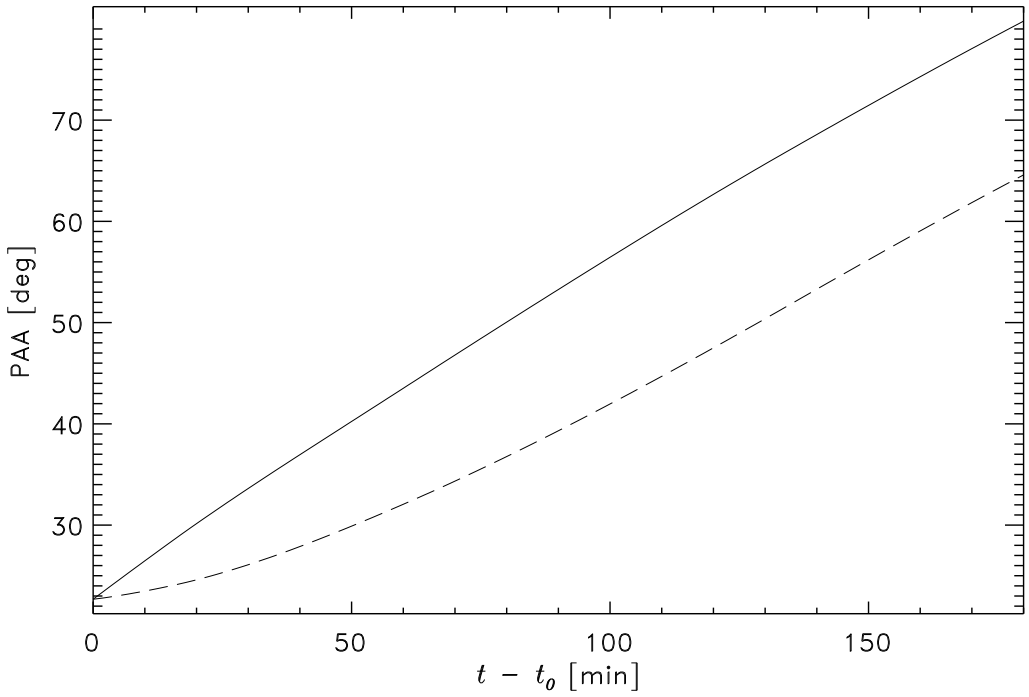

Figure 5.26: Evolution of the angle between the local vertical and the LOS. The solid (long-dashed) line shows the prograde (retrograde) case.

prograde and retrograde winds.

Following the same approach as for γ_{DWC}, its error contribution is given by

$$\mathrm{err}(\gamma_{des}) \;=\; \left| \frac{\partial v_{EW}}{\partial \gamma_{des}} \delta\gamma_{des} \right| \;=\; \left| \frac{v_{des}}{\cos\gamma_{DWC}} \cdot \sin\gamma_{des} \cdot \delta\gamma_{des} \right| \qquad (5.29)$$

As noted in the previous subsection, the LOS vector lies approximately in the plane spanned by the vectors $\vec{v}_{des}$ and $\vec{v}_{EW}$. This implies that $\delta\gamma_{des} = \delta\gamma_{DWC}$, where $\delta\gamma_{DWC}$ is defined by Eq. (5.28).

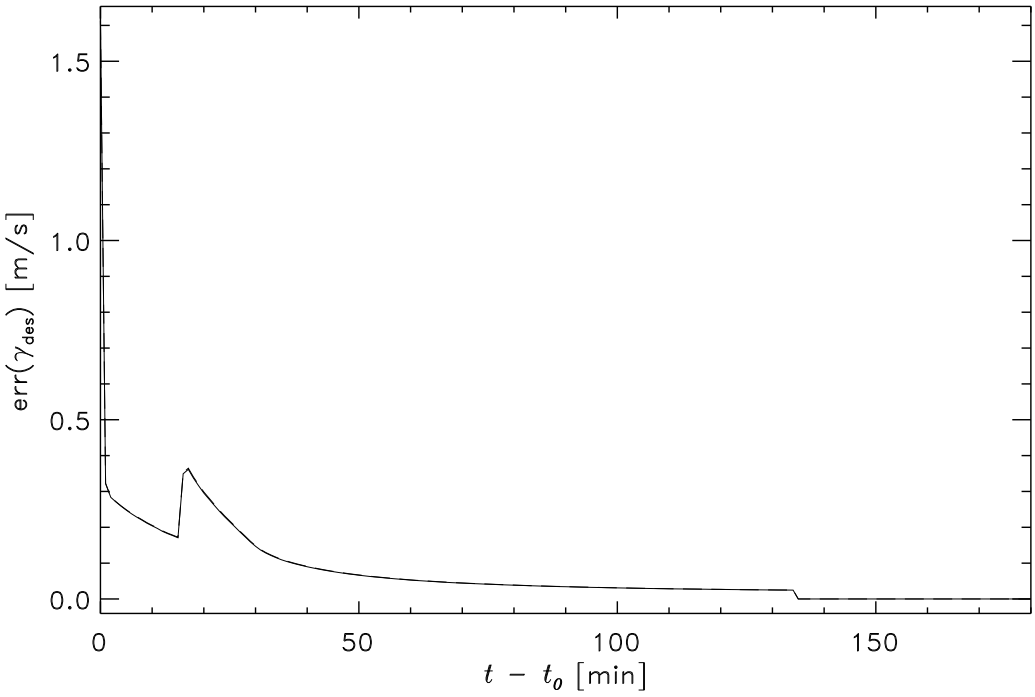

Figure 5.27: Error contribution from $\delta\gamma_{des}$. The solid (long-dashed) line shows the prograde (retrograde) case. No difference is visible between the prograde and the retrograde case.

The resulting error contribution from γ_{des} is displayed in Fig. 5.27. The prograde and retrograde error contributions $\mathrm{err}(\gamma_{des})$ differ only marginally. As $\gamma_{des} \approx 90° - \gamma_{DWC}$, Equation 5.29 may be simplified to

$$\mathrm{err}(\gamma_{des}) \approx v_{des}\delta\gamma_{des} \tag{5.30}$$

This result accounts for the almost identical error contributions in both prograde and retrograde case. As in the previous subsection, $\mathrm{err}(\gamma_{des})$ is slightly overestimated towards the end of the mission, due to the use of a constant longitudinal position error.

5.6.8 Meridional Doppler Wind Component

As can be seen from Fig. 3.3, this angle (γ_{NS}) is near 90° throughout the Huygens mission. The exact evolution is displayed in Fig. 5.28. The differ-

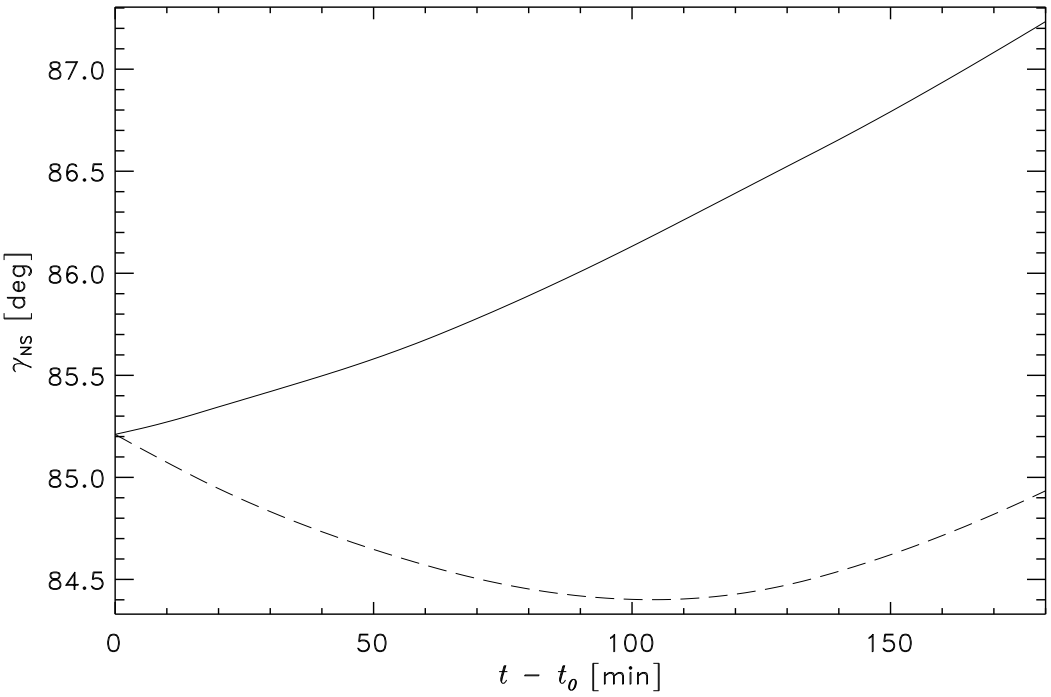

Figure 5.28: Evolution of the angle between the local north-south direction and the LOS. The solid (long-dashed) line shows the prograde (retrograde) case.

ence between the prograde and the retrograde case originates from the fact that in the retrograde case the longitudinal velocity of Huygens is initially faster than that of Cassini until about $t_0 + 100$ min and that the projection of the latitudinal offset between Huygens and Cassini is a function of $\cos(lon_C - lon_H)$ (Figs. 5.11 and 5.29). With such a large value for γ_{NS} it is clear from Eq. (5.16) that even large meridional motions (which are not expected) have negligible impact on the zonal wind recovery, as desired by DWE.

The error contribution from inaccurate value of this angle can be written

$$\mathrm{err}(\gamma_{NS}) = \left| \frac{\partial v_{EW}}{\partial \gamma_{NS}} \delta\gamma_{NS} \right| = \left| \frac{v_{NS}}{\cos\gamma_{DWC}} \sin\gamma_{NS} \delta\gamma_{NS} \right| \qquad (5.31)$$

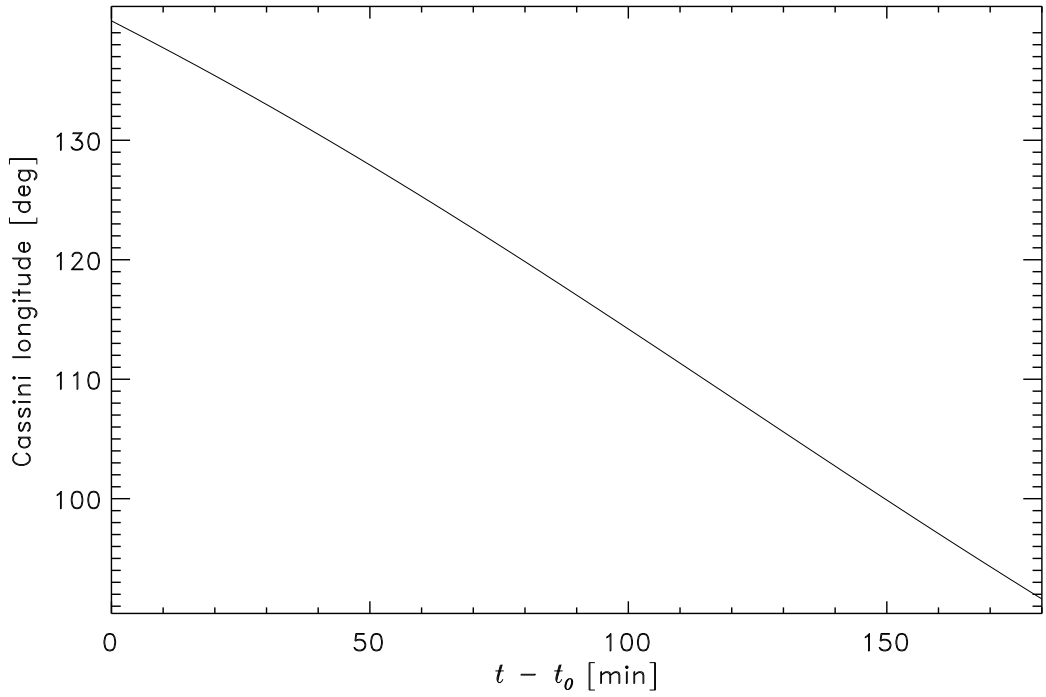

Figure 5.29: Cassini longitude during Huygens mission.

Similar to the derivation of $\delta\gamma_{DWC}$ and $\delta\gamma_{des}$, $\delta\gamma_{NS}$ is constructed from the position errors of Huygens and Cassini. The Cassini contribution is again small ($\delta x_C / x_{LS}$). The Huygens contribution may be approximated by the latitudinal position error δlat_H multiplied by the cosine of the longitudinal offset between Huygens and Cassini. When this offset is 0°, $\delta\gamma_{NS}$ is equal to δlat_H. On the other hand, when it is 90°, a variation of the Huygens latitude has no impact on the value of γ_{NS}. Thus, $\delta\gamma_{NS}$ can be written

$$\delta\gamma_{NS} = \sqrt{(\frac{\delta x_C}{x_{LOS}})^2 + [\delta lat_H \cdot \cos(lon_C - lon_H)]^2} \qquad (5.32)$$

Eq. (5.32) resembles Eq. (5.28). However, in Eq. (5.28) we neglected the corresponding factor $\cos(lat_C - lat_H)$, because the latitudes of Huygens and Cassini are approximately equal throughout the mission.

The value of δlat_H is given by the initial latitudinal delivery error $\delta lat_{H,0}$, which is 0.26° (see Subsection 5.6.6). For this error estimation, we assume that a nonvanishing meridional velocity leads to an increase of this value. This is identical to the assumption that the systematic error induced by an erroneous initial latitudinal position diverge, in contrast to the converging

longitudinal position error, and is therefore an upper boundary for δlat_H. After the ith sample, δlat_H is given by

$$\delta lat_{H,i} = \delta lat_{H,0} + \frac{dt}{R_T} \cdot \sum_{j=0}^{i} \delta v_{NS,j} \tag{5.33}$$

Fig. 5.30 shows the increase of δlat_H assuming a constant meridional wind of 1 m s^{-1}, either north- or southward. The resulting error $\delta\gamma_{NS}$ is displayed in

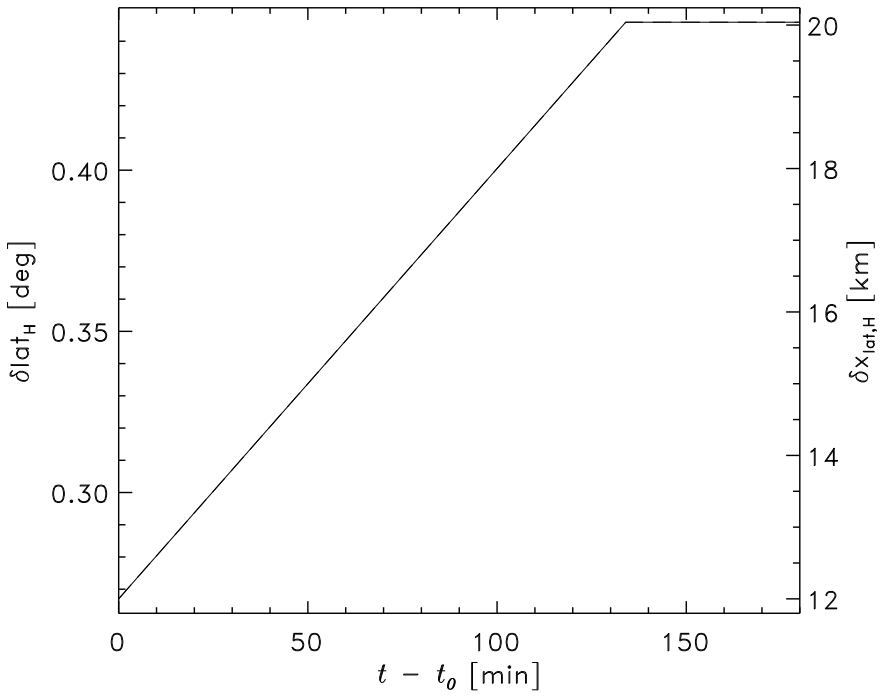

Figure 5.30: Huygens latitudinal position error for a constant meridional wind speed of ± 1 m s^{-1}.

Fig. 5.31. It is clear that, if meridional motion can be neglected ($v_{NS} = 0$), the error contribution err(γ_{NS}) vanishes. Even with setting $v_{NS} = 1$ m s^{-1} (southward), the error contribution is around 1 cm s^{-1} or less. This case is displayed in Fig. 5.32. As the error contributions are positive definite, setting $v_{NS} = -1$ m s^{-1} (northward) gives a virtually identical result.

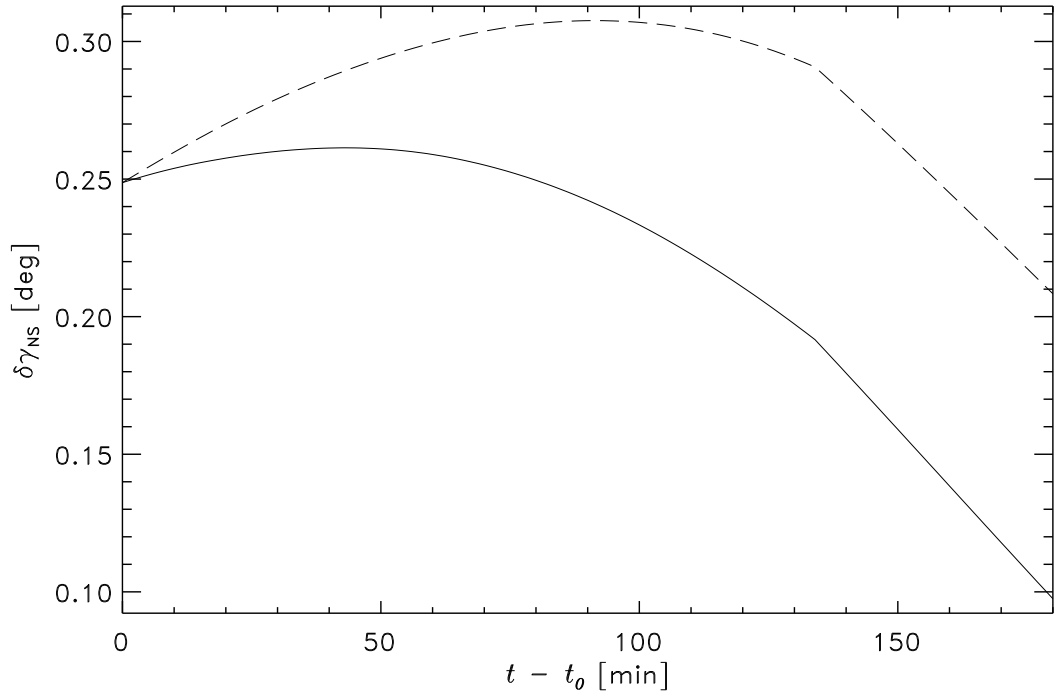

Figure 5.31: Error of meridional Doppler wind component angle. The solid (long-dashed) line shows the prograde (retrograde) case.

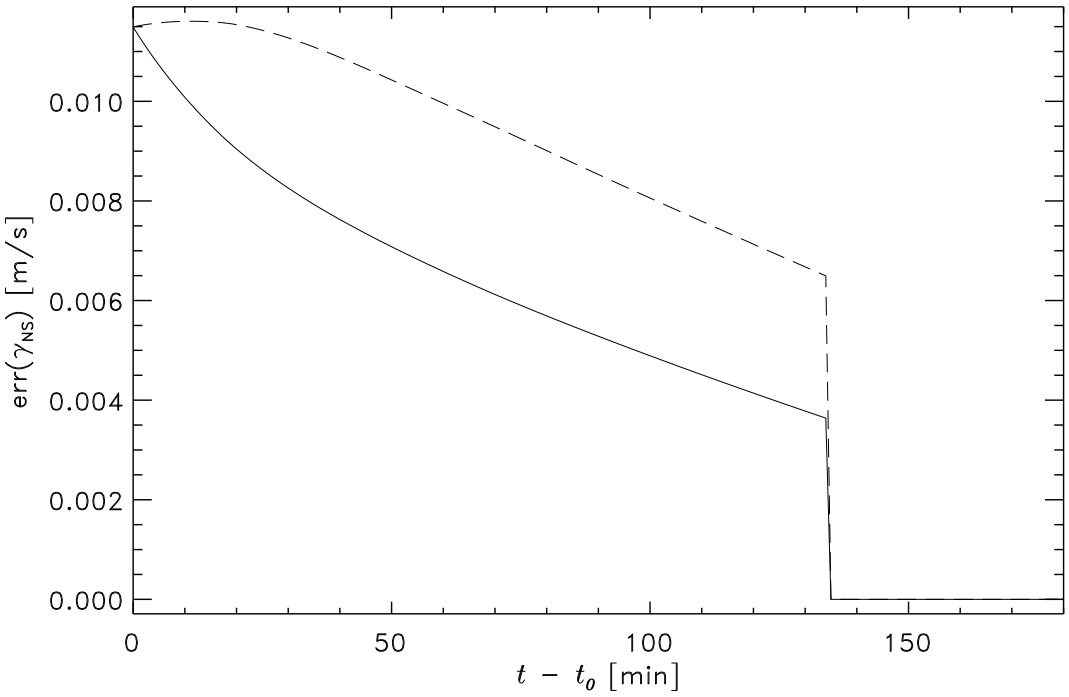

Figure 5.32: Error contribution from inaccurate meridional Doppler wind component. The solid (long-dashed) line shows the prograde (retrograde) case.

5.6.9 Cassini Observation Angle

The Cassini observation angle γ_C is defined as the angle between the Cassini velocity vector $\vec{v}_C$ and the LOS vector pointing from Cassini to Huygens. Fig. 5.33 shows the evolution of this angle during the Huygens mission. There

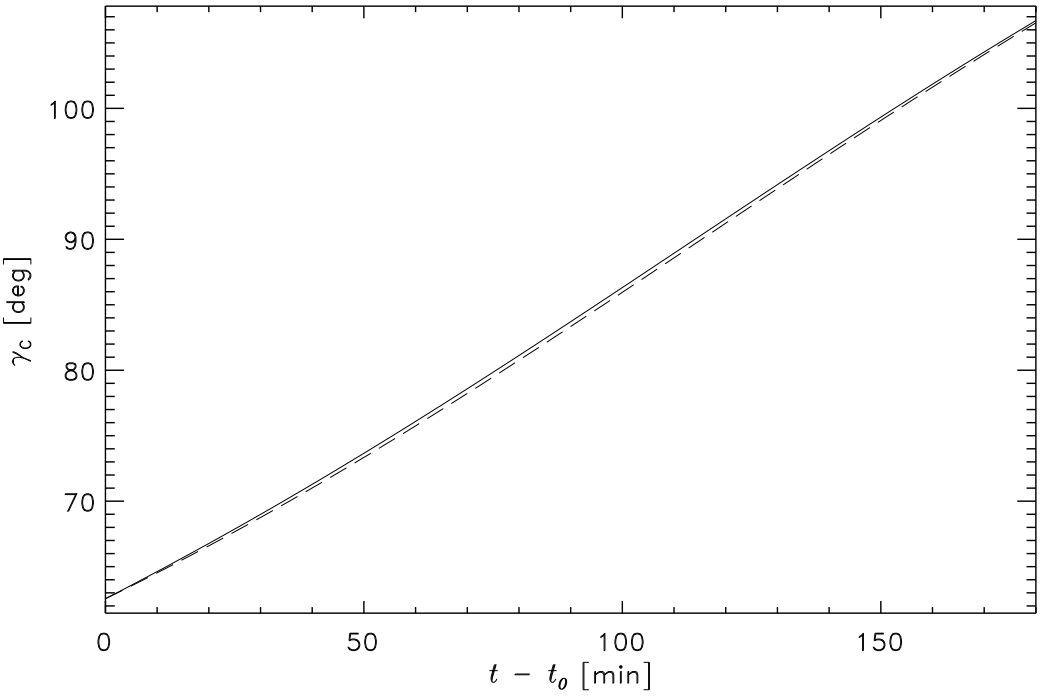

Figure 5.33: Evolution of the angle between the Cassini velocity and the LOS. The solid (long-dashed) line shows the prograde (retrograde) case.

is very little difference between the prograde and retrograde case, because the LOS vector is much longer than the difference between the Huygens position in both cases.

The error contribution from this parameter is given by

$$\mathrm{err}(\gamma_C) \;=\; \left| \frac{\partial v_{EW}}{\partial \gamma_C} \delta\gamma_C \right| \;=\; \left| -\frac{v_C}{\cos\gamma_{DWC}} \sin\gamma_C \delta\gamma_C \right| \qquad (5.34)$$

$\delta\gamma_C$ is constructed from the position errors of Cassini and Huygens. As above, Cassini's contribution to $\delta\gamma_C$ is $\delta x_C / x_{LS}$. In order to determine the contribution of the Huygens position error, we make use of the following plausible approximations: (a) The LOS, $\vec{v}_C$ and $\vec{v}_{EW}$ are located in the same plane. (b) The altitude error of the Huygens position is negligible with

respect to its longitudinal error. (c) The longitudinal error is a straight line rather than an arc of a circle. With these approximations, the contribution of the Huygens position error is given by the longitudinal error projected onto a line perpendicular to the LOS and in the plane spanned by $\vec{v}_C$ and $\vec{v}_{EW}$ ($\delta lon_H \cdot R_T/x_{LS} \cdot \sin\gamma_{DWC}$).

Another contribution to $\delta\gamma_C$ originates from the direction error of the Cassini velocity $\vec{v}_C$. For the construction of the angular errors $\delta\gamma_{DWC}$, $\delta\gamma_{des}$ and $\delta\gamma_{NS}$, the directional errors could be omitted because the velocities v_{EW}, v_{des} and v_{NS} are in fact one-dimensional parameters (see previous subsections). $\vec{v}_C$, however, is a three-dimensional vector and its directional inaccuracy must taken into consideration. $\delta\gamma_C$ can thus be written as

$$\delta\gamma_C = \sqrt{(\frac{\delta x_C}{x_{LS}})^2 + (\delta lon_H \cdot \frac{R_T}{x_{LS}} \cdot \sin(\gamma_{DWC}))^2 + (\frac{\delta v_C}{v_C})^2} \qquad (5.35)$$

The first two terms in the square root of Eq. (5.35) are about of the same order of magnitude ($\sim 10^{-4}$). The third term, which accounts for Cassini's directional velocity error, has been set to 10^{-5} for this analysis. The resulting error is displayed in Fig. 5.34.

The error contribution from $\delta\gamma_C$ (err(γ_C); Fig. 5.35) is rather large due to the large value of the Cassini velocity ($\sim$ 5.7 km s^{-1}). It is in fact the largest contribution computed and dominates during the entire descent. The only way to reduce this error contribution is a better determination of the positions of Cassini and Huygens.

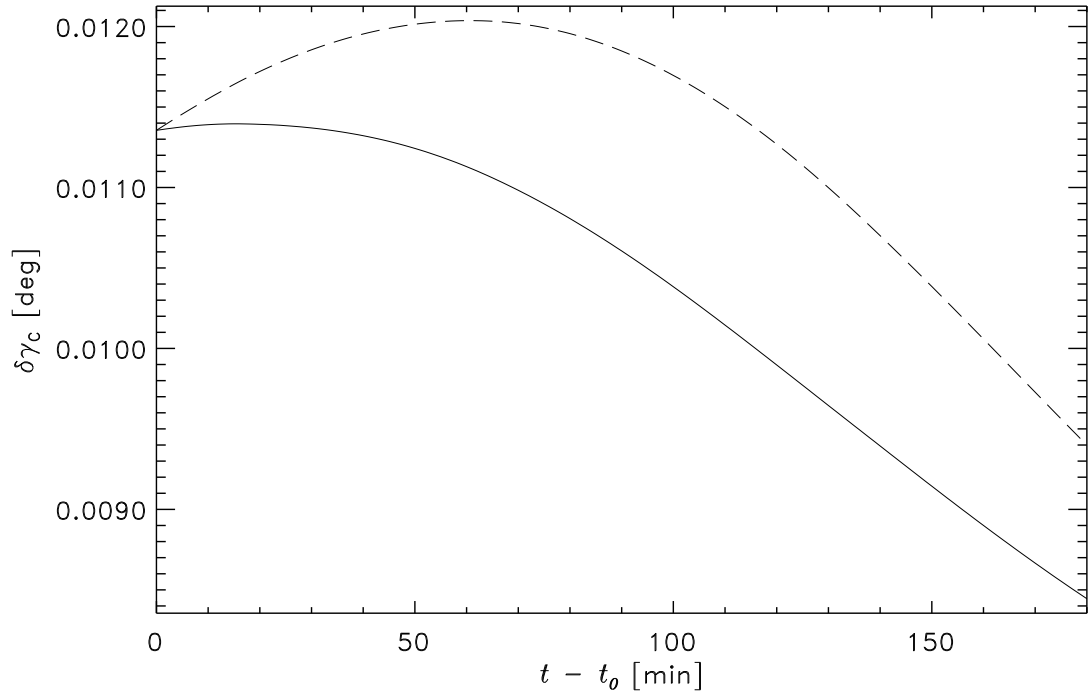

Figure 5.34: Error of Cassini observation angle. The solid (long-dashed) line shows the prograde (retrograde) case.

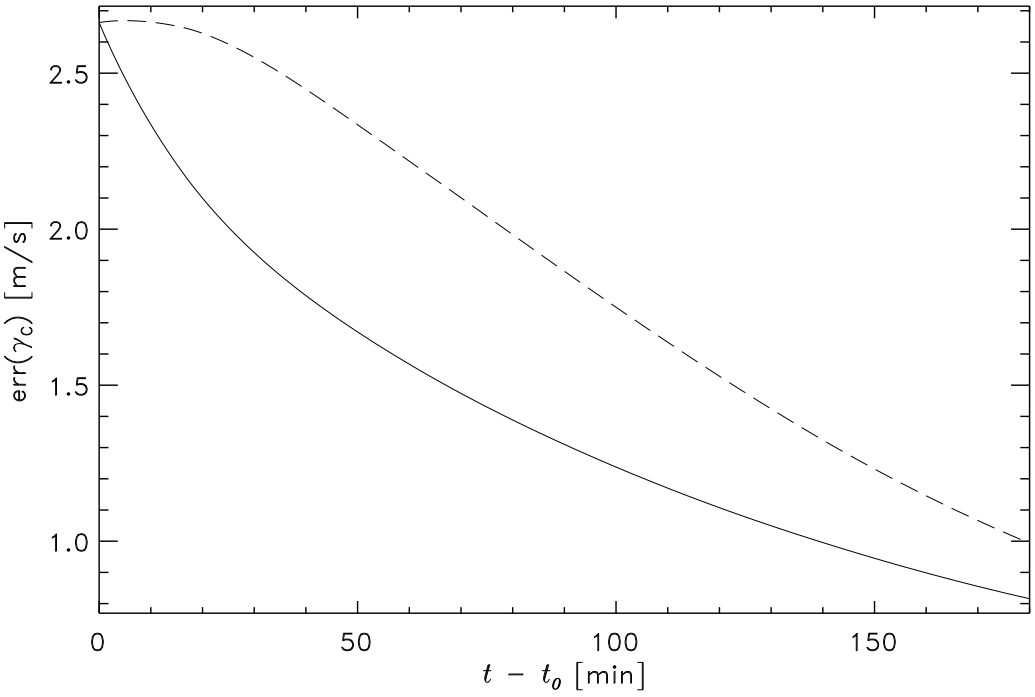

Figure 5.35: Error contribution from inaccurate Cassini observation angle. The solid (long-dashed) line shows the prograde (retrograde) case.

5.6.10 Spin

The data measured during the descent are transmitted redundantly on the two channels A and B. Each channel has its own dedicated transmitting antenna (PTA). The polarizations are circular with left hand circular polarization (LHCP) for the signal transmission at $f_{0,A} = 2040$ MHz and right hand circular polarization (RHCP) for the signal at $f_{0,B} = 2098$ MHz. Both antennae are located on the top side of the experiment platform, about 30 cm away from the rotation axis. The expected spin profile during the descent is shown in Fig. 5.36 (Alcatel, 1997a).

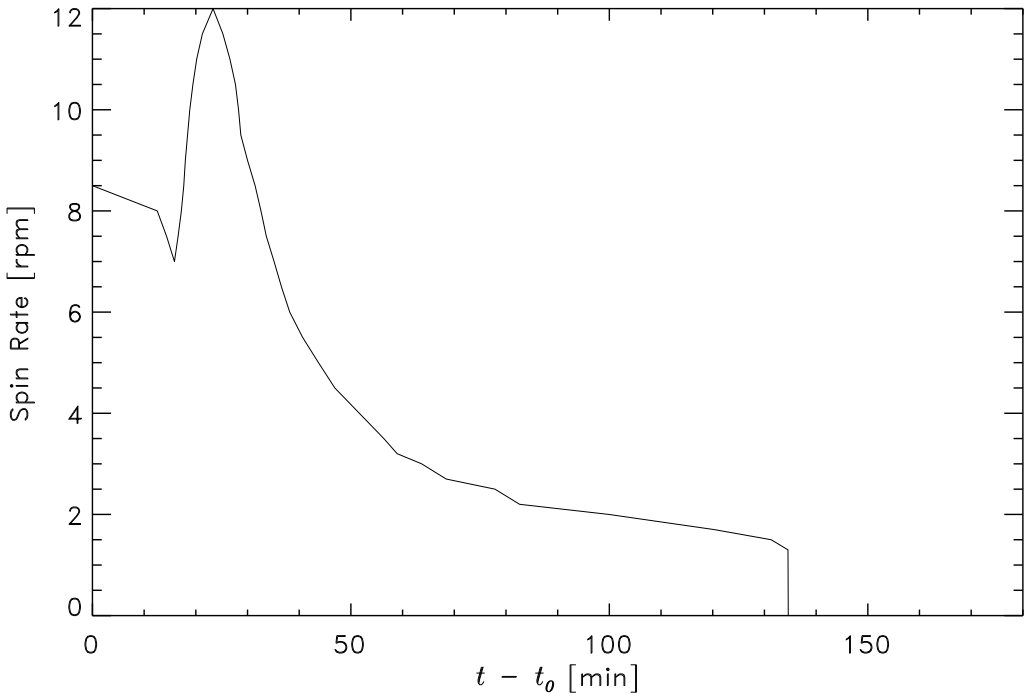

Figure 5.36: Expected spin profile of Huygens during the descent.

Spin has not been listed as a parameter in Eq. (5.16). Nevertheless, it is clear that it contributes to the Doppler shift of the received signal due to the off-axis position of the PTA. Its impact, however, depends on the moving average filter applied to the original frequency data and on the actual spin rate. For example, a moving average filter with a width of 43 samples (equivalent to a period of 5.375 sec) will effectively filter out a spin rate of 11.2 rpm. Low spin rates around 2 rpm, which are expected during the second half of the descent, will remain virtually unmodified. Their impact,

however, is small due to the low angular velocity. In this subsection, we discuss the impact of the spin on the original frequency data.

The direction of the Huygens rotation is counter-clockwise as one looks from the top. While spinning, the off-axis position induces a small Doppler shift $f_{D,spin}$ on the transmitted signal. The effect can be described by

$$f_{D,spin,i} = \frac{f_0}{c} \cdot 2\pi \cdot f_{spin,i} \cdot r_{off} \cdot \cos(\phi_{ini} + 2\pi \cdot dt \cdot \sum_{j=0}^{i} f_{spin,j}) \cdot \sin(\gamma_{des}) \quad (5.36)$$

where $f_{D,spin,i}$ is the Doppler shift due to spin on the ith sample, f_{spin} is the spin rate from Fig. 5.36, r_{off} is the radial offset of the antenna position ($\sim$30 cm), dt is the sampling period (0.125 sec) and $\sin(\gamma_{des})$ is the projection onto the LOS. The initial spin phase ϕ_{ini} is, of course, arbitrary and unpredictable.

The resulting velocity contribution $v_{spin,LOS} = -f_{D,spin} \cdot c/f_0$ is displayed in Fig. 5.37 for prograde winds and for an initial phase $\phi_{ini} = 0°$. It appears

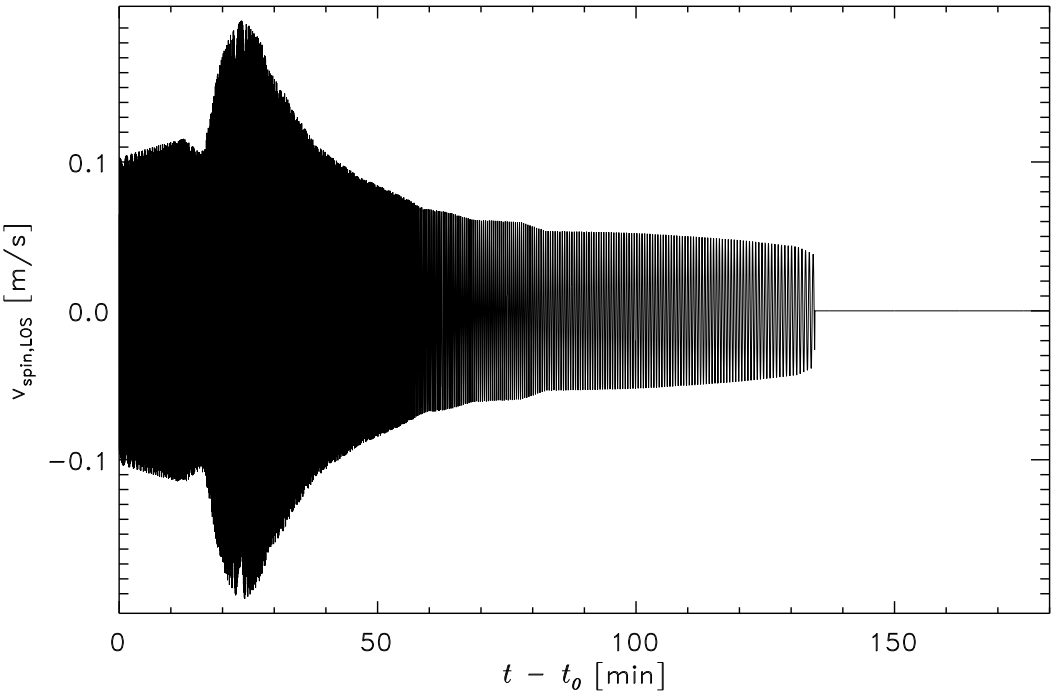

Figure 5.37: Velocity contribution due to PTA off-axis position.

as an oscillation with varying amplitude and frequency that changes the reconstructed zonal wind speed by not more than $\pm$20 cm s^{-1} (from the

Doppler shift of ±1.4 Hz). The projection onto the LOS is slightly smaller in the retrograde case (not more than ±15 cm s^{-1} or ±1 Hz), but follows the same shape as in Fig. 5.37.

Another velocity contribution due to spin is caused by the PTA phase pattern (Fig. 5.38). While the PTA spins with Huygens, the initial phase of the transmitted signal varies with the azimuth ϕ. As frequency is the time derivative of phase, this effect induces a Doppler component $f_{D,pp}$ on the received frequency, which can be calculated from

$$f_{D,pp} = \frac{1}{2\pi}\frac{\partial\Phi}{\partial t} = \frac{1}{2\pi}\frac{\partial\Phi}{\partial\phi}\cdot\omega \tag{5.37}$$

where Φ is the initially transmitted phase, ϕ is the azimuth angle and $\omega/2\pi$ is the Huygens spin rate (Fig. 5.36). This Doppler component is shown in Fig. 5.39 for $\omega/2\pi = 1$ rpm.

With increasing azimuth (counter-clockwise rotation), the maximum blueshift due to the PTA phase pattern is achieved at an azimuth angle $\phi \approx 310°$, the maximum redshift occurs at ~130°. The azimuth angle of the position of the PTA dedicated to channel A is 235° (Alcatel, 1997a). Thus, the maximum blueshift due to the PTA off-axis position is achieved at $\phi = 235° + 90° = 325°$, the maximum redshift at 145°.

Both effects have approximately the same magnitude and are almost in phase (separated by only about 15°). The combined effect will thus appear as shown in Fig. 5.37 with the ordinate multiplied by a factor of ~2. However, as outlined above, the true impact of this effect on the filtered frequency data depends on the applied moving average filter. It may be possible to extract the spin rate and phase by calculating the residuals between the original unfiltered frequency data and all velocity contributions including the zonal velocity contribution retrieved by this algorithm. A correlation analysis with the signal level data (AGC), which also depend on the azimuth, and radial accelerometer data (Jones *et al.*, 1997) could support this process.

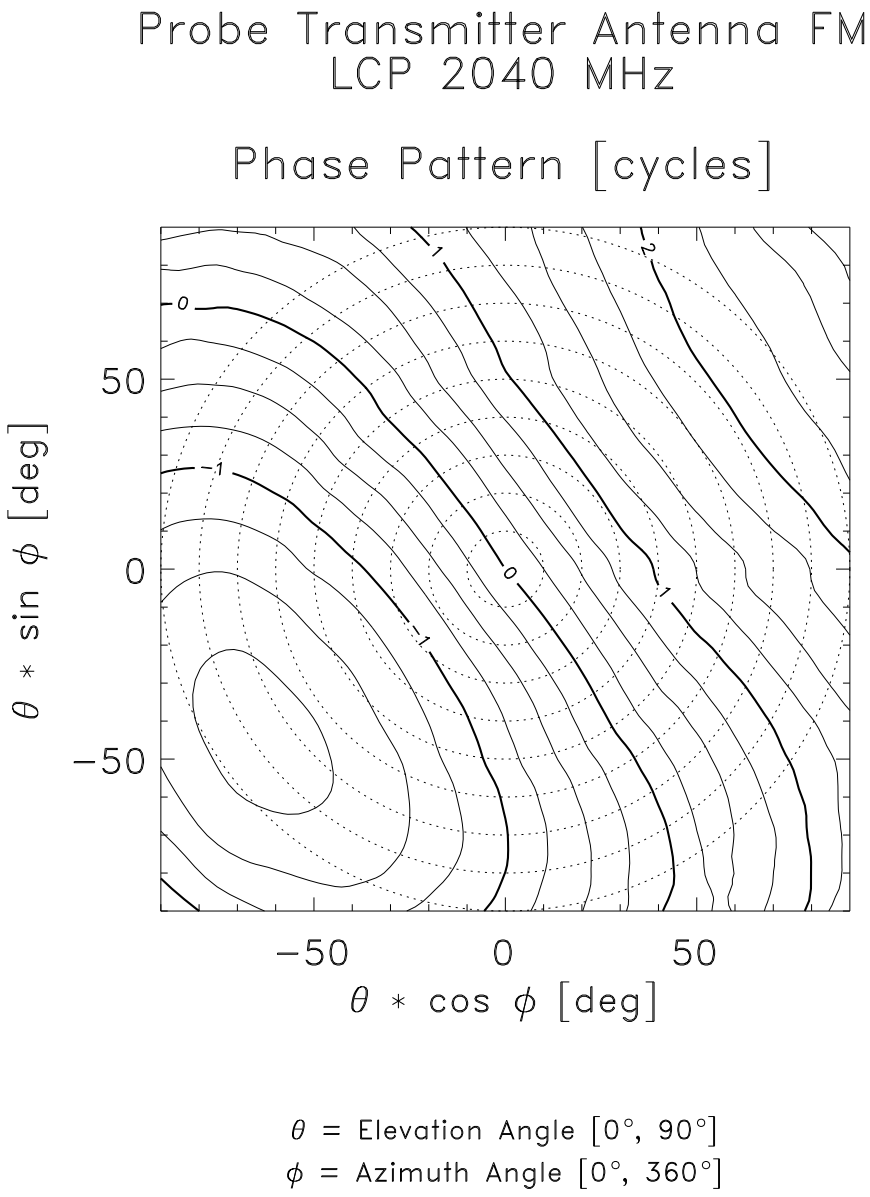

Figure 5.38: Huygens PTA phase pattern. The elevation angle θ is equal to the PAA.

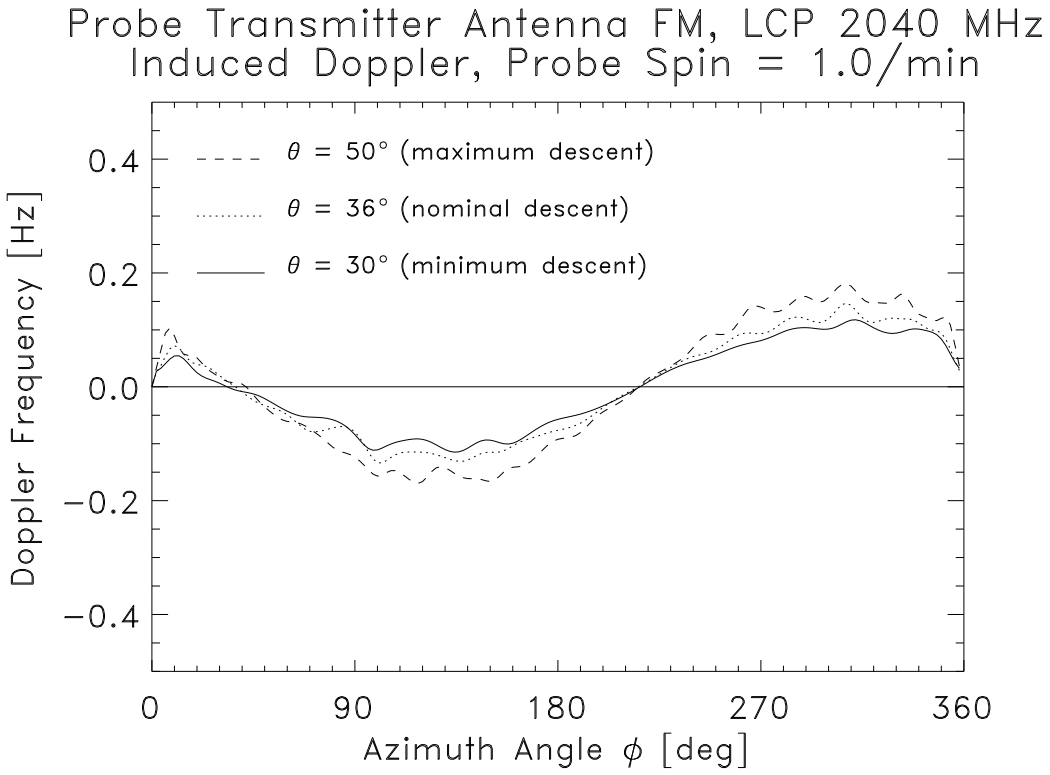

Figure 5.39: Doppler shift caused by PTA phase pattern for various elevation angles θ. The Doppler shift was calculated for a Huygens spin rate of 1 rpm.

5.6.11 Summary and Open Issues

We have analyzed the predicted variation and error contribution of all nine parameters in Eq. (5.16), summed together according to Eq. (5.17). Summaries of the results are shown in Figs. 5.40 and 5.41 for prograde winds

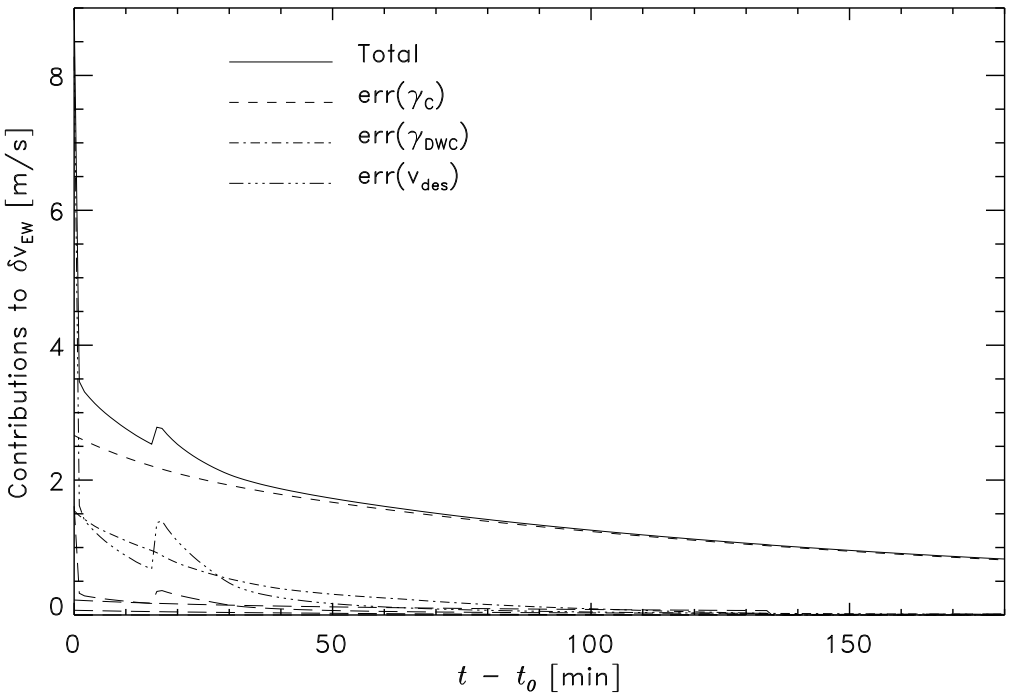

Figure 5.40: Error contributions to δv_{EW} for prograde winds. Minor contributions are shown as long dashes and resolved in the next figure.

and in Figs. 5.42 and 5.43 for retrograde winds. The figures do not show the error contribution err(γ_{NS}), because it is less than 1 cm s^{-1} for most of the descent, even when a meridional wind of a constant 1 m s^{-1} is applied. Also, err(v_{rot}) is not plotted as it was concluded that this contribution is essentially 0.

Due to the negligible impact of a variation of γ_{NS}, the picture does not change when meridional motions are taken into account. When constant meridional motions of 1 m s^{-1} (south) or -1 m s^{-1} (north) are applied, the plots presented here display virtually identical shapes. To conclude, meridional winds in the expected range (< 1 m s^{-1}) have basically no impact on the DWE zonal wind retrieval.

The largest error contribution stems from inaccurate modelling of the

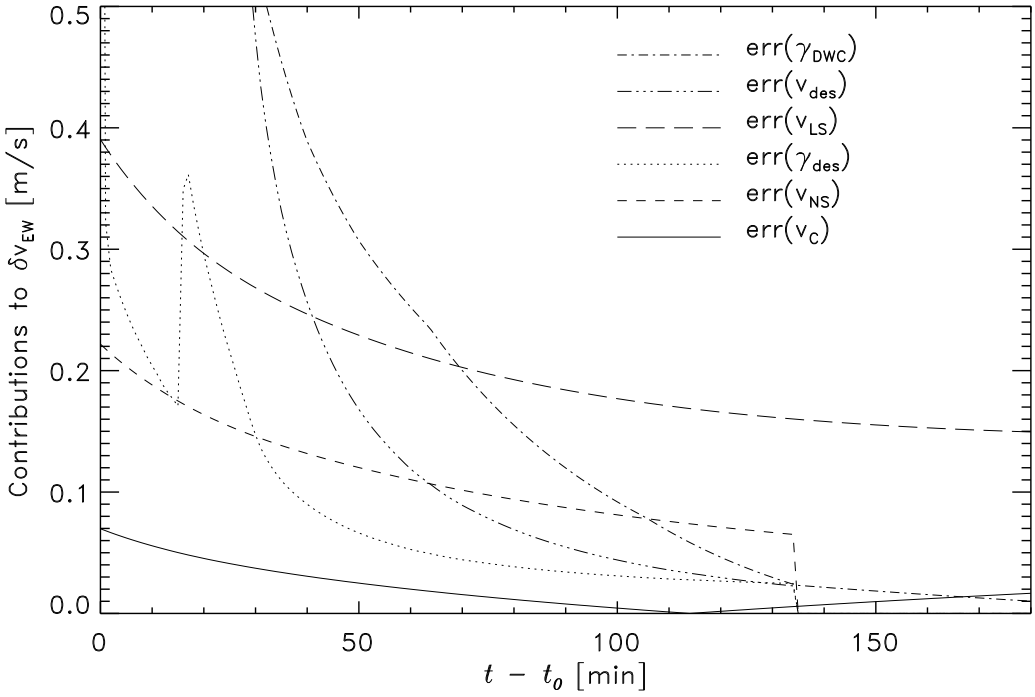

Figure 5.41: Detail of Fig. 5.40 with expanded ordinate.

angle between the LOS and the Cassini velocity γ_C. The error contribution resulting from an inaccurate descent velocity is dominant only during the first minute after t_0, because here the descent velocity v_{des} is still rather large and the error was assumed to be $v_{des}/100$. However, the PRL is established 2.5 minutes after t_0 during the descent according to the currently valid mission timeline. At this moment, the Huygens descent velocity is already smaller than 60 m s^{-1}.

The accuracy of γ_C and its contribution to the total error of the retrieved zonal wind speed depends on the position accuracies of both Huygens and Cassini. This can be seen in Figs. 5.44 and 5.45 which were calculated with a Cassini position accuracy of $\delta x_C = \pm 100$ m, in contrast to $\delta x_C = \pm 10$ km used earlier. If the determination of the Cassini position is possible to this accuracy, the accuracy of the retrieved zonal wind speed can be significantly increased, i.e. in the prograde case.

The initial Huygens position error is random. The distribution of possible Huygens positions in the circularized delivery error ellipse is Gaussian. However, an erroneous value for the initially retrieved zonal wind speed produces a systematic error in the Huygens longitudinal position which decreases with

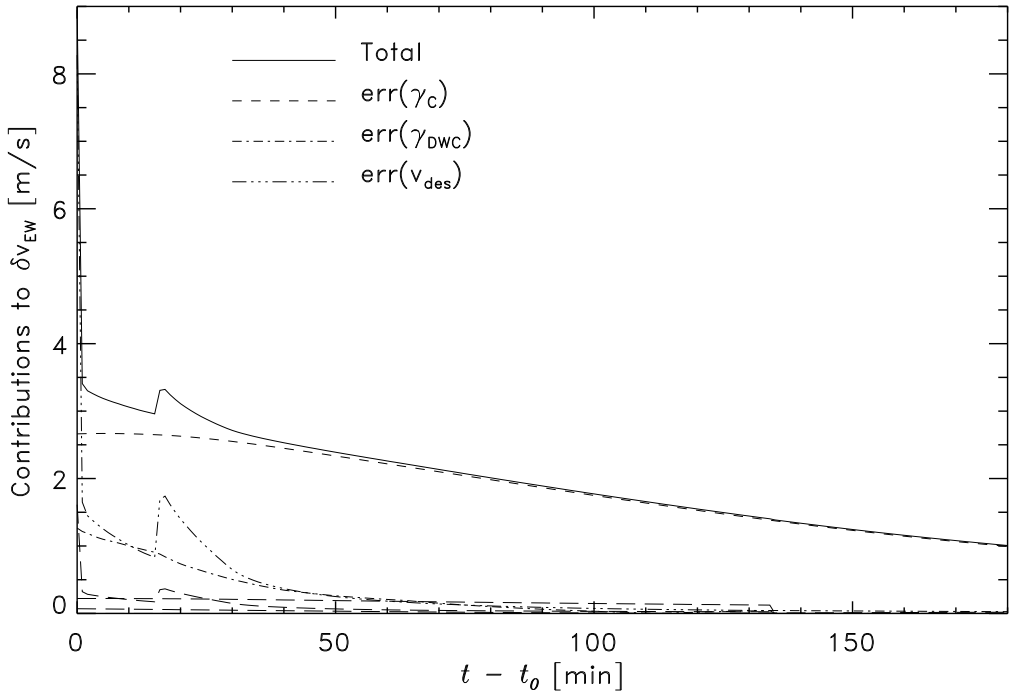

Figure 5.42: Error contributions to δv_{EW} for retrograde winds. Minor contributions are shown as long dashes and resolved in the next figure.

time. This decrease has not been taken into account in this analysis. The error contributions that involve δlon_H, err(γ_{DWC}) and err(γ_C), may therefore be slightly overestimated.

Assuming that the error on the retrieved zonal wind speed is entirely given by a wrong initial Huygens longitude, it is possible to compute the decrease of the longitudinal position error by setting

$$\delta lon_{H,i} = \delta lon_{H,0} - \frac{dt}{R_T} \cdot \sum_{j=0}^{i-1} \delta v_{EW,j} \tag{5.38}$$

until $\delta lon_{H,i} = 0$. It is clear that this overestimates the decrease of the longitudinal position, but it is useful for assessing the impact of the use of the constant longitudinal position error. Letting δlon_H decrease according to Eq. (5.38) results in a nearly linear decrease of δlon_H. It reaches 0 after 130 minutes in the prograde case and after 95 minutes in the retrograde case. The result of this analysis is plotted in Figs. 5.46 and 5.47. From a comparison of these figures with Figs. 5.40 and 5.42 it becomes clear that

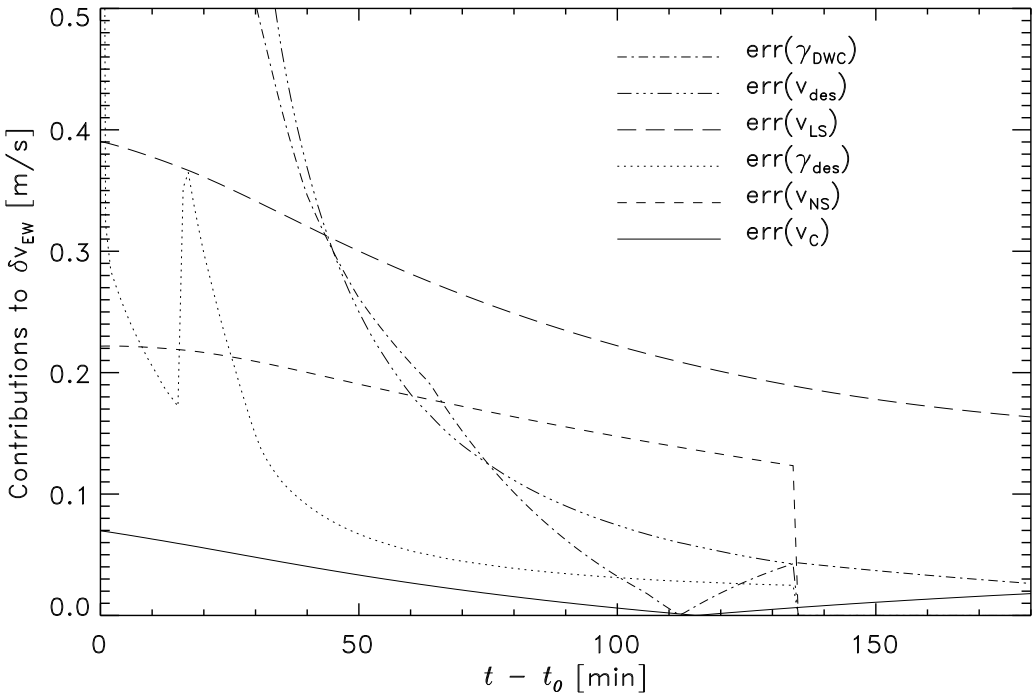

Figure 5.43: Detail of Fig. 5.42 with expanded ordinate.

the use of a constant value for δlon_H overestimates the error contributions in fact only slightly.

The largest error contributions presented here are of systematic nature. As a result, the wind shear profile is more accurate than the profile of absolute winds. Changes of the zonal wind speed can be resolved to an accuracy equal to the largest *random* error contribution. For the first ∼50 min, this is the descent velocity error contribution err(v_{des}), considering a random error of 1% on the descent velocity. Later, it is limited by the DWE measurement error contribution err(δv_{LS}), which is also considered random.

The unfiltered spin contribution to the LOS velocity is expected to be near the maximum contribution of the random errors δv_{des} and δv_{LS}. As our approach in this analysis was conservative, it is likely that we slightly overestimate the random errors.

As outlined above, DWE needs to know the position at the moment of PRL acquisition ($\sim t_0$) as accurately as possible. The initial position error was assumed to be 12 km. This number is provided by the JPL navigation team and originates from the Huygens delivery error in the B-plane (Fig. 3.1). However, the delivery error is defined for an altitude of 1270 km, the so called

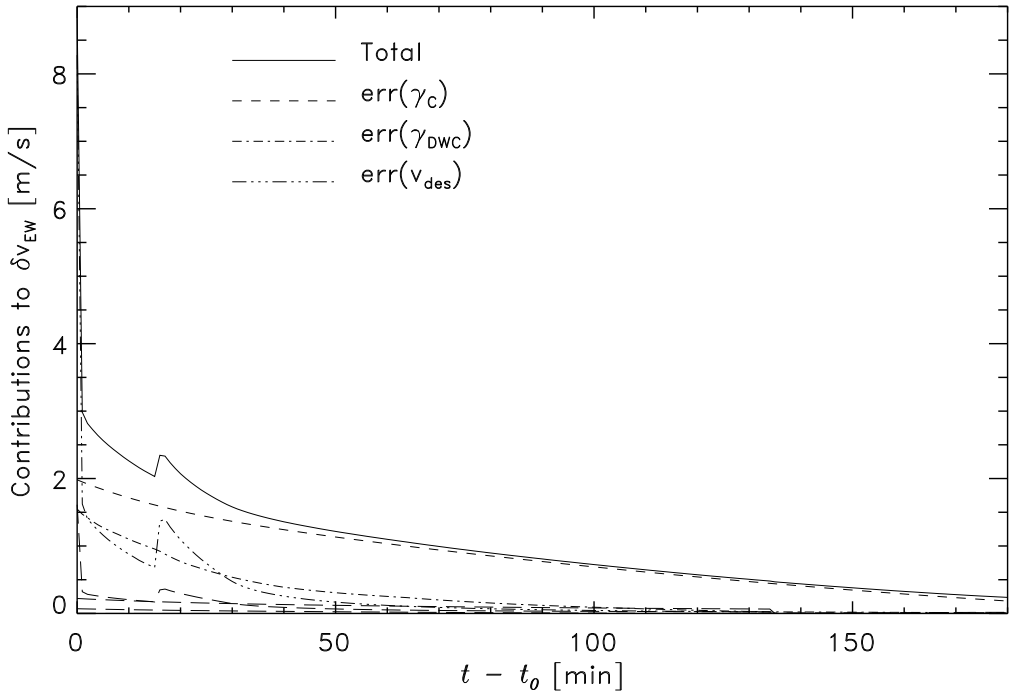

Figure 5.44: Error contributions to δv_{EW} for prograde winds. The Cassini position error was set to $\pm$100 m.

"interface altitude", where the responsibility of JPL terminates. The motion during the entry phase, which is defined to start at the interface altitude and end when the first parachute is ejected at about 160 km altitude and which may last more than 4 min, is still subject to investigation.

The true initial longitudinal position of Huygens certainly differs from its value at the interface altitude. The amount, by which it differs, depends on the acceleration forces, the entry angle and the B-plane angle. It is anticipated that the Huygens longitude at interface altitude is 172.5°E. Current models suggest that 4.5 min later, at t_0 (altitude 165 km), it is at 160.8°E (Kazeminejad, 2001). Due to the B-plane angle of 190°, the latitudinal drift during entry is small. HASI will perform acceleration measurements during this phase, by which the trajectory can be reconstructed. The achievable accuracy, however, is not yet clear (Atkinson, 1998).

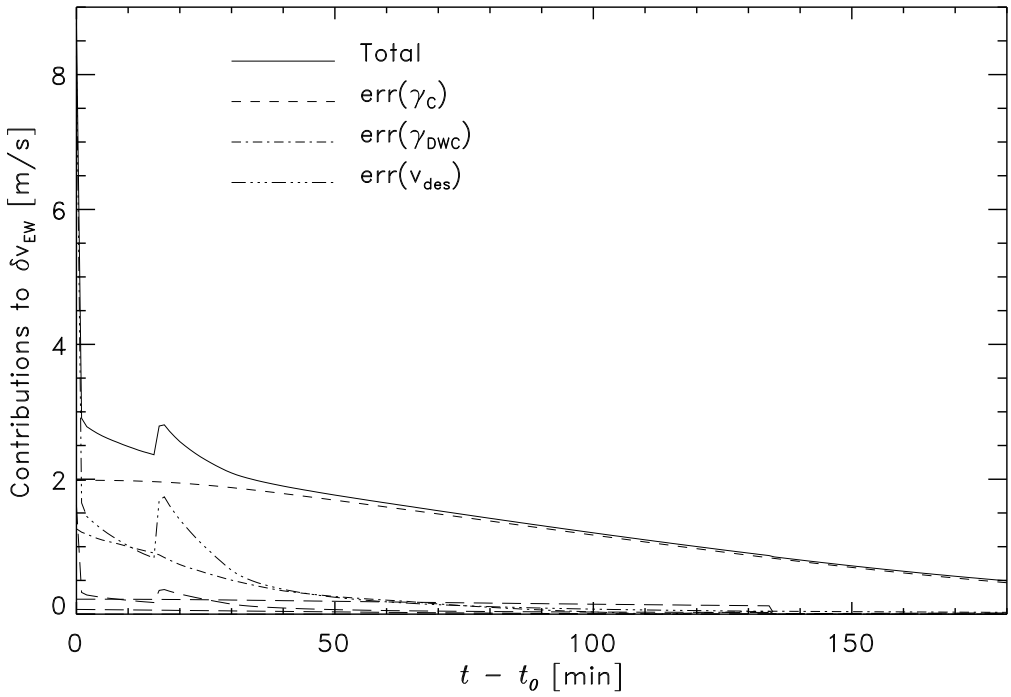

Figure 5.45: Error contributions to δv_{EW} for retrograde winds. The Cassini position error was set to ± 100 m.

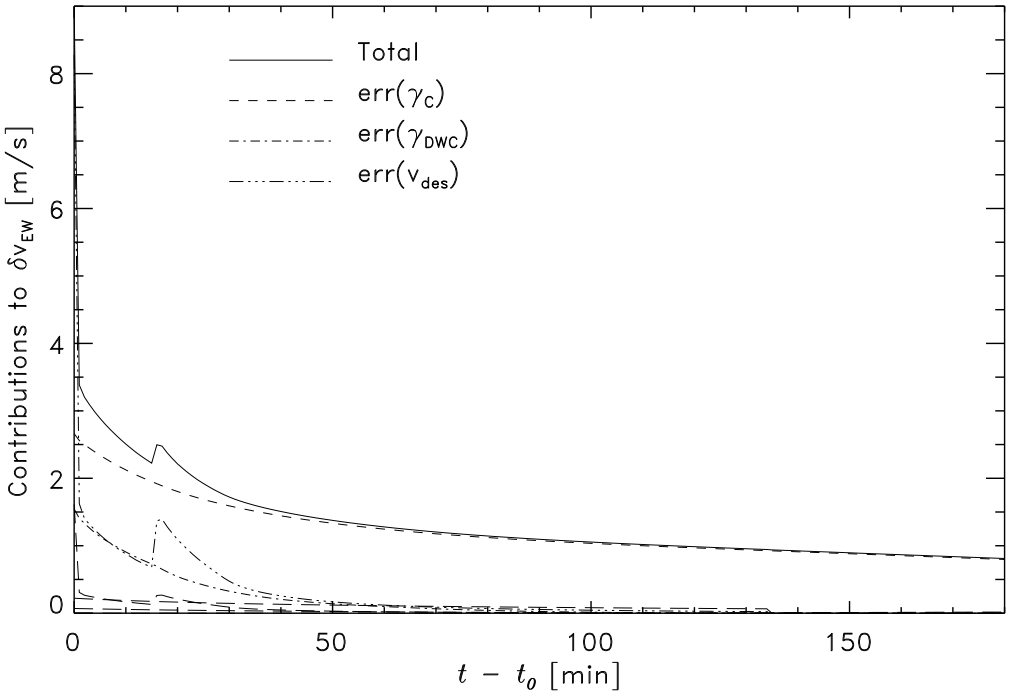

Figure 5.46: Error contributions to δv_{EW} for prograde winds. δlon_H was modified to decrease for this analysis (see text).

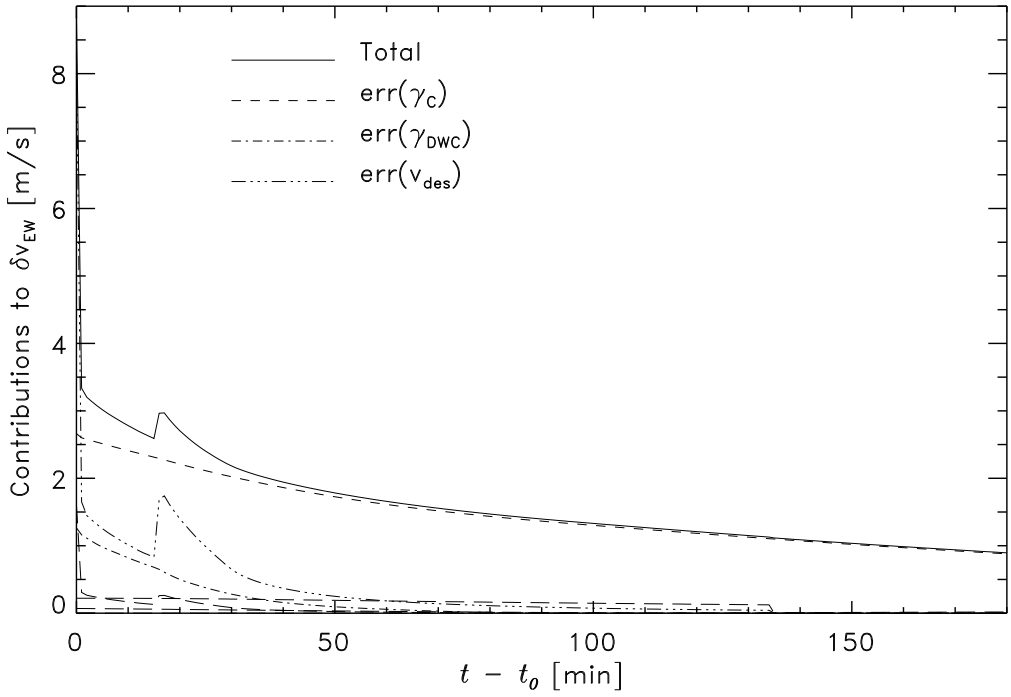

Figure 5.47: Error contributions to δv_{EW} for retrograde winds. δlon_H was modified to decrease for this analysis (see text).

Chapter 6

Deriving the Zonal Wind Speed

The algorithm presented in the previous chapter has been tested by combining modeled range rates (e.g. Fig. 5.8) with frequency data from the eighth in-flight checkout (F8; Fig. 4.5). The simulated DWE frequency data were constructed by adding the F8 frequency samples $f_{R,F8}(t_i)$ as a "zero" reference to the frequency expected from the range rate $v_{LS}(t_i) \cdot f_0/c$. Furthermore, the spin contribution expected from Eq. (5.36), multiplied by a factor 2 to account for the phase pattern effect, was included in the Huygens mission simulation data. The simulated data are shown in Fig. 6.1 for prograde winds. The zonal wind profile is retrieved from the simulated data in the following by (1) applying the offset calibration, (2) filtering spurious oscillations and (3) extracting other Doppler contributions.

The first step of the zonal wind retrieval is applying the offset calibration. It has been shown in Subsection 4.4.2 that the offset between f_0 and the reference frequency is a function of the frequency oscillation amplitude A_{osc}, which can be retrieved by applying a 10-sec moving average filter to the data and subtracting the result from the original data. This operation is displayed in Fig. 6.2. Comparing the oscillation amplitude retrieved by this procedure with the one measured during F8 (Fig. 4.7) shows only minor deviations. Obvious failures of this procedure, as can be seen at t_0 and at $t_0 + 15$ min, are corrected manually before the calibration is applied. These failures are caused by rapidly changing descent velocities right after t_0 and at the exchange of the parachutes at t_0+15 min. The offset correction $f_{off}(A_{osc})$ is then given by Eq. (4.6).

It should be noted here that the correlation between A_{osc} and f_{off} is weak during the first 20-30 minutes after t_0. As the drift stability of the USOs increases with operation time, the reason for this behavior may lie in

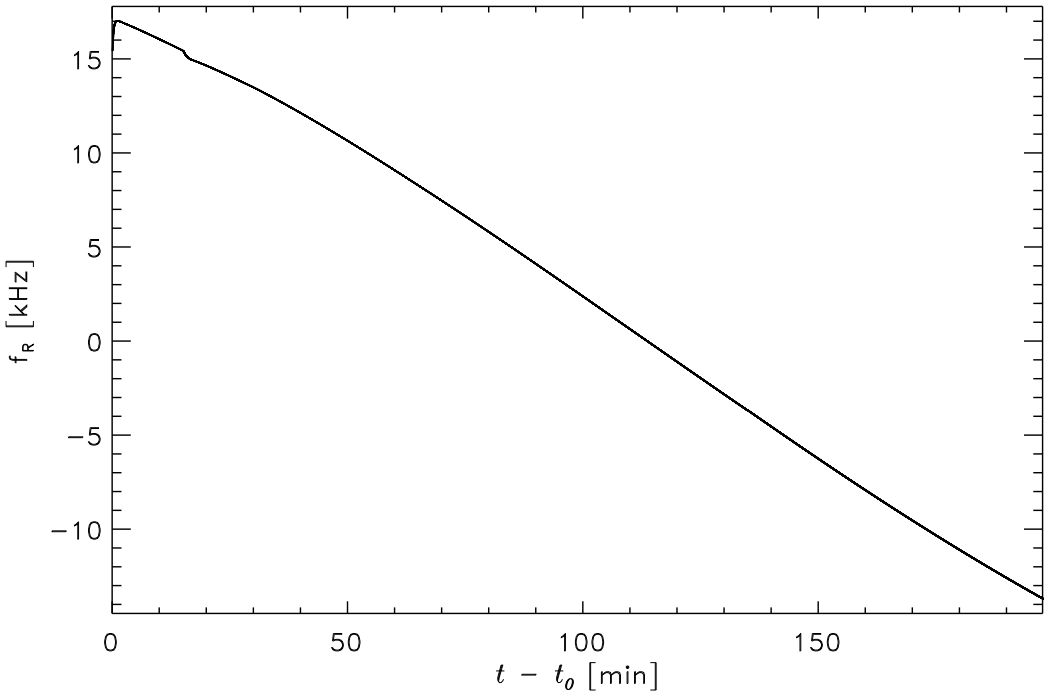

Figure 6.1: DWE model data for prograde Flasar wind.

the TUSO, which is switched on together with Huygens at about $t_0 - 35$ min in a PCO. The RUSO is switched on together with the PSA at $t_0 - 60$ min and should therefore have a more stable output frequency. The Huygens project is currently discussing the possibility to switch on the Huygens Probe 3-4 hours prior to the entry, in contrast to the originally planned 30 minutes. The reason for this is the positive offset of the CDMU clock mentioned above, which drifts towards more nominal values while warming up during operation. If such a pre-heating phase is implemented, the problem mentioned here will most probably have vanished. However, if it is rejected, it should be kept in mind that during the first 20 minutes after start of the descent, the carrier frequency measurement f_R may be in error by up to -2 Hz, even after applying the offset calibration.

The second step is filtering noise and spurious oscillations by applying the moving average filter described in Section 5.4. Here, we integrate over 43 samples corresponding to a filter with a width close to twice the period of the most dominant frequency oscillation $2/f_{osc}$. It filters out all strong spurious lines except the one at 0.00367 Hz (corresponding to a period of 4.5 min). This rather strong line, seen on the left edge of the spectrum

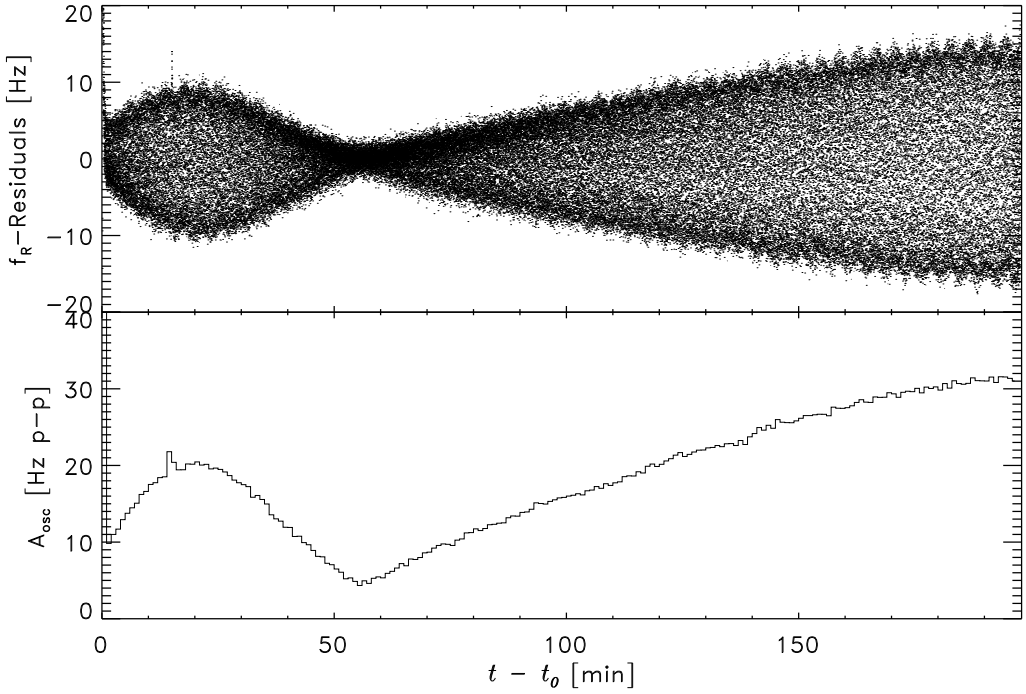

Figure 6.2: f_R smoothing residuals and resulting A_{osc}. The residuals (upper panel) were constructed by subtracting a running mean of the simulated data of Fig. 6.1, smoothed over 10 sec (filtered with a 81-sample moving average filter), from the original data. A_{osc} (lower panel) was computed by subtracting the mean of the ten smallest frequency values measured during one minute (480 samples) from the mean of the ten largest frequency values measured during the same minute.

shown in Fig. 4.4, can be constructed from Eq. (4.5) with $i = 0$, $j = -1$ and $k = 2$.

Finally, the other velocity contributions except spin are extracted. As outlined in the previous sections the Cassini position and velocity are provided by JPL. The Huygens descent velocity is initially provided by on-board systems and later by the measurements of other experiments. Here, we use the same model descent velocity as has been used to construct the model data (Fig. 5.7). The Huygens meridional velocity is set to 0. This value will also be used for the initial evaluation after the Huygens mission, but may be suited to more realistic values when they become available from other measurements. The Huygens position, particularly the longitude at the beginning of the data transmission, taken here as t_0, will be provided by ESA and *a posteriori* by HASI acceleration measurements. As the accuracy of the

Huygens longitudinal position is one of the largest systematic DWE error source, the algorithm was tested with various longitudinal offsets between the true initial Huygens longitude ("true longitude") used for the construction of the simulation data and the longitude used in the zonal wind retrieval ("retrieval longitude").

The moving average filter (second step) could actually be applied *after* the extraction of the other Doppler contributions (third step). However, applying the offset calibration should be the first step, because the zonal wind retrieval is an iterative process and any error in the determination of the absolute frequencies has a direct impact on the evaluation of the remaining samples, particularly the determination of the Huygens longitudinal position. When steps 2 and 3 are reversed, the frequency oscillation affects the retrieved zonal wind speed and thus the retrieved Huygens longitude. However, any position error is virtually compensated within one oscillation phase.

Fig. 6.3 shows the ideal case, where Huygens was not subject to meridional motion and true and retrieval longitude are identical. The simulation data have been constructed using prograde Flasar winds. It must be noted that the residual is rather large at the start of the descent (see Fig. 6.4, which shows the first minute of Fig. 6.3 with an expanded ordinate). This may be explained by the fact the the descent velocity changes rather rapidly during this phase. The change is smoothed over by the integration of step 2. Furthermore, the moving average filter breaks down at the beginning and at the end of the measurement, because of a lack of integratable samples. The observed behavior is virtually identical in all cases presented in the following. Fig. 6.5 shows the same analysis for retrograde winds.

The simulated data for Figs. 6.6-6.9 were constructed applying additionally constant meridional motions of ± 1 m s^{-1} for both prograde and retrograde zonal winds. As above, the retrieval program assumes a value of 0 for this velocity component. Even with this unrealistically high meridional velocity, the zonal wind retrieved is almost identical to those shown in Figs. 6.3 and 6.5. A small difference of ± 15 cm s^{-1} is visible during the first $\sim$30 minutes, which represents the typical influence of a 1 m s^{-1} meridional wind. Due to the observation geometry, which is very unfavorable for the meridional direction, this is an expected result. From these figures, it is clear that meridional motion even faster than predicted by most Titan wind models cannot corrupt the DWE measurement.

The sensitivity of the DWE to the longitudinal position of Huygens can be seen in Figs. 6.10-6.13. The simulated data for these plots were constructed as above with a true longitude at t_0 of 161.4°E, but the retrieval program now assumes that the Huygens position at t_0 was 50 km or 1.1° East or West of the true longitude. The effect of a wrong retrieval longitude on the

retrieved zonal wind speed is an offset to the real value. The offset decreases during the mission, because the longitudinal position error tends to decrease (see Subsection 5.6.6) and the observation geometry improves. If the zonal winds are prograde and the retrieval longitude is west of the true longitude, the retrieved zonal wind speed is slightly overestimated. On the other hand, if the zonal winds are retrograde and the retrieval longitude is west of the true longitude, the retrieved zonal wind speed is slightly underestimated. If the retrieval longitude is east of the true longitude, we get the opposite effect. The longitudinal position error of 1.1° or 50 km is thereby reduced to ∼0.5° or ∼20 km in all cases. This can be seen in Figs. 6.14-6.17, which show the evolution of the difference between the true longitude used for the construction of the simulated data and the longitude used by the retrieval program ($lon_{retrieved} - lon_{true}$).

After touchdown ($t > t_0 + 135$ min), it can be seen in the lower panels of those figures that the longitudinal offset produces an apparent zonal wind speed, which is systematically different from 0. It may be possible to calculate the longitudinal position error from this offset. However, it cannot be excluded that the impact on Titan's surface would produce a random frequency shift in the TUSO. It is clear that this would make such an analysis impossible.

An erroneous initial longitude leads to a systematic error, but does not change the random error. Therefore, the zonal wind shear profile is virtually unaffected by positional errors. Fig. 6.18 shows the zonal wind retrieval in the case of a zonal wind gust in the altitude range 50-60 km with an amplitude and a spatial scale according to Table 5.2. The same case, but with a longitudinal offset of 50 km towards East is displayed in Fig. 6.19. It can be seen here that the shape of the gust is perfectly resolved, even when the absolute values of the retrieved zonal wind profile have rather large errors.

For the gust analysis, it was assumed that the wind gust occurs in the zonal direction. In reality, wind gusts may occur in any horizontal direction, particularly near the surface. The observation geometry, which strongly favors the zonal direction, justifies neglecting the meridional component in this simulation.

All cases presented here display a few common features. We already mentioned the large residual during the first few seconds of the descent. Other features are spikes in the residuals at $t_0 + 15$ min and, in the gust cases, at the moment of the wind gust. The spike at $t_0 + 15$ min is caused by the rapidly changing descent velocity due to the exchange of parachutes. The spikes at the moment of the wind gust occurrence are caused by the rapidly changing zonal wind velocity. The rapid changes are smeared out by

the moving average filter applied to the carrier frequency measurement and thus produce relatively large residuals with respect to the input zonal wind profile.

The oscillation of the retrieved zonal wind speed, best visible in the residuals after touchdown towards the end of the mission, has a period of 4.5 min and is associated with the strong spurious line not filtered out by the moving average filter. Its amplitude is correlated to the amplitude A_{osc} shown in Fig. 6.2 and imposes an oscillation of the retrieved zonal wind speed of ± 20 cm s^{-1} at maximum.

The inclusion of spin in this analysis, for which Doppler variations of only ± 2.8 Hz are expected, has virtually no impact. We constructed simulation data assuming no spin for Huygens to investigate the impact of spin on the retrieved zonal wind speed. The result is a plot that is identical to Fig. 6.3.

This analysis shows that the DWE measurement of the Huygens carrier frequency can be used to derive an altitude profile of the zonal wind speed in Titan's atmosphere at the expected level of accuracy. The largest error sources produce a systematic error on the zonal wind retrieval. The wind shear profile is limited only by random errors, the largest being the noise associated with the frequency measurement and the error in the descent velocity.

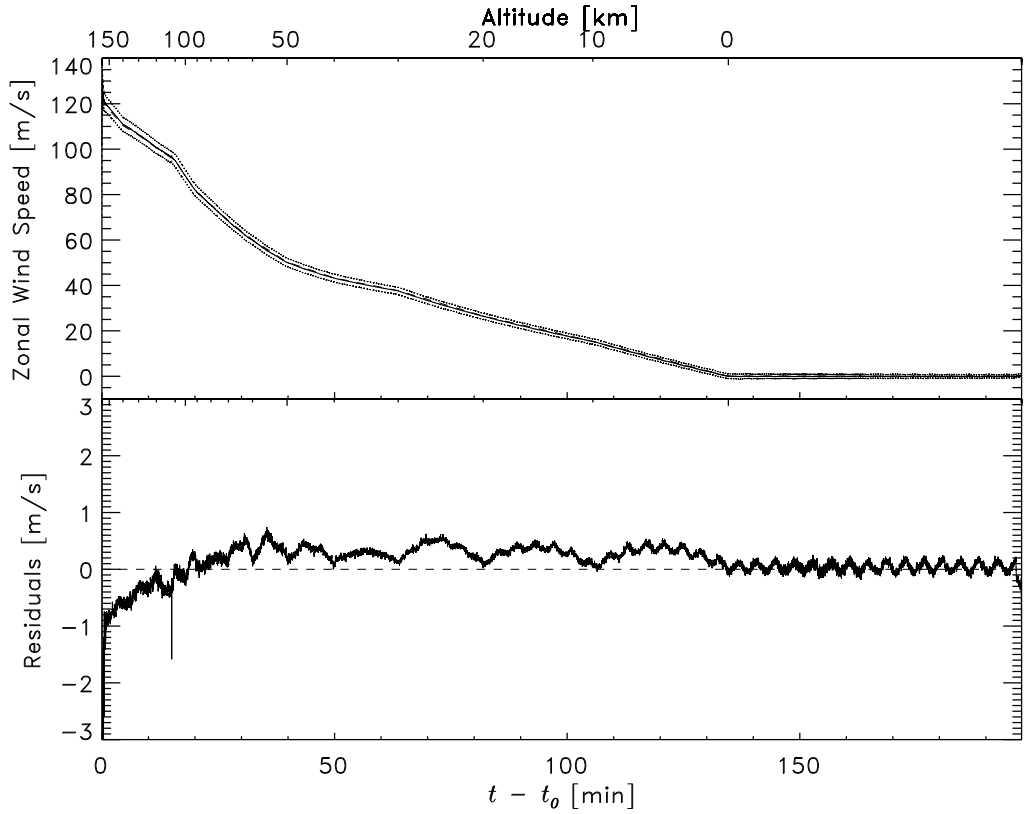

Figure 6.3: Zonal wind retrieval. Upper panel: The solid line shows the retrieved zonal wind speed. The dotted lines give the error boundaries calculated in Sec. 5.6. The dashed line shows the input wind model (virtually no difference visible at this scale). In this example, the model data were constructed using prograde Flasar wind and no meridional motion. True longitude and retrieval longitude are identical. Lower panel: Residual between input and retrieved zonal wind speed from upper panel.

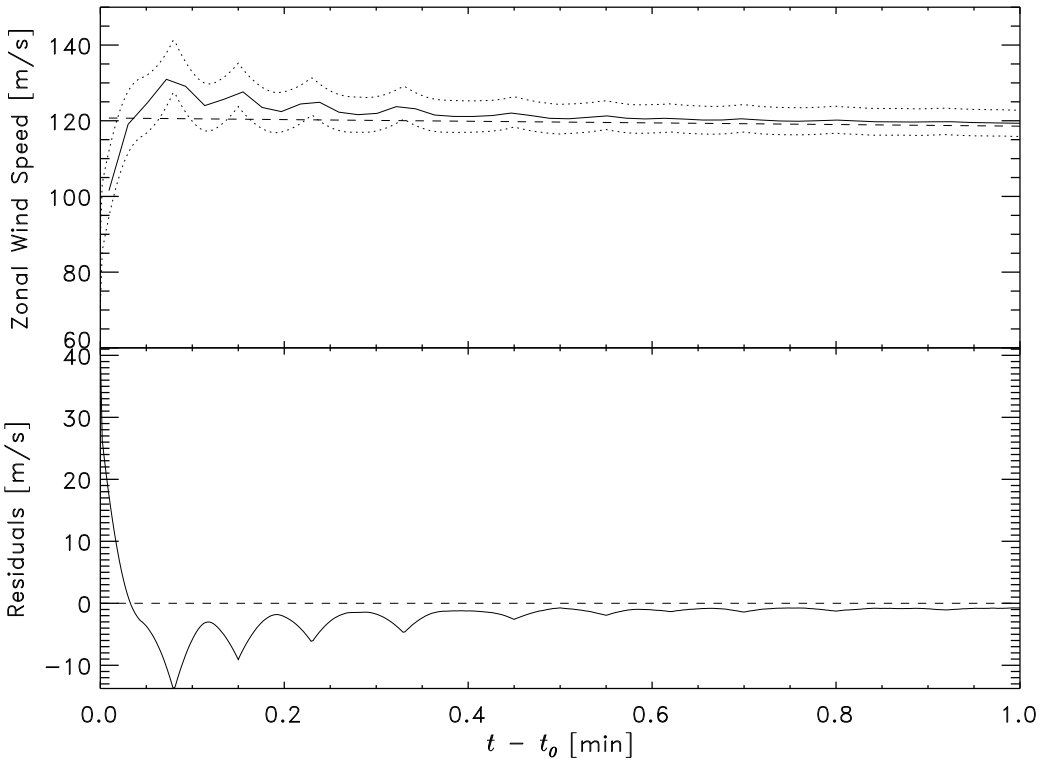

Figure 6.4: First minute of Fig. 6.3.

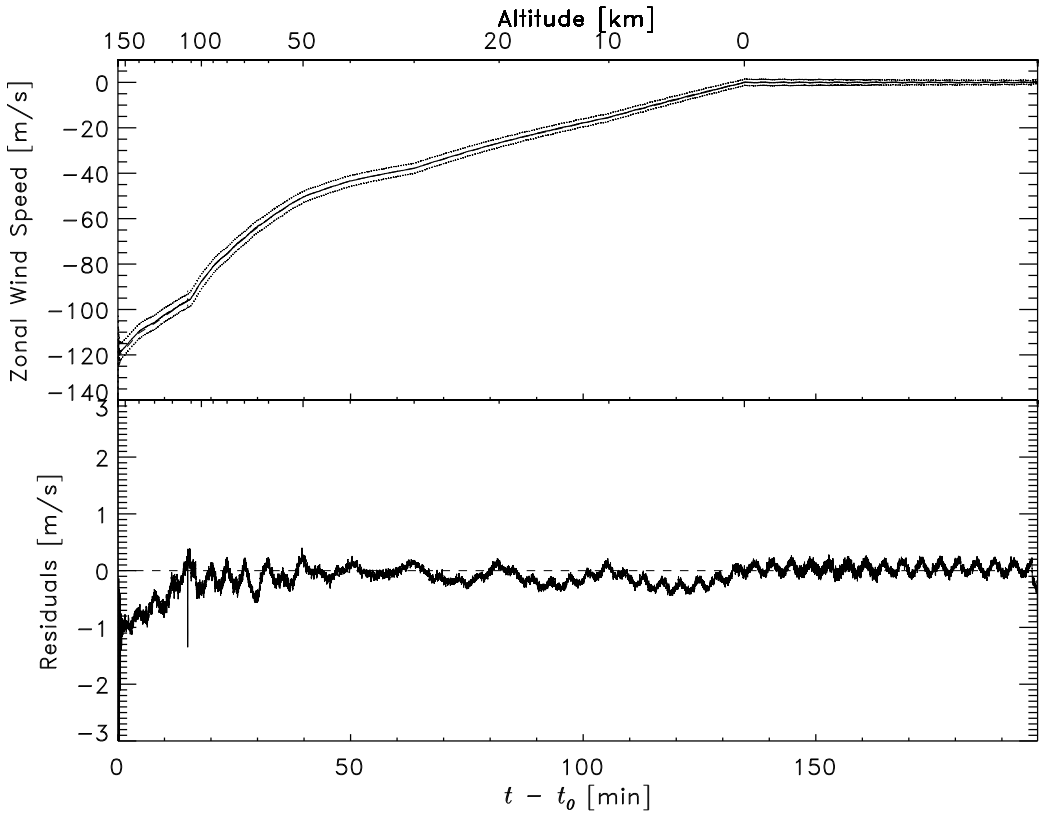

Figure 6.5: Zonal wind retrieval. Input parameters: retrograde Flasar wind, no meridional motion, true and retrieval longitude identical.

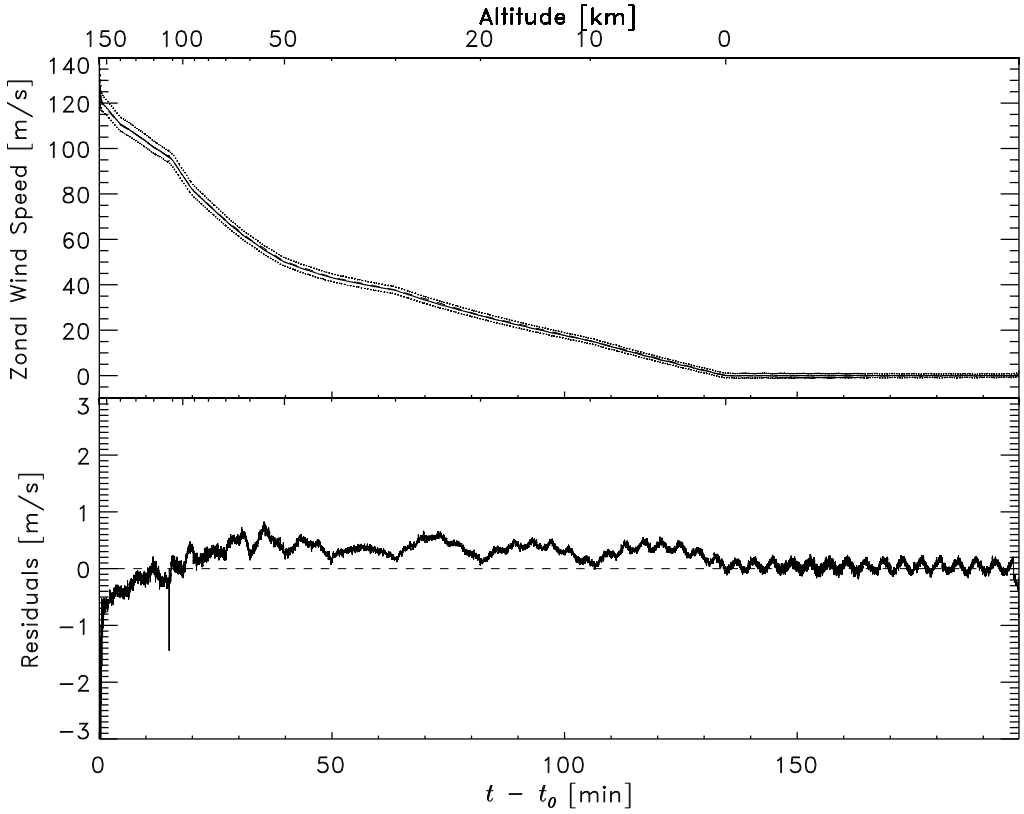

Figure 6.6: Zonal wind retrieval. Input parameters: prograde Flasar wind, meridional motion: 1 m s^{-1} towards north, true and retrieval longitude identical.

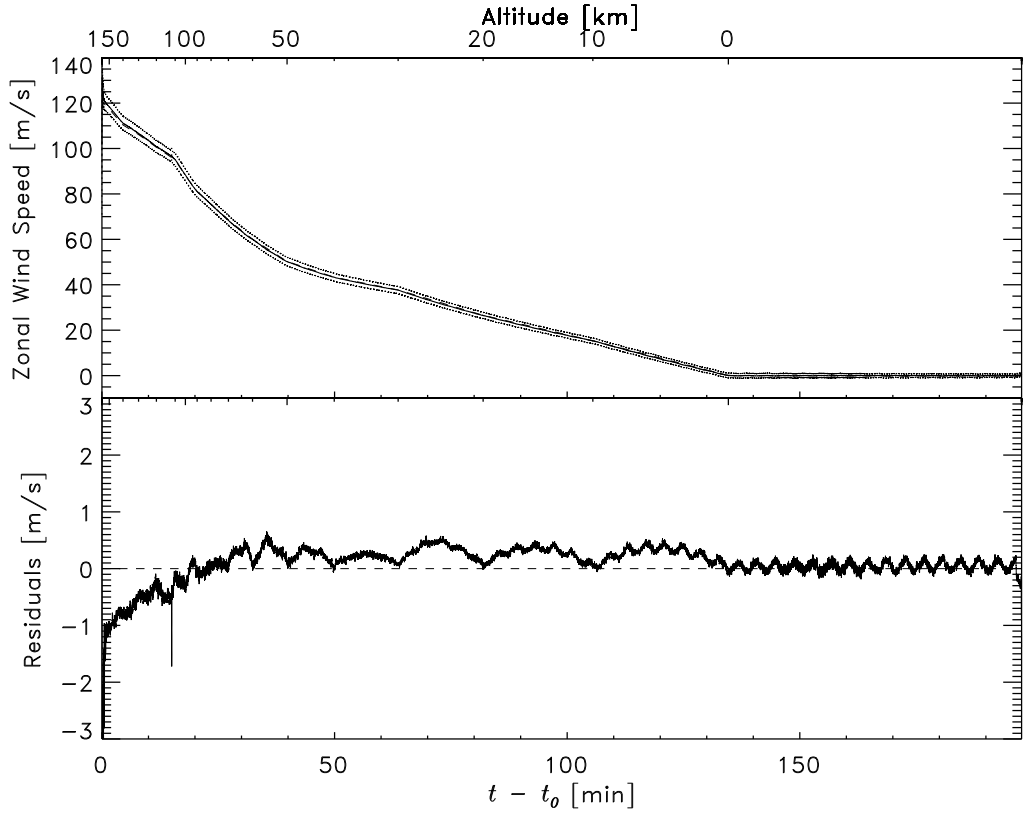

Figure 6.7: Zonal wind retrieval. Input parameters: prograde Flasar wind, meridional motion: 1 m s^{-1} towards south, true and retrieval longitude identical.

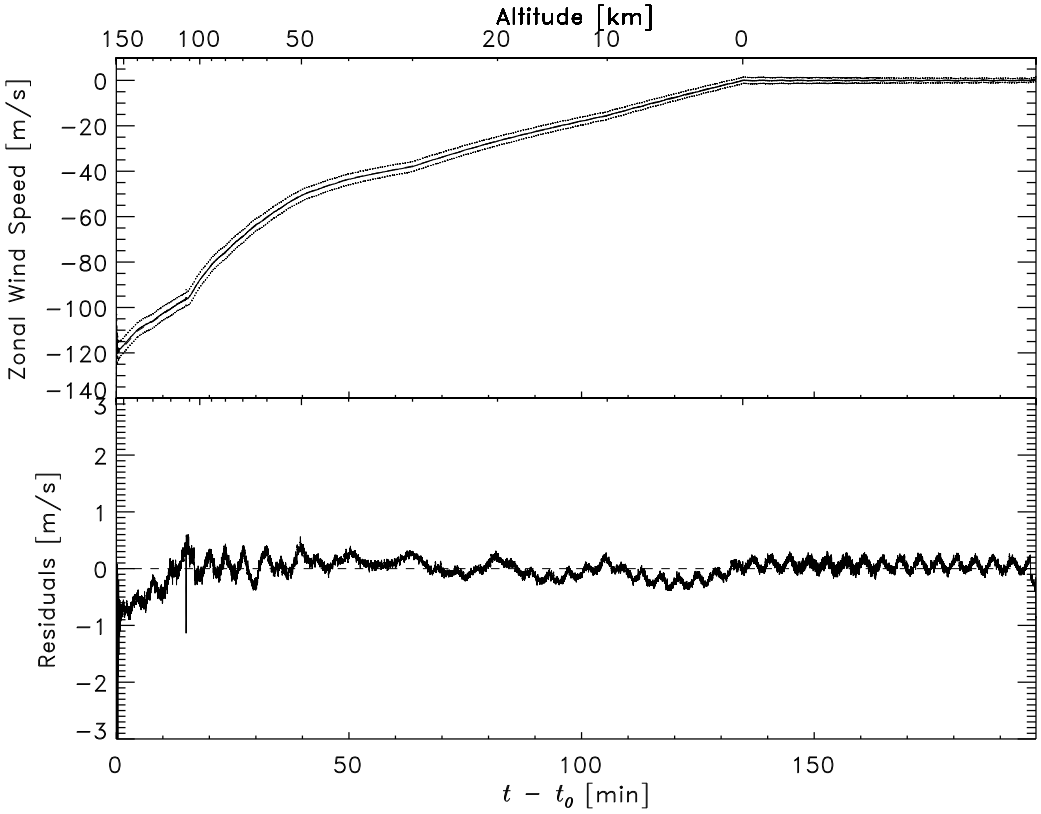

Figure 6.8: Zonal wind retrieval. Input parameters: retrograde Flasar wind, meridional motion: 1 m s^{-1} towards north, true and retrieval longitude identical.

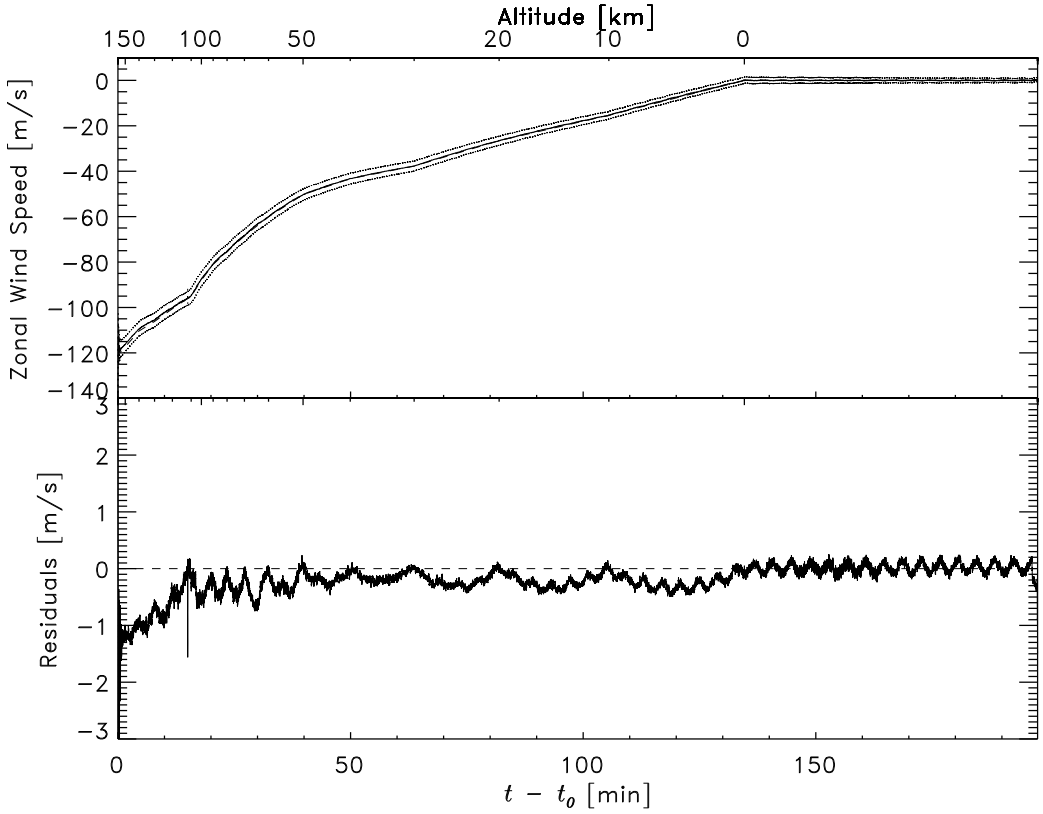

Figure 6.9: Zonal wind retrieval. Input parameters: retrograde Flasar wind, meridional motion: 1 m s^{-1} towards south, true and retrieval longitude identical.

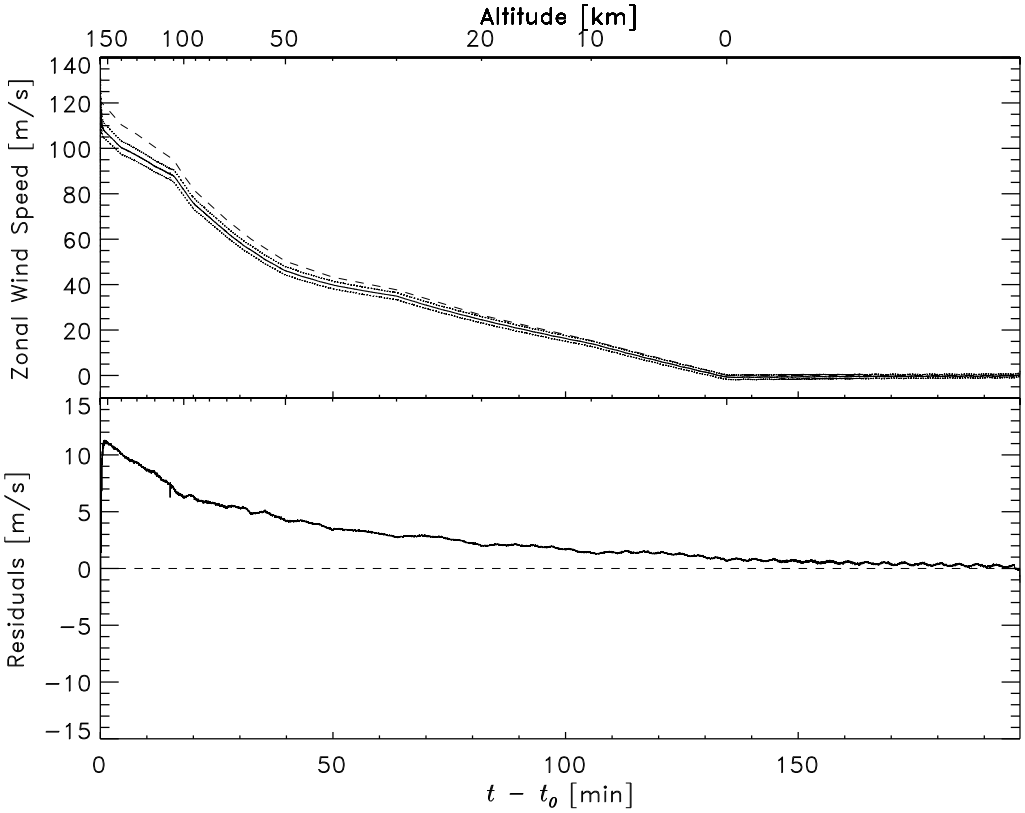

Figure 6.10: Zonal wind retrieval. Input parameters: prograde Flasar wind, no meridional motion, retrieval longitude 50 km East of true longitude (corresponding to 1.1°).

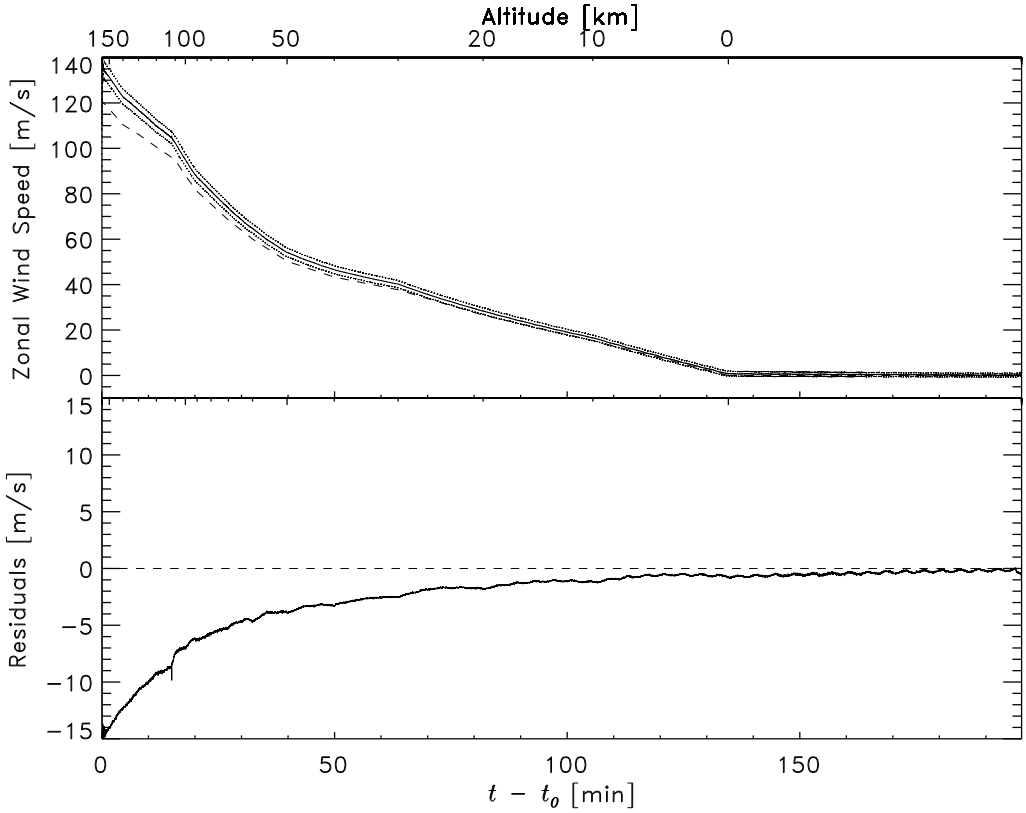

Figure 6.11: Zonal wind retrieval. Input parameters: prograde Flasar wind, no meridional motion, retrieval longitude 50 km West of true longitude (corresponding to 1.1°).

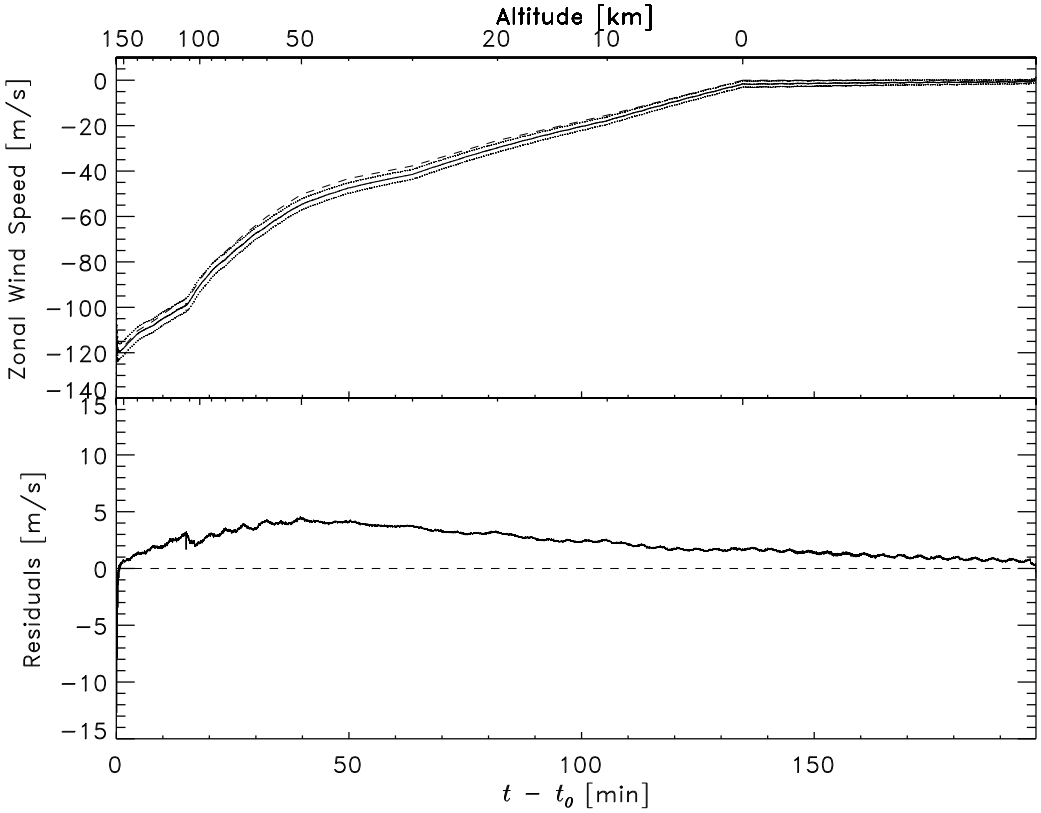

Figure 6.12: Zonal wind retrieval. Input parameters: retrograde Flasar wind, no meridional motion, retrieval longitude 50 km East of true longitude (corresponding to 1.1°).

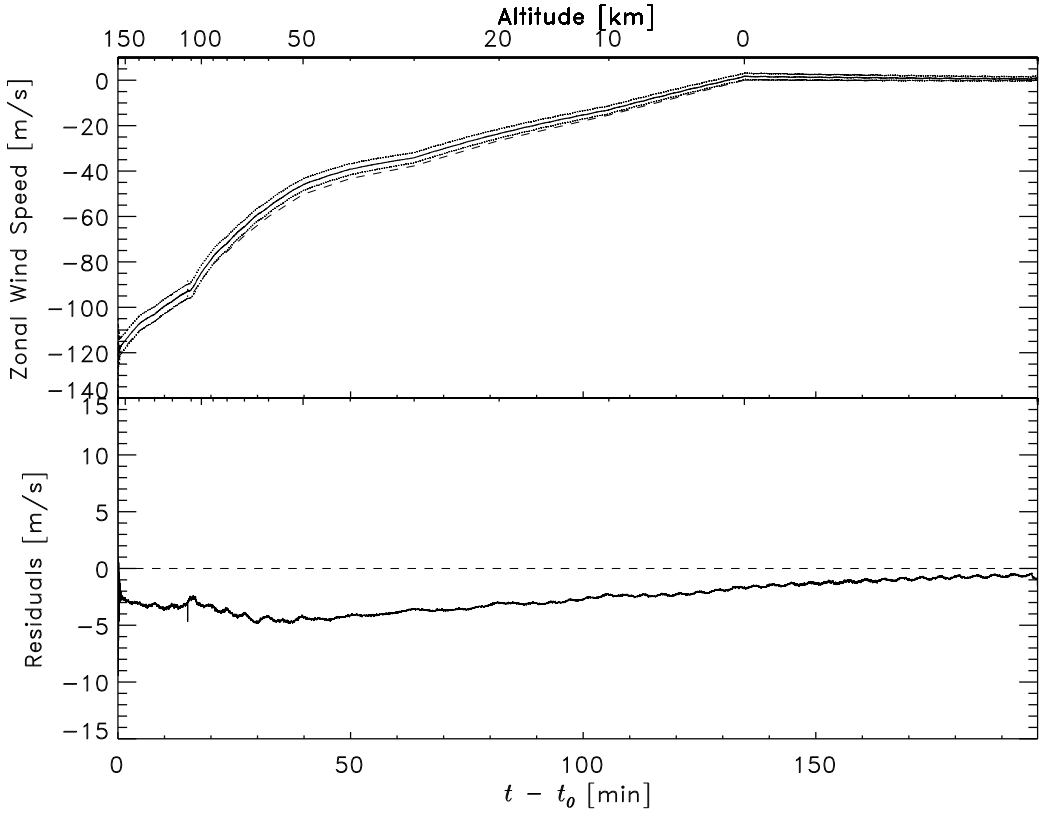

Figure 6.13: Zonal wind retrieval. Input parameters: retrograde Flasar wind, no meridional motion, retrieval longitude 50 km West of true longitude (corresponding to 1.1°).

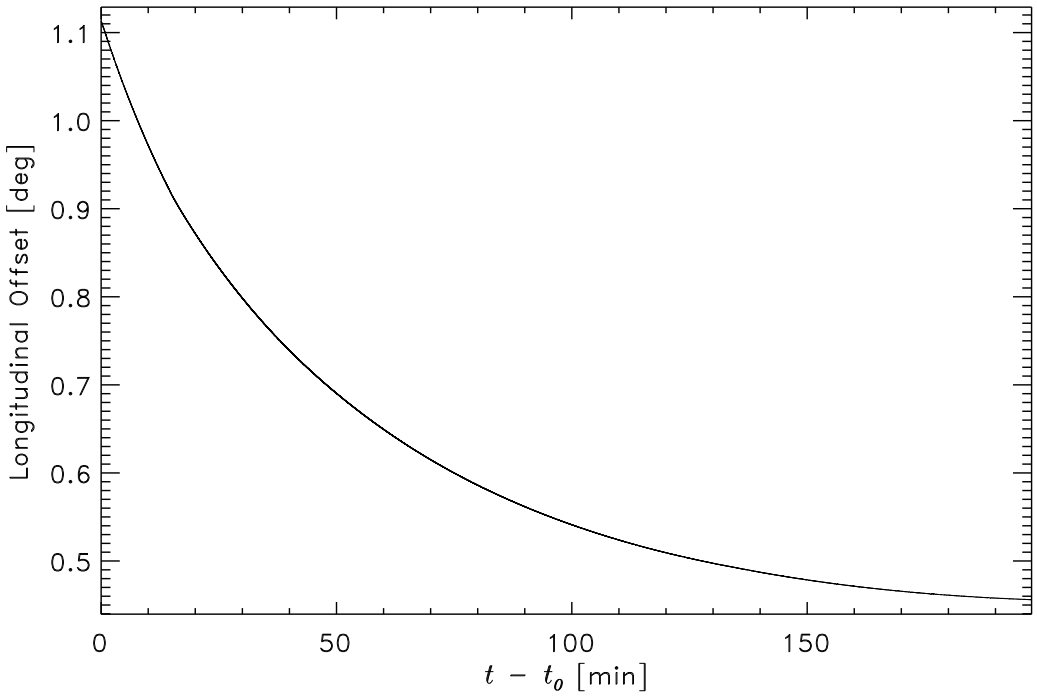

Figure 6.14: Evolution of the longitudinal position error for the case shown in Fig. 6.10.

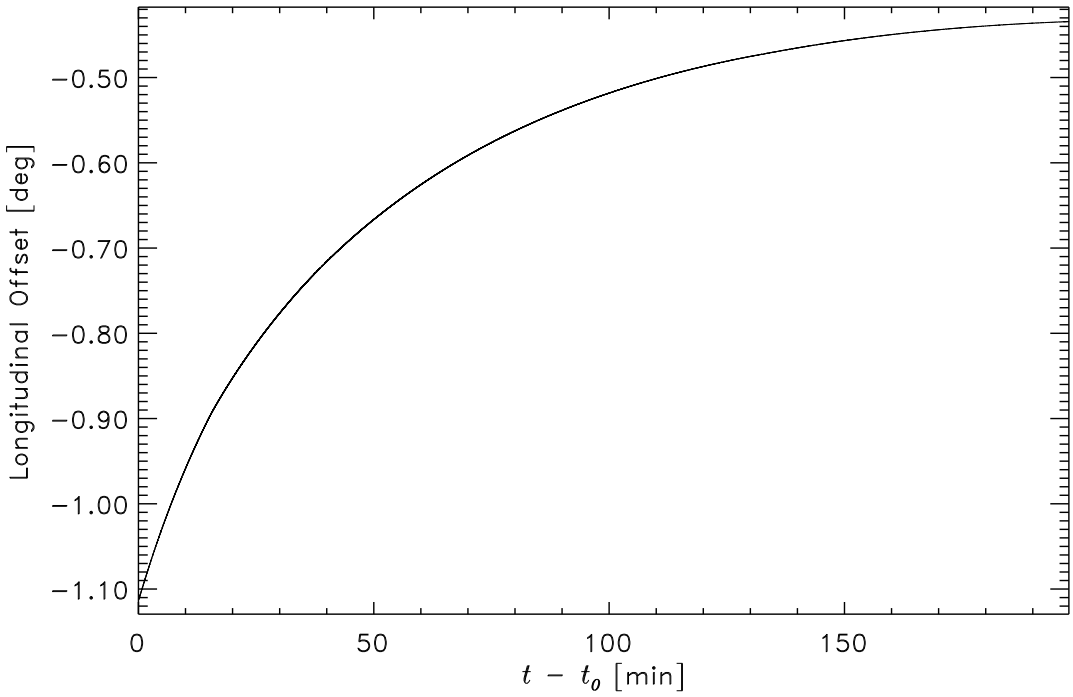

Figure 6.15: Evolution of the longitudinal position error for the case shown in Fig. 6.11.

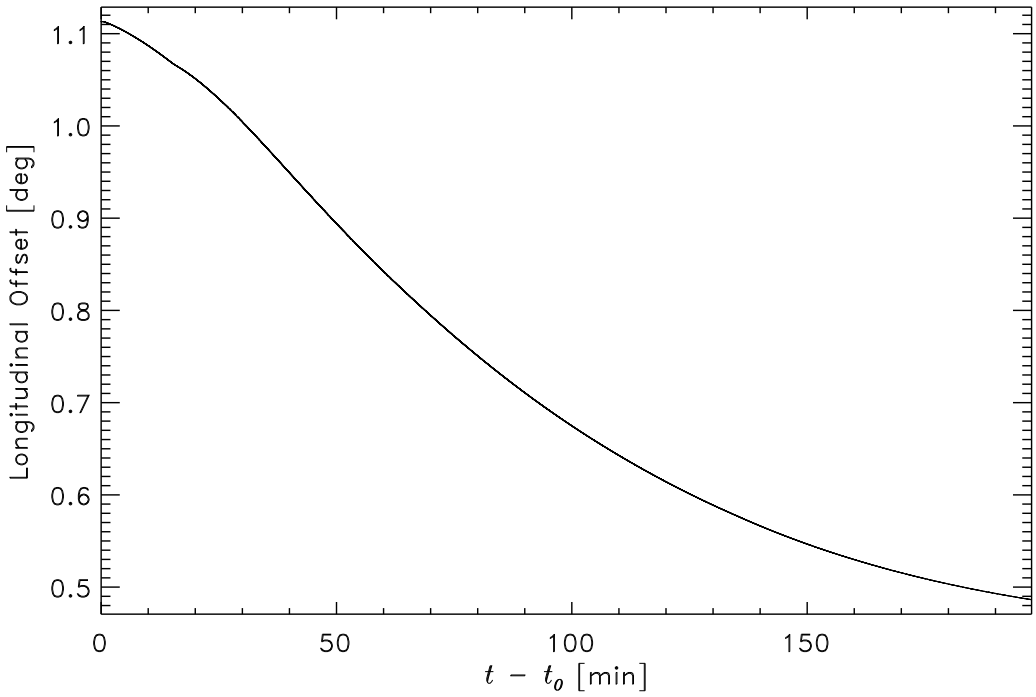

Figure 6.16: Evolution of the longitudinal position error for the case shown in Fig. 6.12.

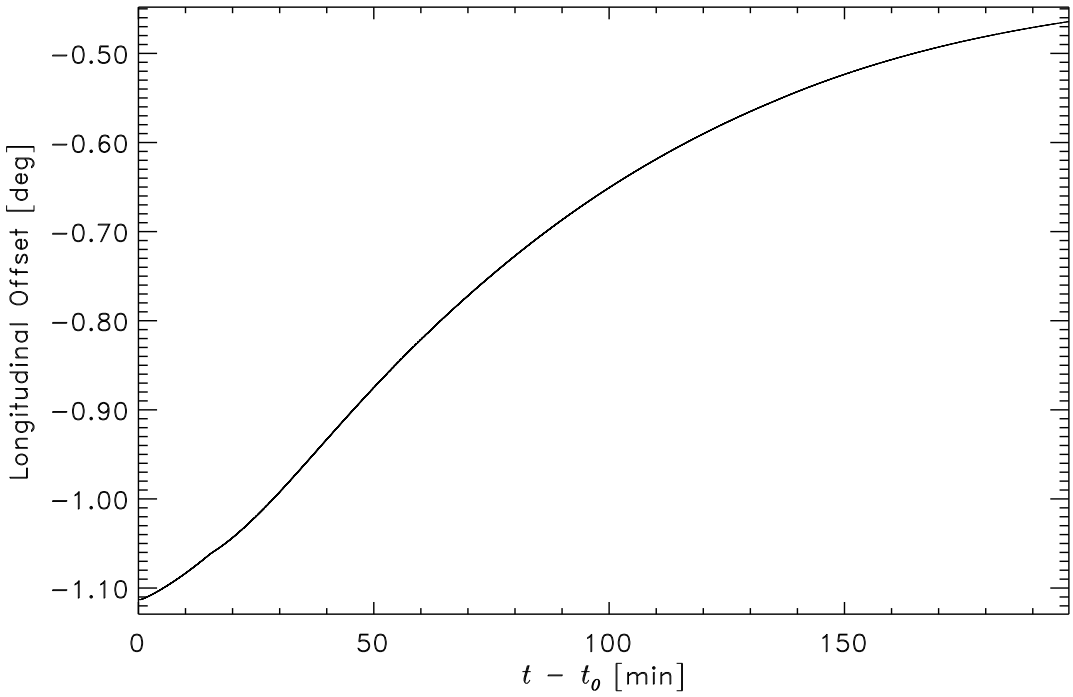

Figure 6.17: Evolution of the longitudinal position error for the case shown in Fig. 6.13.

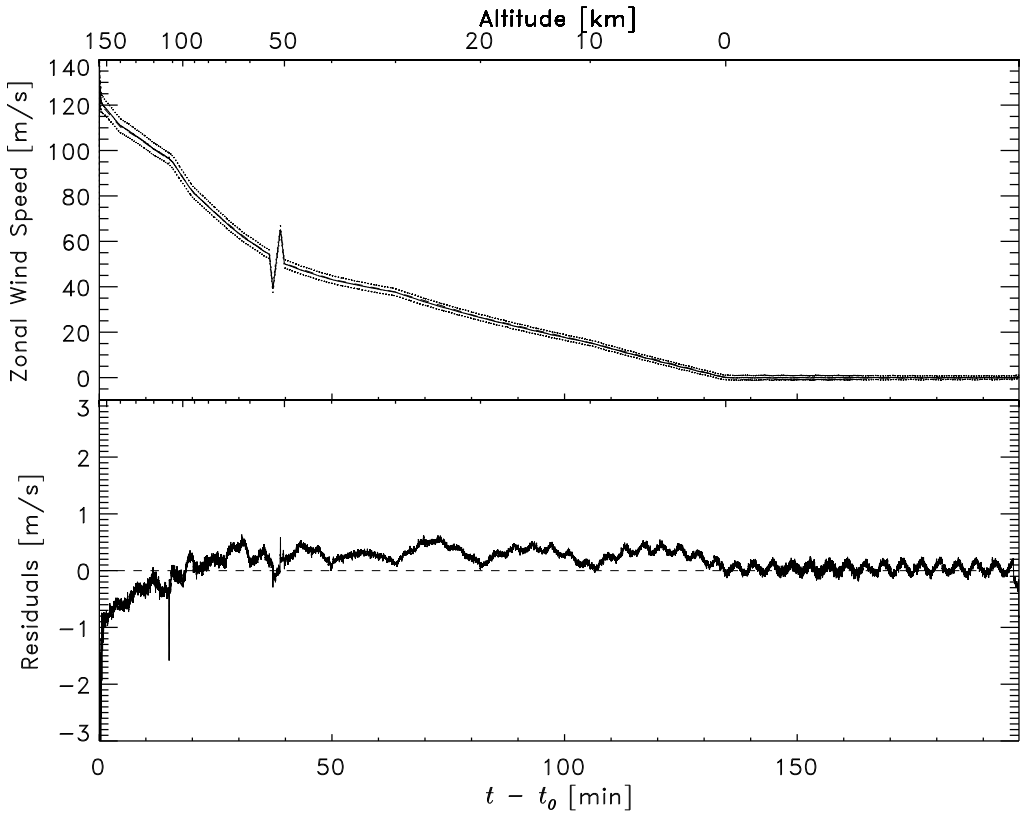

Figure 6.18: Zonal wind retrieval. Input parameters: prograde Flasar wind incl. wind gust, no meridional motion, true and retrieval longitude identical.

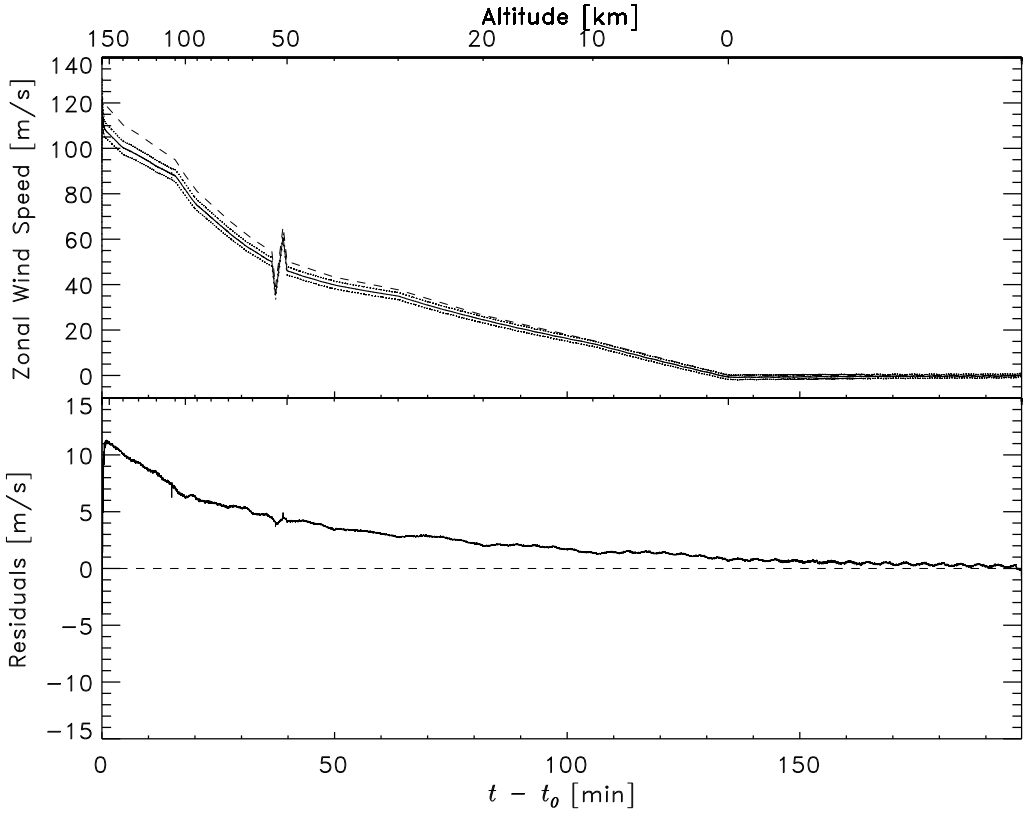

Figure 6.19: Zonal wind retrieval. Input parameters: prograde Flasar wind incl. wind gust, no meridional motion, retrieval longitude 50 km East of true longitude (corresponding to 1.1°).

Chapter 7

Summary

The feasibility of retrieving the Titan atmosphere zonal wind speed profile during the Huygens descent using the PRL carrier frequency measurement has been shown in this thesis. The use of Rubidium-based ultra-stable oscillators allows direct evaluation of the received frequency, because the absolute value of the frequency output of such oscillators is predictable under various environmental conditions.

The RUSO and TUSO performances were investigated with extensive testing during pre-launch integration and have been monitored at regular intervals in flight. Based on the test results, it is possible to characterize in detail all hardware effects on the received carrier frequency and to eliminate most them.

The impact of other Doppler contributions can be extracted using the measurements of other instruments. Those measurements are all subject to systematic and statistical errors, which affect the accuracy of the zonal wind retrieval. It was shown that the predicted accuracy of all input measurements is sufficient for an accurate zonal wind profile reconstruction.

Furthermore, it was shown that trajectory errors, particularly the position errors of Huygens, are the most dominant error source for DWE. These errors impose a systematic error that produces an offset on the absolute zonal wind retrieval. The favorable observation geometry acts to decrease the offset during the mission. This makes the algorithm presented in this thesis robust.

The wind shear profile, on the other hand, is not affected by systematic errors but only by relatively small random errors, i.e. the noise of the carrier frequency measurement. Wind gusts of the order of meters per second can thus be resolved, even if the retrieved absolute zonal wind speed is in error by several m s^{-1}, e.g. due to the use of an erroneous initial Huygens longitude.

DWE can thus contribute to the scientific exploitation of the Huygens mission by providing valuable data for the investigation of the atmospheric

dynamics of slowly rotating planetary bodies. Furthermore, the data are an important input for the Huygens trajectory reconstruction process.

Appendix

Construction of Model Data

The carrier frequency and signal level data are part of the PSA-HK data which are sampled at 8 Hz. DWE also checks various PRL status parameters of the PSA-HK data indicating the link quality. Furthermore, information about power consumption, internal temperatures and lock status are provided as part of the PSA-HK data for the RUSO and as part of the Probe-HK data for the TUSO. Detailed information about the TM format can be found in the TM/TC data tables (Alcatel, 1997c). The source code of the C-programs used to retrieve those measurements and PRL parameters from the PSA- and Probe-HK data stream can be found at the DWE homepage http://www.astro.uni-bonn.de/~dwe/. Several programs for the graphical display of the data, written in Interactive Data Language (IDL), are also included.

The velocity contributions and simulated data (Section 5.6 and Chapter 6) were constructed using JPL Navigation predictions for the Cassini trajectory and the Titan ephemeris. These data are provided as binary kernels which can be evaluated using the public toolkit SPICE. The kernels can be retrieved from an internal Cassini web page, the SPICE toolkit is available from the public FTP server ftp://naif.jpl.nasa.gov/pub/naif/toolkit/ via anonymous FTP. The SPICE toolkit provides functions for programs written in C or Fortran, respectively, which evaluate the SPICE kernels and derive the state vectors of Cassini with respect to Titan. SPICE can define the state vectors with respect to all common celestial coordinate systems. The IAU-Titan system is used predominantly in this thesis.

The predicted altitude and descent velocity of Huygens during the Huygens mission are taken from a model developed by Alcatel and provided by ESA as plain text files via anonymous FTP at the ESTEC public FTP server ftp://ftp.estec.esa.nl/pub/huygens/profile_oct95/. It must be noted, however, that this profile refers to the old mission scenario. Thus, any geometric information such as Titan latitude, longitude or angles are invalid. A

new descent profile is currently under construction (as of spring 2002).

The actual construction of the model data also depends on the Huygens position at the start of the data transmission and on the time synchronization between Huygens and Cassini state vectors. As outlined in Section 5.6, we used 161.4°E and 9.0°S for the Huygens position at t_0, which was set to 09:11:10.8 UTC on 14 January 2005. These settings will certainly be slightly different in the real mission, but their actual values are not crucial for the algorithm presented here.

The following table summerizes the construction of the parameters entering Eq. (5.16):

v_C	taken from SPICE kernels, including the Titan rotation velocity v_{rot}, if calculated with respect to IAU-Titan
v_{des}	taken from Alcatel/ESA model
v_{EW}	the applied zonal wind speed
v_{NS}	the applied meridional wind speed
v_{rot}	either 0 or equal to the Titan rotation velocity at the Huygens position, depending on the applied coordinate system
γ_{DWC}	angle between LOS and zonal direction, calculated from the scalar product between the LOS vector and a unit vector pointing towards East at the Huygens position
γ_{NS}	angle between LOS and meridional direction, calculated from the scalar product between the LOS vector and a unit vector pointing towards South at the Huygens position
γ_{des}	angle between LOS and downward direction, calculated from the scalar product between the LOS vector and a unit vector pointing down at the Huygens position
γ_C	angle between LOS and the Cassini velocity, calculated from the scalar product between the LOS vector and the Cassini velocity vector

The C-programs for the construction of the model data and the simulated mission data and the IDL-programs used for their graphical display in this thesis can be found at the DWE homepage http://www.astro.uni-bonn.de/~dwe/.

Acronym List

ACP	Aerosol Collector and Pyrolyzer
AGC	Automatic Gain Control
AIV	Assembly, Integration and Verification
BIU	Bus Interface Unit
CDS	Command and Data Management Subsystem (Cassini)
DISR	Descent Imager and Spectrometer
DSN	Deep Space Network
DTWG	Descent Trajectory Working Group
DWC	Doppler Wind Component
DWE	Doppler Wind Experiment
EM	Engineering Model
ESA	European Space Agency
FM	Flight Model
FWHM	Full Width at Half Maximum
GCM	General Circulation Model
GCMS	Gas Chromatograph and Mass Spectrometer
HASI	Huygens Atmospheric Structure Instrument
HGA	High Gain Antenna
HK	Housekeeping
HPA	High Power Amplifier
HUM	Huygens User Manual
IAU	International Astronomical Union
IR	Infrared
JPL	Jet Propulsion Laboratory
LH	Lellouch-Hunten (atmospheric model)
LHCP	Left Hand Circular Polarization
LOS	Line of Sight
NASA	National Aeronautics and Space Administration
ODM	Orbiter Deflection Maneuver
ODT	Orbiter Delay Time
PAA	Probe Aspect Angle
PCO	Probe Checkout
PLL	Phase Locked Loop
PRL	Probe Relay Link
PRT	Probe Relay Test
p-p	Peak-to-Peak
PSA	Probe Support Avionics
PSE	Probe Support Equipment
PTA	Probe Transmitting Antenna

QFS	Qualification and Flight Spare Model
RAU	Radar Altimeter Unit
Rb	Rubidium
RHCP	Right Hand Circular Polarization
RSS	Root Sum of Squares
RUSO	Receiver Ultra-Stable Oscillator
SOI	Saturn Orbit Insertion
SPICE	Spacecraft, Planet, Instrument, C-Matrix, Events
SSP	Surface Science Package
TM/TC	Telemetry / Telecommand
TUSO	Transmitter Ultra-Stable Oscillator
USO	Ultra-Stable Oscillator

Acknowledgments

At this point, I like to express my gratitude to those who supported me in writing this thesis. At the first place is, of course, the Huygens-DWE-PI Dr. Mike Bird. Thank you, Mike, for the opportunity to write this thesis and for the numerous discussions and comments. I also want to thank Profs. Dr. Max Römer and Dr. Ulrich Mebold for their willingness to act as examiners of this thesis. Without mentioning individual names, I want to thank all my colleagues at the Astronomical Institutes of the University of Bonn as well as my DWE and Huygens colleagues all around the globe for the pleasant working atmosphere and some useful discussions. Last not least, I like to mention my wife Monika for her continuous mental support.

References

Alcatel: Huygens User Manual, HUY.AS/c.100.OP.0201, Huygens Project Internal Document, 1997a

Alcatel: HUY.AS/c.100.RE.0505, Huygens Project Internal Document, 1997b

Alcatel: TM/TC Data Tables, HUY.AS/c.100.DB.0204 Huygens Project Internal Document, 1997c

Allan, D.W.; Ashby, N.; Hodge, C.C.: Science of Timekeeping, Hewlett Packard Application Note #1289 http://www.allanstime.com/Publications/DWA/Science_Timekeeping/, 1997

Allison, M.: A Preliminary Assessment of the Titan Planetary Boundary Layer, in *Proc. Symposium on Titan, Toulouse, 9-12 September 1991*, ESA-SP-338, 113, 1992

Atkinson, D.H.: Measurement of Planetary Wind Fields by Doppler Monitoring of an Atmospheric Entry Vehicle, Ph.D. Thesis, Washington State University, Pullman WA/USA, 1989

Atkinson, D.H.: Report of the Huygens Descent Trajectory Working Group, ESA, Huygens Project Internal Document, 1998

Awal, M.; Lunine J.L.: Moist Convective Clouds in Titan's Atmosphere, *Geophys. Res. Lett.* **21**, 2491, 1994

Bird, M.K.: Atmospheric Attenuation of the Huygens S-band Radio Signal during the Titan Descent, in *HUYGENS - Science, Payload and Mission*, ESA-SP-1177, 321, 1997

Bird, M.K.; Heyl, M.; Allison, M.; Asmar, S.W.; Atkinson, D.H.; Edenhofer, P.; Plettemeier, D.; Wohlmut, R.; Iess, L.; Tyler, G.L.: The Huygens Doppler Wind Experiment, in *HUYGENS - Science, Payload and Mission*, ESA-SP-1177, 139, 1997a

Bird, M.K.; Allison, M.; Asmar, S.W.; Atkinson, D.H.; Dutta-Roy, R.; Edenhofer, P.; Folkner, W.M.; Heyl, M.; Iess, L.; Plettemeier, D.; Preston, R.A.; Tyler, G.L.; Wohlmut, R.: Rubidium Ultra-Stable Oscillators at Titan: The Huygens Doppler Wind Experiment, in *Proc. Workshop on the Scientific Applications of Clocks in Space*, 211, 1997b

Bird, M.K.; Dutta-Roy, R.; Asmar, S.W.; Rebold, T.A.: Detection of Titan's Ionosphere from Voyager 1 Radio Occultation Observations, *Icarus* **130**, 426, 1997c

Bird, M.K.; Dutta-Roy, R.; Asmar, S.W.; Rebold, T.A.: Radio Occultation Detection of Titan's Ionosphere, *BAAS* **30**, 1093, 1998

Bird, M.K.; Allison, M.; Asmar, S.W.; Atkinson, D.H.; Dutta-Roy, R.; Edenhofer, P.; Folkner, W.M.; Heyl, M.; Iess, L.; Plettemeier, D.; Preston, R.A.; Tyler, G.L.; Wohlmut, R.: The Huygens Doppler Wind Experiment: Titan Winds Derived from Probe Radio Frequency Measurements, *Space Science Rev.*, in press, 2002

Clausen, K.; Deutsch, L.: Huygens Recovery Task Force (HRTF) Final Report, HUY-RP-12241, Huygens Project Internal Document, 2001

Comas Solá, J.: Observations des satellites principaux de Jupiter et de Titan, *Astronomische Nachrichten* **179**, 290, 1908

Conner, D.: Cassini SPICE Development Team Report and Implementation Plan, Cassini Project Internal Document, 1999

Counselman, C.C. III; Gourevitch, S.A.; King, R.W.; Pettengill, G.H.; Prinn, R.G.; Shapiro, I.I.; Miller, R.B.; Smith, J.R.; Ramos, R.; Liebrecht, P.: Wind Velocities on Venus: Vector Determination by Radio Interferometry, *Science* **203**, 805, 1979

Courtin, R.; Gautier, D.; McKay, C.P.: Titan's Thermal Emission Spectrum: Reanalysis of the Voyager Infrared Measurements, *Icarus* **114**, 144, 1995

Coustenis, A. and Taylor, F.: Titan – The Earth-Like Moon, in *Series on Atmospheric, Oceanic and Planetary Sciences – Vol. 1*, World Scientific Publishing Co. Ltd., 1999

DASA: Acceptance Data Package and Experiment User Manual for RUSO FM/TUSO QFS, DWE-DASA.-1000-RP-0006/08, Huygens Project Internal Document, 1996

Davies, M.E.; Abalakin, V.K.; Bursa, M.; Lieske, J.H.; Morando, B.; Morrison, D.; Seidelmann, P.K.; Sinclair, A.T.; Yallop, B.; Tjuflin, Y.S.: Report of the IAU/IAG/COSPAR Working Group on Cartographic Coordinates and Rotational Elements of the Planets and Satellites: 1994, *Celestial Mechanics and Dynamical Astronomy* **63**, 127, 1996

Del Genio, A.D.; Zhou, W.; Eichler, T.P.: Equatorial Superrotation in a Slowly Rotating GCM: Implications for Titan and Venus, *Icarus* **101**, 1, 1993

Dutta-Roy, R.: Oscillations of NCO and AGC, DWE-Report to the Huygens Project, 1997

Dutta-Roy, R.: Report on DWE Spurious Oscillation, DWE-Report to the Huygens Project, 1998

Dutta-Roy, R.: DWE Test Reports for AIV and In-Flight Checkouts, DWE-Reports to the Huygens Project, 1996-2002

Fjeldbo, G; Eshleman, V.R.: The Bistatic Radar-Occultation Method for the Study of Planetary Atmospheres, *J. Geophys. Res.* **70**, 3217, 1965a

Fjeldbo, G; Eshleman, V.R.; Garriott, O.K.; Smith, F.L. III: The Two-Frequency Bistatic Radar-Occultation Method for the Study of Planetary Atmospheres, *J. Geophys. Res.* **70**, 3701, 1965b

Flasar, F.M. and Conrath, B.J.: The Meteorology of Titan, in *Proc. Symposium on Titan, Toulouse, 9-12 September 1991*, ESA-SP-338, 89, 1992

Flasar, F.M.; Allison, M.D.; Lunine, J.I.: Titan Zonal Wind Model, in *HUYGENS - Science, Payload and Mission*, ESA-SP-1177, 287, 1997

Flasar, F.M.: The Dynamic Meteorology of Titan, *Planet. Space Sci.* **46**, 1125, 1998

Fulchignoni, M.; Angrilli, F.; Bianchini, G.; Bar-Nun, A.; Barucci, M.A.; Borucki, W.; Coradini, M.; Coustenis, A.; Ferri. F.; Grard, R.J.; Hamelin, M.; Harri, A.M.; Leppelmeier, G.W.; Lopez-Moreno, J.J.; McDonnel, J.A.M.; McKay, C.; Neubauer, F.M.; Pedersen, A.; Picardi, G.; Pirronello, V.; Pirjola, R.; Rodrigo, R.; Schwingenschuh, C.; Seiff, A.; Svedham, H.; Thrane, E.; Vanzani, V.; Visconti, G.; Zarnecki, J.: The Huygens Atmospheric Structure Instrument (HASI), in *HUYGENS - Science, Payload and Mission*, ESA-SP-1177, 163, 1997

Grard, R.J.L.: The Significance of Meteoric Ionization for the Propagation of Lightning Spherics in the Atmosphere of Titan, in *Proc. Symposium on Titan, Toulouse, 9-12 September 1991*, ESA-SP-338, 113, 1992

Hinson, D.P.; Tyler, G.L.: Internal Gravity Waves in Titan's Atmosphere Observed by Voyager Radio Occultation, *Icarus* **54**, 337, 1983

Hourdin, F.; Talagrand, O.; Sadourny, R.; Courtin, R.; Gautier, D.; McKay, C.P.: Numerical Simulation of the General Circulation of the Atmosphere of Titan, *Icarus* **117**, 358, 1995

Hubbard, W.B.; Sicardy, B.; Miles, R.; Hollis, A.J.; Forrest, R.W.; Nicolson, I.K.M.; Appleby, G.; Beisker, W.; Bittner, C.; Bode, H.-J., Bruns, M.; Denzau, H.; Nezel, M.; Riedel, E.; Struckmann, H.; Arlot, J.E.; Roques, F.; Sèvre, F.; Thuillot, W.; Hoffmann, M.; Geyer, E.H.; Buil, C.; Colas, F.; Lecacheux, J.; Klotz, A.; Thouvenot, E.; Vidal, J.L.; Carreira, E.; Rossi, F.; Blanco, C.; Cristaldi, S.; Nevo, Y.; Reitsema, H.J.; Brosch, N.; Cernis, K.; Zdanavicius, K.; Wasserman, L.H.; Hunten, D.M.; Gautier, D.; Lellouch, E.; Yelle, R.V.; Rizk, B.; Flasar, F.M.; Porco, C.C.; Toublanc, D.; Corugedo, G.: The Occultation of 28 Sgr by Titan, *Astron. Astrophys.* **269**, 541, 1993

Ip, W.-H.: Titan's Upper Ionosphere, *Astrophys. J.* **362**, 354, 1990

Israel, G.; Niemann, H.; Raulin, F.; Riedler, W.; Atreya, S.; Bauer, S.;

Cabane, M.; Chassefière, E.; Hauchecorne, A.; Owen, T.; Sablé, C.; Samuelson, R.; Torre, J.P.; Vidal-Madjar, C.; Brun, J.F.; Coscia, D.; Ly, R.; Tintignac, M.; Steller, M.; Gelas, C.; Condé, E.; Millan, P.: The Aerosol Collector Pyrolyzer (ACP) Experiment for Huygens, in *HUYGENS - Science, Payload and Mission*, ESA-SP-1177, 59, 1997

Jones, J. (JPL Navigation Team): private communication, 2000

Jones, J.C.; Giovagnoli, F.: The Huygens Probe System Design, in *HUYGENS - Science, Payload and Mission*, ESA-SP-1177, 25, 1997

Kazeminejad, Bobby (ESA): private communication, 2001

Keller, C.N.; Cravens, T.E.; Gan, L.: A Model of the Ionosphere of Titan, *J. Geophys. Res.* **97**, 12117, 1992

Kohl, R. and Bird, M.K.: Rubidium Standard Goes to Deep Space, in *Proc. 11th European Frequency and Time Forum*, EFTF Secretariat, Neuchatel, Switzerland, 596, 1997

Kohl, R.; Wagner, K.; Bird, M.K. and Dutta-Roy, R.: Doppler Wind Experiment – First Results From Space, in *Proc. 12th European Frequency and Time Forum*, EFTF Secretariat, Neuchatel, Switzerland, 695, 1998a

Kohl, R.; Wagner, K.; Bird, M.K. and Dutta-Roy, R.: Rubidium Frequency Standard For Deep Space Missions, Poster for the *1st ESA Workshop on Tracking, Telemetry and Command Systems*, ESTEC, 1998b

Kostiuk, T.; Fast, K.E.; Livengood, T.A.; Hewagama, T.; Goldstein, J.J.; Espenak, F.; Buhl, D.: Direct Measurement of Winds on Titan, *Geophys. Res. Lett.* **28**, 2361, 2001

Kuiper, G.: Titan - A Satellite with an Atmosphere, *Astrophys. J.* **100**, 378, 1944

Lellouch E. and Hunten, D.M.: Titan Atmosphere Engineering Model, Space Science Department of ESA, ESTEC Report, ESLAB 87/109, 1987

Lellouch E. and Hunten, D.M.: The Lellouch-Hunten Models for Titan's Atmosphere, in *HUYGENS - Science, Payload and Mission*, ESA-SP-1177, 237, 1997

Lemmon, M.T.; Karkoschka, E.; Tomasko, M.: Titan's Rotational Light-Curve, *Icarus* **113**, 27, 1995

Lindal, G.F.; Wood, G.E.; Hotz, H.B.; Sweetnam, D.N.; Eshleman, V.R.; Tyler, G.L.: The Atmosphere of Titan: An Analysis of the Voyager 1 Radio-Occultation Measurements, *Icarus* **53**, 348, 1983

Lorenz, R.D.: Descent and Impact Dynamics of the Huygens Probe, IAF-94-A.1.004, Paper presented at the 45th Congress of the International Astronautical Federation, Jerusalem, Israel, October 9-14, 1994

Lunine, J.I.; Flasar, F.M.; Allison, M.: Huygens Probe Wind Drift: Science Issues and Recommendations, Huygens Project Internal Document, 1991

Muhleman, D.O.; Grossman, A.W.; Butler, B.J.; Slade, M.A.: Radar Reflectivity of Titan, *Science* **248**, 975, 1990

Newell, A.C.; Baird, R.C.: Absolute Determination of Refractive Indices of Gases at 47.7 GHz, *J. Appl. Phys.* **36**, 3751, 1965

Niemann, H.; Atreya, S.; Bauer, S.J.; Biemann, K.; Block, B.; Carignan, G.; Donahue, T.; Frost, L.; Gautier, D.; Harpold, D.; Hunten, D.; Israel, G.; Lunine, J.; Mauersberger, K.; Owen, T.; Raulin, F.; Richards, J.; Way, S.: The Gas Chromatograph Spectrometer Aboard Huygens, in *HUYGENS - Science, Payload and Mission*, ESA-SP-1177, 85, 1997

Press, W.H.; Teukolsky, S.A.; Vetterling, W.T. and Flannery, B.P.: Numerical Recipes in C, The Art of Scientific Computing, *Cambridge University Press*, New York, 1992

Richardson, J.E.; Lorenz, R.D.; McEwan, A.: Titan's Surface and Rotation: New Results from Voyager 1 Images, *BAAS* **33**, 3811, 2001

Seiff, A.: Mars Atmospheric Winds Indicated by Motion of the Viking Landers During Parachute Descent, *J. Geophys. Res.* **98**, 7461, 1993

Smith, P.H.; Lemmon, M.T.; Lorenz, R.D.; Sromovsky, L.A.; Caldwell, J.J.; Allison, M.D.: Titan's Surface Revealed by HST Imaging, *Icarus* **119**, 336, 1996

Smith, Steven W.: The Scientist and Engineer's Guide to Digital Signal Processing, *California Technical Publishing*, San Diego, California, 1997

Sollazzo, C. (Custodian): Cassini/Huygens Integrated Data Link Report, ESA-JPL-HUY-25999, Huygens Project Internal Document, 1997

Spilker, Linda J. (Ed.): The Cassini-Huygens Mission to Saturn and Titan, NASA SP-533, NASA, Washington D.C., 1997

Svedham, H. (ESA): private communication, 2000

Tokano, T.; Neubauer, F.M.; Laube, M.; McKay, C.P.: Seasonal Variation of Titan's Atmospheric Structure Simulated by a General Circulation Model, *Planet. Space Sci.* **47**, 493, 1999

Tokano, T.: Simulation of Titan's Atmosphere by a General Circulation Model, Ph.D. Thesis, Universität Köln, 2000

Tomasko, M.G.; Doose, L.R.; Smith, P.H.; West, R.A.; Soderblom, L.A.; Combes, M.; Bézard, B.; Coustenis, A.; deBergh, C.; Lellouch, E.; Rosenqvist, J.; Saint-Pé, O.; Schmitt, B.; Keller, H.U.; Thomas, N.; Gliem, F.: The Descent Imager/Spectral Radiometer (DISR) Aboard Huygens, in *HUYGENS - Science, Payload and Mission*, ESA-SP-1177, 109, 1997

Tracadas, P.W.; Hammel, H.B.; Elliot, J.L.; Olkin, C.B.: Probing Titan's Atmosphere with the 1995 August Stellar Occultation, *Icarus* **153**, 285, 2001

Yelle, R.V.; Strobell, D.F.; Lellouch, E.; Gautier, D.: The Yelle Titan Atmosphere Engineering Models, in *HUYGENS - Science, Payload and Mission*, ESA-SP-1177, 243, 1997

Zarnecki, J.C.; Banaszkiewicz, M.; Bannister, M.; Boynton, W.V.; Challenor, P.; Clark, B.; Daniell, P.M.; Delderfield, J.; English, M.A.; Fulchignoni, M.; Garry, J.R.C.; Geake, J.E.; Green, S.F.; Hathi, B.; Jaroslawski, S.; Leese, M.R.; Lorenz, R.D.; McDonnell, J.A.M.; Merryweather-Clarke, N.; Mill, C.S.; Miller, R.J.; Newton, G.; Parker, D.J.; Rabbetts, P.; Svedham, H.; Turner, R.F.; Wright, M.J.: The Huygens Surface Science Package, in *HUYGENS - Science, Payload and Mission*, ESA-SP-1177, 177, 1997